BIOMECHANICS OF ENGINEERED SMOOTH MUSCLE MICROTISSUES

By

Alan S. Liu

A dissertation submitted to The Johns Hopkins University in conformity with the requirements for the degree of Doctor of Philosophy.

Baltimore, Maryland

September, 2015

Abstract

Mechanical forces play a large role in biological processes. While individual cells are the basic unit of force generation in organisms, it is only at the tissue level of organization where the interplay between groups of cells and the surrounding extracellular matrix (ECM) can be studied. To investigate how mechanical forces affect tissues, a microfabricated substrate consisting of two flexible cantilevers was used in order to simultaneously apply forces to and measure responses from engineered microtissues. These constructs consisted of a few hundred bovine pulmonary smooth muscle cells contained in a collagen/fibrin matrix which spanned the gap between the two cantilevers. A nickel microsphere bonded to the top of one of the cantilevers enabled the application of force to the system through the transduction of a magnetic field generated by a magnetic tweezer apparatus.

To investigate the mechanical properties of these microtissues, a quasistatic stretching protocol was applied and the tissues' stress-strain response was measured. The ECM component of this response was ascertained by lysing the cells in select microtissues before applying the stretching protocol. A mathematical model was developed to help quantify these microtissue mechanical properties, and it was found that the cells contribute the bulk of the viscoelastic response while the ECM contributes most of the viscoplastic response. Notably, the presence of the cells seems to shield the microtissue from yielding under tension.

The effect of periodic forces was also investigated. Successive quasistatic actuations as well as continuous cyclic strains were applied to the microtissues. The

results from the repeated quasistatic stretches showed an active reinforcement of tissue stiffness following the first stretch, revealed a time scale of approximately 10 minutes during which the microtissues reverted to their pre-stretch states, and reinforced the dichotomy between the cell and ECM contributions to microtissue mechanical properties. Continuous cyclic stimulation led to two distinct initial responses from the microtissues: a relatively linear viscoelastic response as well as a strain-stiffening response. The strain-stiffening of the tissue diminished over the course of the continuous stimulation and microtissue behavior converged, indicating an active response.

In order to apply magnetic forces to multiple microtissues simultaneously, a microfabricated device was designed and validated, and it was shown to reproduce the amount of force generated by the magnetic tweezer. Lastly, human embryonic stem cell-derived cardiomyocytes were used to construct microtissues, and they were able to mimic the pacing and Frank-Starling characteristics of native cardiac tissue.

By elucidating the interplay between cell and extracellular matrix biomechanics, the experimental work reported with these microtissues provides new understanding of fundamental biophysical properties of cells and tissues and can potentially provide new input for applications such as tissue engineering and drug discovery and testing.

Advisor: Daniel H. Reich

Acknowledgements

My time at Hopkins has been filled with challenges and rewards. Throughout it all, Dr. Daniel Reich has been a constant source of guidance, knowledge, and encouragement. I would like to thank him, as well as my former lab-mates, Edward (Jim) Felton, Corinne Kramer, Craig Copeland, and Ruogang Zhao for teaching me how to do science and for setting an example of what it means to be a good researcher. For my current lab-mates, Yu Shi and Prasenjit Bose, the journey may seem long, but remember: clear eyes, full hearts, can't lose.

I would also like to thank my fellow graduate students in physics as well as those in other departments for fostering such a great sense of community at Hopkins. Life would have been duller without you guys. Last, but definitely not least, I thank my parents, who have always supported me in all my interests, as well as my little brother (for being awesome).

I have been shaped as a scientist, and as a person, by all of these people, and I hope to take the best parts of their influence with me into the future as I aim high and strive to be all that I can be.

Table of Contents

List of Tables

List of Figures

Chapter 1 Introduction and Overview

1.1 Introduction

Physical forces play an important role in biology on many scales, from limb movement to cell division. The study of biomechanics has the potential to enhance our picture of living systems. As the smallest biological unit of force generation in organisms, cells must collectively contribute to larger scale forces, whether through interactions with each other or through interactions with the extracellular matrix (ECM) in which they exist. Although, single-cell and excised-tissue mechanics have been studied extensively, the mechanical properties of a biological system between these two length scales is still relatively unknown. How do the collective effects of the forces generated by many cells influence their surrounding environment? To answer this question, I will present the use of microtissue constructs composed of hundreds of cells encapsulated within a fibrous matrix as a mechanical model of a simple tissue.

1.2 Cell mechanics

From a biomechanical perspective, cells have three general roles: force sensing, force generation, and force transmission. Jointly, these three capabilities help define a cell's mechanical interaction with its environment.

1.2.1 Mechanotransduction

Mechanotransduction refers to the various cellular processes whereby mechanical stresses are converted into biochemical activity. The results of cellular force sensing can be seen on multiple scales, from the very familiar strengthening of skeletal muscle due to exercise to the very subtle rearrangement of internal cellular structure due to flow-induced shear stress [1]. The effects of mechanotransduction are varied. In normal conditions, mechanical cues guide embryonic development, gene expression, cell function, and differentiation [2-4]. Similarly, in disease conditions, the mechanotransduction machinery also has implications for cancer metastasis and the development of atherosclerosis [5, 6].

Cells can sense physical cues from their environment through multiple avenues, including ion channels which open as the cell is stretched, intracellular proteins which undergo conformational changes as the cell is compressed, and specialized sensor complexes located on the cell surface which respond to shear stress as fluid flows over the cell [7]. Focal adhesions also play a large role in mechanotransduction. These large macromolecular complexes connect the internal cellular cytoskeleton (CSK), a filamentous network which gives mechanical shape and structure to the cell, to the external extracellular matrix (ECM), a network consisting of polymer-like proteins (e.g.

collagen, fibrin) which exists in the interstitial space between cells to provide structural support to the cells therein (Figure 1.3).

Recent experiments have taken advantage of advances in the microfabrication of biologically compatible substrates and the micromanipulation of biological probes to study how single cells on planar substrates respond to varied mechanical stimuli. These efforts have included mechanically stimulating cells at their focal adhesion sites [8] , applying both global as well as inhomogeneous strains to cells [9, 10], and poking cells [11]. Although the results from these experiments have been rich and elucidating, the responses of single cells on flat substrates may not recapitulate the *in vivo* condition of multiple interacting cells in a three dimensional environment.

1.2.2 Cellular force generation

In the context of muscle-generated forces, the most important source of intracellular contractile force is the actin-myosin complex. Individual actin molecules (globular actin subunits) polymerize to form microfilaments, one of three key components (the others being intermediate filaments and microtubules) of the cellular cytoskeleton. Changes in the structure of the cytoskeleton underlie many important processes such as cell migration and cell division, and they can be dramatically seen in the formation of lamellipodia and filopodia [12].

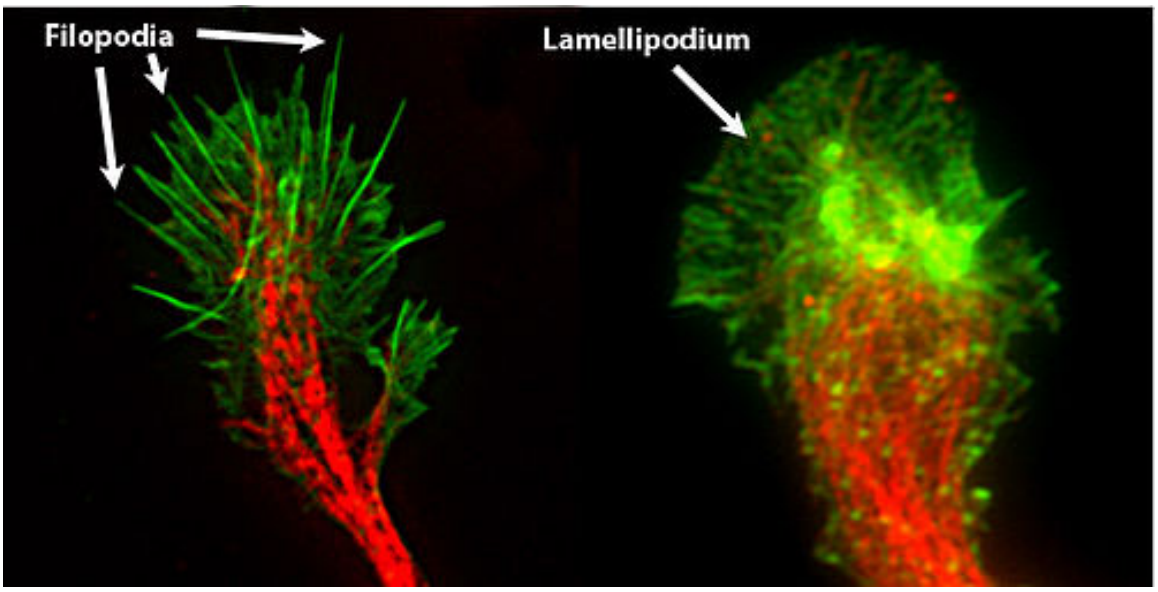

Figure 1.1 Filopodia and lamellipodium. These structures are involved in cell motility and their shape is characterized by that of the underlying actin cytoskeleton (green) [from Wikimedia commons].

Microfilaments, or actin filaments, have a diameter of ~7 nm and form a mesh network throughout the entire cell, giving it mechanical strength. These filaments grow and shrink in response to cell signaling mechanisms which affect the relative rates of these two processes and drive changes in mechanically-governed properties such as cell shape and cell locomotion [12].

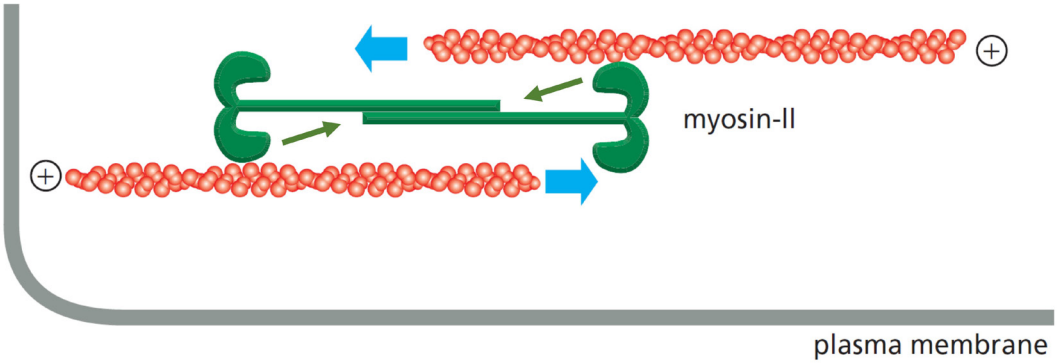

Figure 1.2 Actin-myosin force generation. Myosin filaments (green) join adjacent actin filaments (red) which are polarized in opposite directions. As the head of the molecular motor contracts (green arrows) towards the centerline of the myosin filament, it causes a relative sliding motion of the actin filaments (blue arrows). The 'plus' ends of the actin filaments can be anchored onto the plasma membrane and thus the relative sliding motion generates a contractile force [12].

Myosins are protein motors which act in conjunction with actin polymers to generate cellular force. In muscle contraction, filaments of myosin II associated with actin filaments generate a relative sliding motion between the actin filaments (Figure 1.2) [13]. Together, this force-generation machinery is referred to as the actin-myosin system and is regulated largely by the ROCK (Rho-associated protein kinase) biochemical pathway (see § 3.3.2).

There have been many efforts to study and quantify the contractile force generated by cells. The earliest studies which used wrinkles in simple 2D deformable substrates to visualize cell forces have evolved into the computer-aided tracking of the 3D traction force distribution around a cell embedded in a gel [14, 15]. Along the way, the forces associated with cell-cell interactions have also been quantified by studying the mechanical reciprocity between multiple cells cultured on 2D substrates [16, 17]. Although these studies have resulted in detailed measurements of sub-cellular scale

forces, the methods used therein are difficult to apply to the study of collective forces associated with multiple cells interacting over long ranges in a 3D environment. The use of collagen gels which encapsulate many hundreds of cells has been seen as a solution to this shortcoming.

1.2.3 Cellular force coupling

Cells not only sense and generate forces, they also transmit them. The intracellular actin network is anchored to sites along the cell membrane. At these sites, trans-membrane proteins transfer the force generated by the actin-myosin system to other cells or the ECM.

Adherens junctions couple together the actin cytoskeleton of two neighboring cells. The cytoplasmic face of each of these junctions links directly to the actin network, and the adherens junctions of neighboring cells are bound together through outward-facing cadherins proteins.

Analogously, the internal actin network of a cell is connected to the ECM through integrins. These integrins are localized at focal adhesion complexes made up of many types of proteins. The outward facing portion of different integrins has different ligands, allowing the focal adhesion complex to bind to various types of ECM proteins (Figure 1.3).

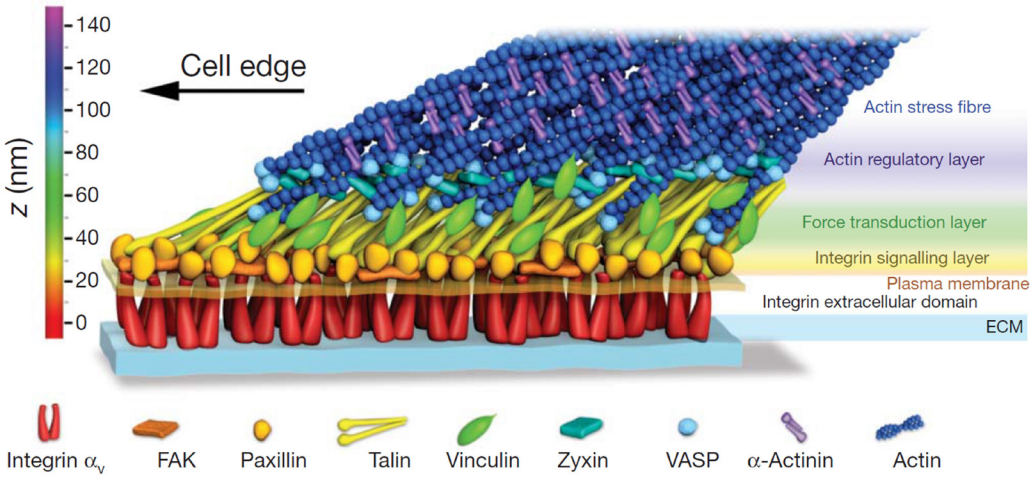

Figure 1.3 Cell-ECM interaction. Actin stress fiber interaction with the ECM is mediated by a number of trans- and near-membrane proteins at focal adhesion sites [18].

1.3 Cell-populated collagen gels

Cell-populated collagen gels are some of the simplest model systems which capture the dynamic reciprocity (i.e. cell and matrix properties have a synergistic effect on the overall construct) between cells and matrix in a 3D environment. These cell-matrix constructs have been used to investigate wound healing [19], artificial tissue engineering [20, 21], and, more closely related to this thesis, collective cell/matrix mechanical properties [22-24]. Scientists have found that varying design parameters such as collagen concentration, cell density, and boundary conditions have a dramatic effect on the overall mechanical properties of the artificial tissue construct [25].

Biomechanical studies of engineered cell-populated collagen tissue models have generally involved centimeter-scale constructs which must first be grown and then transferred to a mechanical testing apparatus [25]. These techniques, however, suffer

from high diffusion barriers for testing of soluble factors due to the large size of the constructs as well as errors induced by the handling of specimens as they are mounted on the testing apparatus. Furthermore, as tissue engineering begins to take advantage of robust, but relatively rare and valuable, stem cells, the large quantities of cell material needed to engineer these cell-matrix constructs limits their usefulness.

The recent development of microfabricated tissue gauges (μTUGs) allows for the engineering of sub-millimeter scale cell/collagen constructs as well as the *in situ* measurement of tissue generated force and tissue stiffness [26, 27]. These devices require less material, obtain higher throughput, and have no need for manual handling compared with previous techniques.

1.4 Experimental overview

In the experiments that are presented in this thesis, I used μTUGs to measure and manipulate microtissues consisting of bovine pulmonary artery smooth muscle cells (BPA-SMCs) embedded in a collagen/fibrin matrix. The engineering parameters for these microtissues were first determined and then their contractility was observed in both control conditions and in conditions where their biological or physical structure was altered.

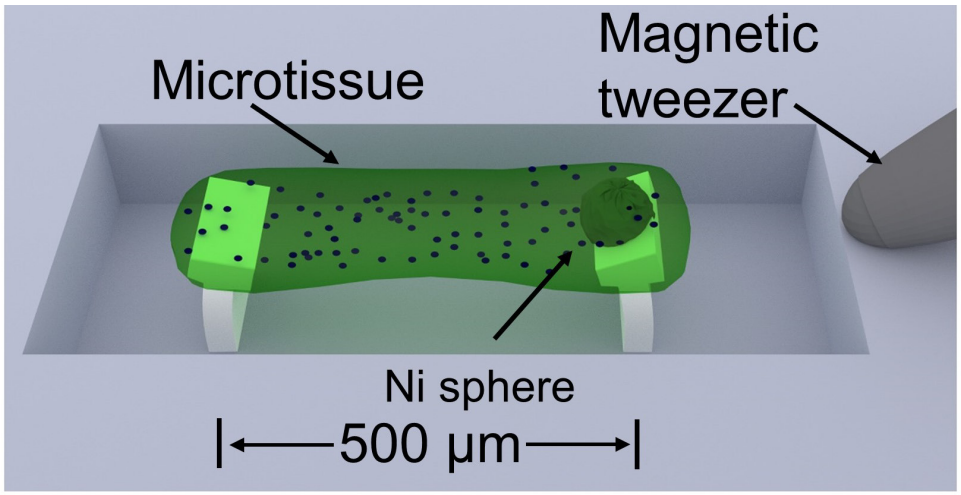

Figure 1.4 Microtissue and µTUG system. Digital schematic of complete experimental system. Microtissue (green interspersed with blue cells) is engineered on two flexible cantilevers (white). Microtissue stretching is achieved by transducing a magnetic field generated by the magnetic tweezer into an applied force via the nickel sphere which is bonded to one of the cantilevers.

The µTUG substrate was modified such that forces up to 25 µN could be applied via an external magnetic field, and the dynamic response of the tissue was measured through the application of a quasistatic stretching force, causing a maximum of 7% strain on the tissues. A mathematical model was developed to describe the response of the microtissues to this force, enabling the quantitative determination of key mechanical properties. Repeated quasistatic actuations allowed the observation of active reinforcing behavior by the microtissues. Ultimately, continuous sinusoidal stretching forces were applied at a frequency of 1 Hz in order to mimic the cardiac rhythm.

Finally, microtissues were engineered using stem-cell derived cardiomyocytes as a proof of concept of the ability of this system to also support stem-cell based tissues.

1.5 Dissertation outline

Chapter 2 contains the general materials and methods used to prepare μTUG substrates, engineer microtissues, apply external force, and undertake the relevant image/data analysis. In Chapter 3, static microtissue mechanical properties as well as their response to pharmacological treatment are described. Chapters 4 and 5 discuss the microtissue response to quasistatic and dynamic periodic applied forces. In Chapter 6, the creation of a device to apply forces to multiple microtissues simultaneously is described. Lastly, Chapter 7 provides a summary and discussion of the thesis as a whole and describes experiments undertaken with stem-cell based microtissues.

Chapter 2 Materials and methods

2.1 Introduction

The experimental work in this thesis combined techniques from microlithography, tissue engineering, micromanipulation using magnetics, and digital image processing. These techniques will be presented in this order below. Briefly, μTUG substrates are fabricated in polydimethylsiloxane (PDMS) through the creation of a silicon master mold and subsequent replica molding processes. Microtissues are engineered on these substrates by introducing a liquid solution containing ECM and cells, and then relying on polymerization and cellular-driven self-assembly to enable the formation of coherent tissues. These tissues are then manipulated through a magnetic tweezer system. Finally, quantitative data is gathered through the computer-aided analysis of images obtained by both phase contrast and fluorescence microscopy.

2.2 Device Fabrication

2.2.1 µTUG creation process

An overview of the µTUG fabrication process flow is shown in Figure 2.1 Master molds were created on silicon substrates by patterning SU-8 photoresists in a two layer photolithography process [28]. Structures on these master molds correspond directly to the final structures on the µTUG device.

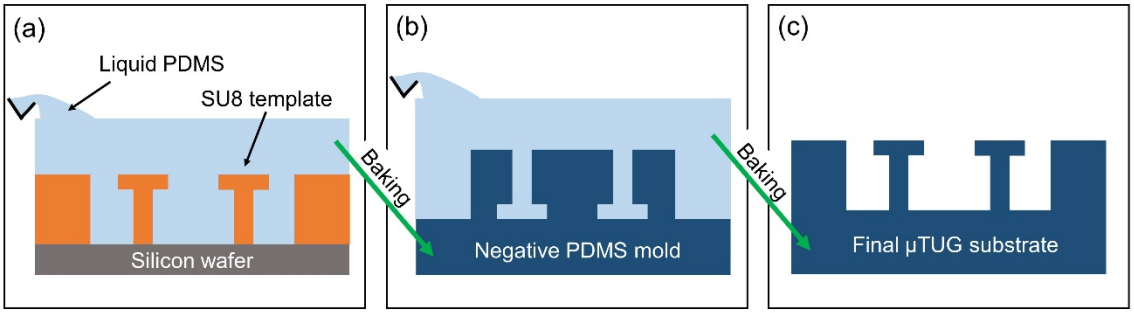

Figure 2.1 Replica molding process. (a) Master molds were created through 2-layer photolithography of SU-8 photoresist (orange) patterned on a silicon substrate (gray). Negative geometry molds were created by casting liquid PDMS (light blue) over the master mold. (b) After baking, liquid PDMS hardens into a negative geometry mold of the master (dark blue). Liquid PDMS was cast into this negative mold to ultimately form the final µTUG substrate. (c) µTUG substrate was formed after baking and has the correct final geometry.

The second major step in the fabrication process is to make negative geometry PDMS molds from the masters. The silicon wafers on which the master structures were built were placed in a weighing boat with the structures facing up. Liquid PDMS (Sylgard 184, Dow Corning) at a 1:10 primer:base ratio was poured into the boat and

over the master molds. The entire boat was then degassed in vacuum to ensure the accurate replication of the features on the master mold in the PDMS negative. Following the degassing procedure, the boat and its contents were baked overnight in an oven at 65 °C. The next day, the hardened PDMS was peeled away from the master molds with the help of EtOH as a detachment agent. Negative molds used in this experiment were obtained from Dr. Christopher Chen at the University of Pennsylvania.

The surfaces of these negative PDMS molds were treated before being used to create μTUG devices. This process consists of a 25 watt, 45 second treatment at 450 mTorr in air plasma in order to change the surface chemistry of the PDMS to allow for stronger hydrophilic bonds [29]. Following the plasma treatment, the negative mold was coated with 20 μL of (Tridecauoro-1,1,2,2-Tetrahydrooctyl)-1-Trichlorosilane (United Chemical Technologies) via overnight evaporation in a vacuum desiccator. The silane treatment enables easier separation of the μTUG substrate from the negative mold.

μTUG devices were fabricated in 35 mm plastic tissue culture dishes. First, a 1 mm thick layer of liquid PDMS mixed at a 1:10 ratio of primer:base was deposited into the 35 mm dish. To harden this layer, the dish was baked on a hotplate at 70 °C for 45 minutes. Concurrently, liquid PDMS was poured over the top of the negative PDMS molds and degassed. Following the hardening of the bottom layer, the negative PDMS mold was inverted into the dish and the remaining volume was filled with liquid PDMS. The entire ensemble was degassed and then baked at 70 °C overnight, after which the negative PDMS mold was peeled off with EtOH, leaving the final μTUG substrate.

Figure 2.2 µTUG device fabrication. (a) Liquid PDMS was deposited onto negative geometry mold with features facing up. (b) The entire ensemble was degassed in a vacuum desiccator until no bubbles remain. (low image quality due to shooting through optically poor lid of desiccator). (c) The negative mold was then inverted onto a 35 mm petri dish with a hardened bottom coating of PDMS and the remaining volume was filled with liquid PDMS. The entire 35 mm dish was again degassed to remove bubbles. (d) The dish is baked overnight at 70 °C to cure the liquid PDMS. Final µTUG substrate results after removal of negative geometry mold (Figure 2.3).

For the work in this thesis, the µTUGs consisted of 800 µm by 400 µm microwells each containing two microcantilevers spaced 500 µm apart. Each microcantilever was ~125 µm tall and had a base area of 30 µm by 170 µm. The upper third of each microcantilever had dimensions of 100 µm by 320 µm. These enlarged heads are designed to prevent the microtissues from slipping off the microcantilever as it deflects. Up to 130 microwells can be arrayed in a single 35 mm dish (Figure 2.3).

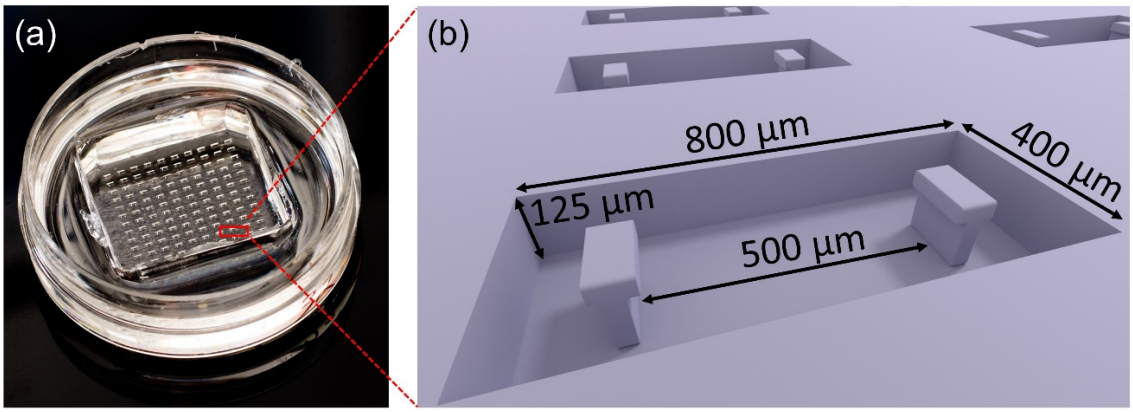

Figure 2.3 µTUG geometric properties. (a) Photograph of µTUG substrate showing arrays of individual microwells in a 35mm dish. In this example, microwells are arrayed in 13 rows by 10 columns. (b) Digital representation of individual microwell structure with dimensions.

2.2.2 µTUG modifications

The pillars in the µTUG devices were sometimes modified to aid in imaging or to prepare them for magnetic force transduction (Figure 2.4). In order to track pillar positions in a fluorescence imaging modality, pillar tops were tagged with fluorescent micron-scale particles. A solution of liquid PDMS and fluorescent particles (Sigma, L3030, λ_{ex}~575 nm; λ_{em}~610 nm) was manually painted on to the pillar tops and allowed to dry overnight.

In many experiments, an external magnetic field was applied to the µTUGs in order to stretch the microtissues. To transduce this magnetic field into a force, a ~100 µm diameter nickel microsphere was bonded to one of the pillar tops using PDMS. Nickel powder (-150 +200 mesh) was purchased from Alfa Aesar (Stock #44739). The most spherical particles were selected, coated in liquid PDMS, manually placed on the correct micropillar, and baked in 70 C overnight. This adhesion was robust—we saw no detachment of the beads in our subsequent experiments.

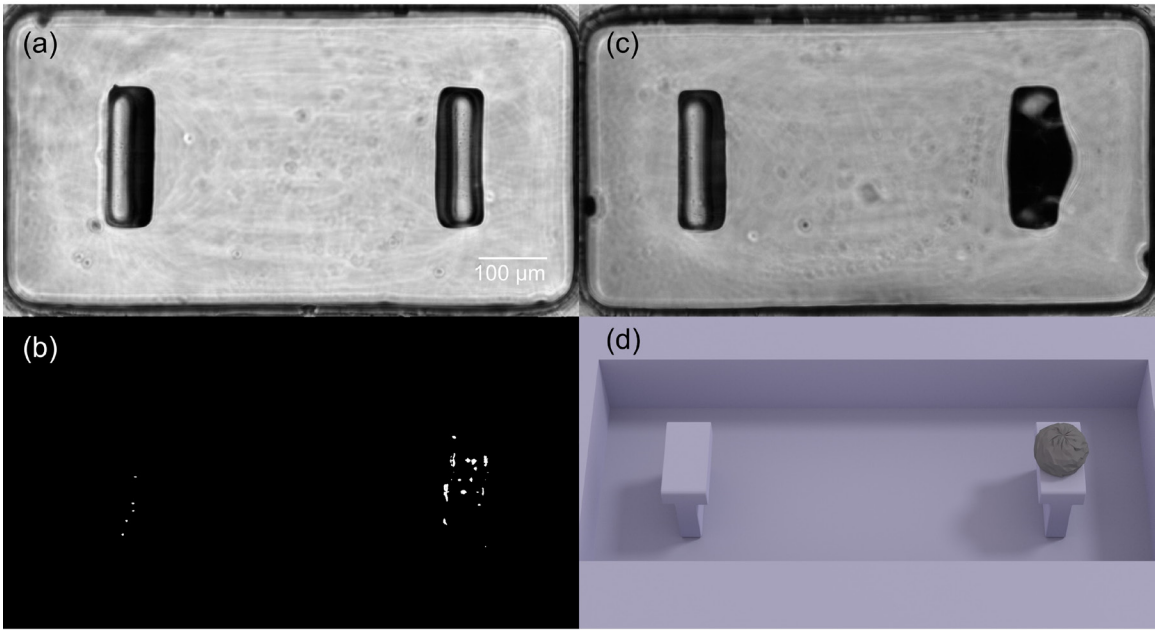

Figure 2.4. µTUG modifications. (a) Phase image of µTUG with pillar-tops tagged with fluorescent microparticles. Microparticles are not discernable in white light. Scale bar = 100 µm. (b) Corresponding fluorescent image of (a), showing pillar tops tagged with fluorescent particles, which can be clearly seen. (c) Phase image of µTUG with nickel microsphere bonded to right pillar. (d) Digital representation of µTUG to show detail.

2.3 Microtissue engineering

2.3.1 µTUG surface preparation

Immediately prior to use in experiments, µTUGs were prepped for sterility and non-adhesion. For sterility, a 70% solution of ethanol was pipetted into the µTUG substrate. After 5 minutes, this solution was aspirated, and the µTUG was dried with N_2. In order to reduce cell-PDMS adhesion, a 0.2% w/v solution of Pluronic F-127 (BASF)

was then gently pipetted into the μTUG (taking care that no solution entered the microwells themselves), allowed to remain for 15 min, and then aspirated. The time that the Pluronic solution remains in the μTUG should be adjusted based on cell type (time quoted here relates to experiments performed with BPA-SMCs). Lastly, the μTUG was rinsed with phosphate-buffered saline (PBS), dried with N_2, and then placed in a -20° C freezer until it was needed again. The total time in the freezer was ~20 minutes, but this is not a crucial parameter

2.3.2 Microtissue creation

As stated previously, creating microtissues relies on the cellular self-assembly of a matrix solution [26, 30]. For BPA-SMC tissues, I determined that the optimal ECM solution consists of 2.5 mg/mL collagen and 2 mg/mL fibrin. The collagen solution was purchased from BD Biosciences (354236), and its concentration (usually between 3-5 mg/mL) is determined by the manufacturer. The fibrin solution was made from fibrinogen from bovine plasma (Sigma F8630) dissolved in Hanks' balanced solution (Gibco) to a concentration of 100 mg/mL. 2 mL of ECM solution was used per each μTUG substrate. This 2 mL of solution consisted of 200 μL M199 10x (Sigma), 83 μL HEPES (Sigma), 14 μL $NaHCO_3$ (5% w/v), and 40 μL of the 100 mg/mL fibrin solution regardless of the starting concentration of the purchased collagen solution. Enough of the collagen solution was added to the ECM solution to give a final collagen concentration of 2.5 mg/mL. NaOH (1 M) was added to the ECM solution at a 0.022:1 NaOH:stock collagen solution (by volume) ratio to adjust the pH, though some titration may be

required. Sterile H_2O made up the rest of the 2 mL of ECM solution. It is important to keep the ECM solution chilled on ice in order to reduce polymerization.

A sample preparation using a stock collagen concentration of 3.77 mg/mL is shown in the table below. Components of the ECM solution are added in the order that they are presented in the table. Total solution volume equals 2 mL.

Component	Volume (µL)
Water	332.3
M199 10x	200
HEPES (250 mM)	83
$NaHCO_3$ (5% w/v)	14
NaOH (1 M)	28.6
Collagen (3.77 mg/mL)	1302.1
Fibrin (100 mg/mL)	40

Table 2.1 Volume of components comprising 2 mL ECM solution. Components in blue remain constant with changing concentration of stock collagen solution.

Subsequent detailed steps in this procedure are presented in the Appendix. Briefly, however, ~300,000 BPA-SMCs are mixed into the ECM solution, and this solution is centrifuged into the microwells on the µTUG substrate. Following a short polymerization in the incubator, tissue culture media is then added to the µTUG.

2.4 Microtissue force and stress determination

In these experiments, the forces involved can be determined by examining the deflections of the micropillars. Micropillar deflection is related to the amount of force acting on the micropillar through the micropillar's effective spring constant. Force-deflection relationships were determined using three different methods: fitting empirical data, developing a finite element model, and using analytical beam bending theory. Results from empirical fitting were used for deflections in the linear regime while finite element modeling was used for large deflections in the non-linear regime. Analytical beam bending theory was used to corroborate the scale of the results from the previous two methods. Stresses experienced by the microtissues were found by dividing the force found by analyzing the pillar positions and then dividing by the cross sectional area of the narrowest part of the tissue.

2.4.1 Empirically determined spring constant

To experimentally determine the spring constant of the micropillars, collaborators at the University of Pennsylvania used calibrated glass pipettes to deflect the micropillars (see Supplementary Information in [26]). Briefly, known forces were used to determine a force-deflection relationship of the glass pipettes. These calibrated glass pipettes were then used to deflect the micropillars, and a spring constant was calculated based on the forces applied to the micropillar and the resulting deflection. The majority of the μTUG substrates used in these experiments contained micropillars with a spring constant of 0.6 μN/μm.

2.4.2 Force-deflection relationship through finite element modeling

For large deflections, when a simple, linear spring constant does not accurately capture the behavior of the micropillar, a finite element model was developed by our former post-doc, Ruogang Zhao, using micropillar dimensions and the bulk PDMS Young's modulus of 1.6 MPa [31].

Figure 2.4 shows a comparison of the finite element analysis with a strictly linear analysis. The independent axis denotes the ratio between pillar-top displacement relative to pillar height. On the dependent axis, p is load, L is total pillar height, E is the PDMS Young's modulus, and I is the bending moment. The finite element analysis and the linear analysis converge at deflection/pillar height ratios of less than 30%. A polynomial fit was determined for the finite element data as well.

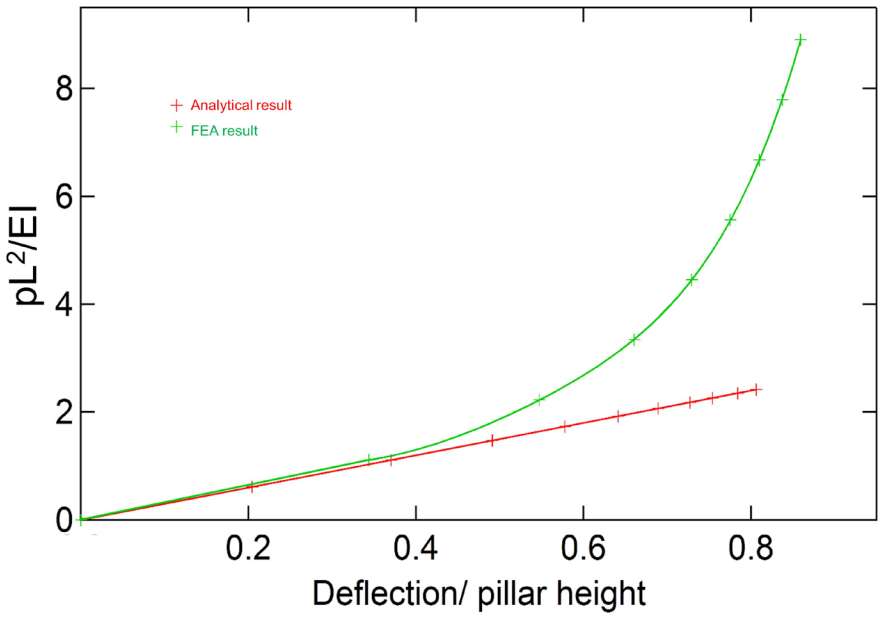

Figure 2.5 Finite element analysis. Green curve shows fit to finite element analysis. Red curve shows behavior if a strictly linear model is used.

2.4.3 Analytic Beam Bending Theory

Each micropillar can be approximately modeled as a cantilever with one fixed end [32] (Figure 2.6). As forces are applied to the free end of the micropillar, in this case by tissue forces, the micropillar deforms. By tracking the position of the free end, the forces involved can be calculated. This simple beam bending model does not account for the enlarged heads of the micropillars. However, since deflection force data used in this thesis was determined either empirically or through finite element analysis, analytic beam bending theory was only used to validate the scale of forces associated with micropillar deflection.

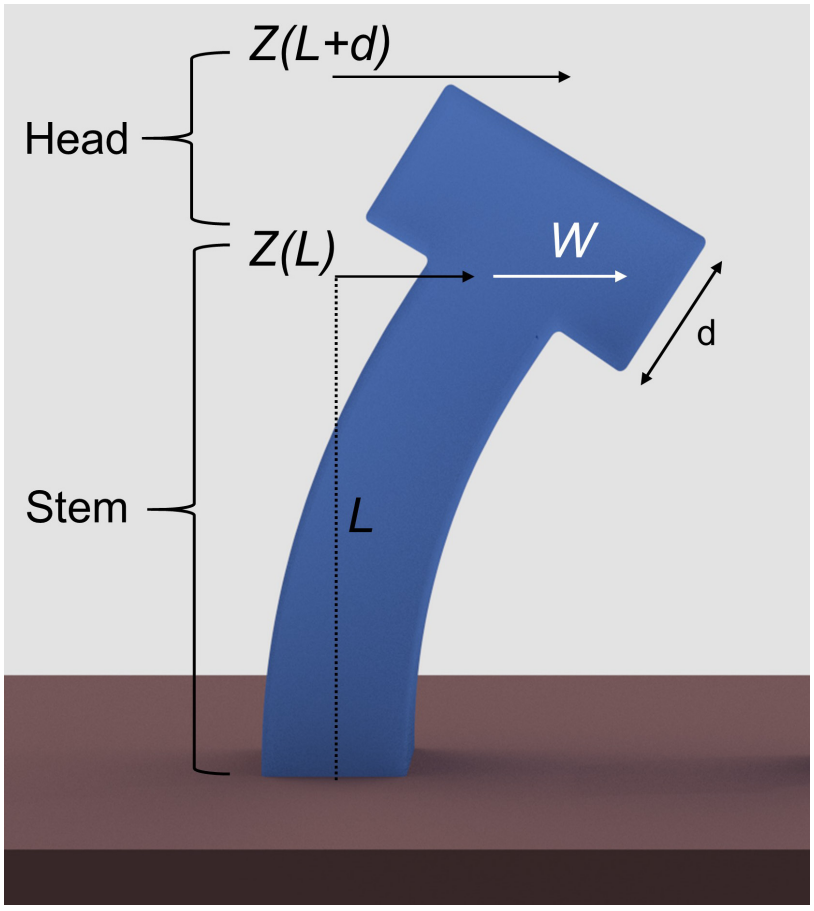

Figure 2.6 Fixed end cantilever. The deflection of the micropillar was approximately modeled using simple beam bending theory. A force causing the deflection, *W*, is assumed to be applied at the intersection between the stem and the head of the micropillar, causing a horizontal deflection, Z(L) to the stem of the micropillar. The entire micropillar is deflected by an amount Z(L+d), with *d* being the thickness of the head of the micropillar.

To approximate the bending of the micropillar, force was assumed to be applied at the intersection between the stem and the head of the micropillar. The head of the micropillar was considered a rigid object since the bending stiffness scales as the square of the cross-sectional area. The cross-sectional area of the head is approximately four times that of the stem, leading to a 16-fold increase in stiffness. Our model is thus simple beam bending with the addition of a rigid element past the length of the stem.

From [32], the deflection, z, caused by force, W, evaluated at the top of the stem, L, is:

$$z(L) = \frac{W}{EI}\frac{L^3}{3} \tag{2.1}$$

Where, E is the PDMS bulk modulus, 1.6 MPa, and I is the bending moment of the stem. For our rectangular beams,

$$I = {BH^3}/{12} \tag{2.2}$$

where B and H are the long and short side, respectively, of the rectangular prism which models the stem of the PDMS cantilever. For our devices, B=170 μm and H=30 μm. Including the height of the head of the micropillars, d=40 μm, in order to calculate the total deflection of the micropillar:

$$z(L+d) = \frac{W}{EI}\frac{L^3}{3} + d\frac{z(L)}{L} \tag{2.3}$$

or

$$z(L+d) = \frac{W}{EI}\frac{L^2}{3}(L+d) \tag{2.4}$$

Rewriting equation 2.11 in the *F=kx* Hookean form

$$W = \frac{3EI}{L^2(L+d)}z = \frac{EBH^3}{4L^2(L+d)}z \tag{2.5}$$

gives us a "spring constant" of

$$k = \frac{EBH^3}{4L^2(L+d)} = 2\ \mu N/\mu m \tag{2.6}$$

which corresponds to the scale of the empirically measured spring constant reported in §2.4.2. The measured spring constant is lower than the analytically determined one because the bulk of the stem oftentimes has a slightly smaller cross sectional area than its base.

2.5 Pillar actuation and tracking

The micropillars were actuated by transducing an externally applied magnetic field through the attached nickel microsphere into an applied force. The positions of the micropillars were determined through both phase and fluorescent microscopy, depending on the time resolution required. Fluorescence microscopy (using a Roper Scientific CoolSnap HQ camera) was used for quasistatic experiments while high-speed phase microscopy (using an Allied Prosilica GX) was used for dynamic oscillatory experiments.

2.5.1 Electromagnetic tweezer system

An electromagnetic tweezer system was used to generate the external magnetic field (Figure 2.7). This system consists of a $^{5}/_{16}$ inch diameter 1820 steel core sharpened to a ~ 100 µm diameter tip and inserted through a solenoid. The solenoid is housed in an aluminum block mounted on micromanipulators oriented along the x, y, and z axes; combined with the insertion depth of the steel core, this setup allows for precise control over the position of the pole tip along 4 axes.

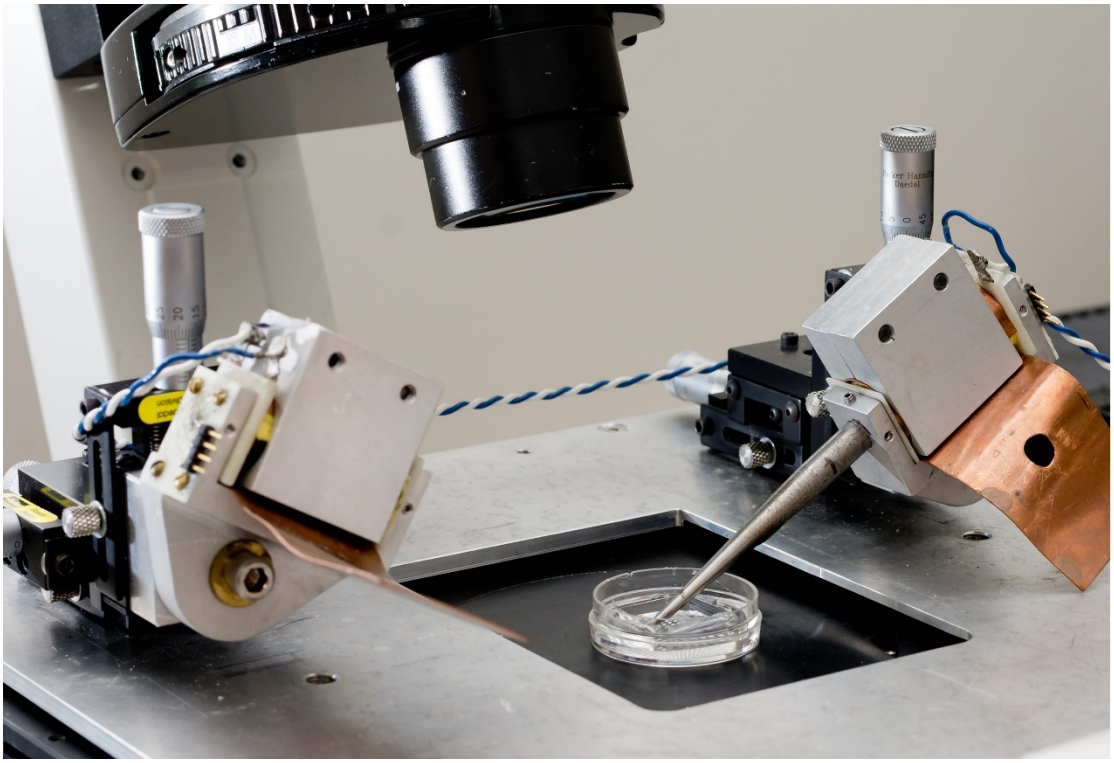

Figure 2.7 Electromagnetic tweezer system. Magnetic tweezer system supports up to two steel cores which act as electromagnetic pole tips (only one shown) mounted on 3-axis micromanipulators. 35 mm diameter µTUG sample shown as reference.

Current is passed through the solenoid coils to generate a magnetic field and can be controlled with a signal generator or with a computer-controlled National Instruments digital to analog converter (DAC) card. The magnetic field, and ultimately the magnetic force, experienced by the nickel microsphere depends on two factors: current in the solenoid and distance away from the pole tip. Figure 2.8 below demonstrates how these two factors affect local magnetic fields (as measured by Ruogang Zhao) [33]. The forces imparted to the nickel microsphere are described by $\mathbf{F}_{Mag} = \nabla (\boldsymbol{\mu}_{Sph}(\mathbf{B})\bullet\mathbf{B})$, where $\boldsymbol{\mu}_{Sph}$ is the field-dependent magnetic moment of the Ni sphere in the total field **B** produced by the magnetic tweezer. Maximum fields experienced by the nickel microsphere reached ~ 100 mT, resulting in a magnetic force of ~40 μN.

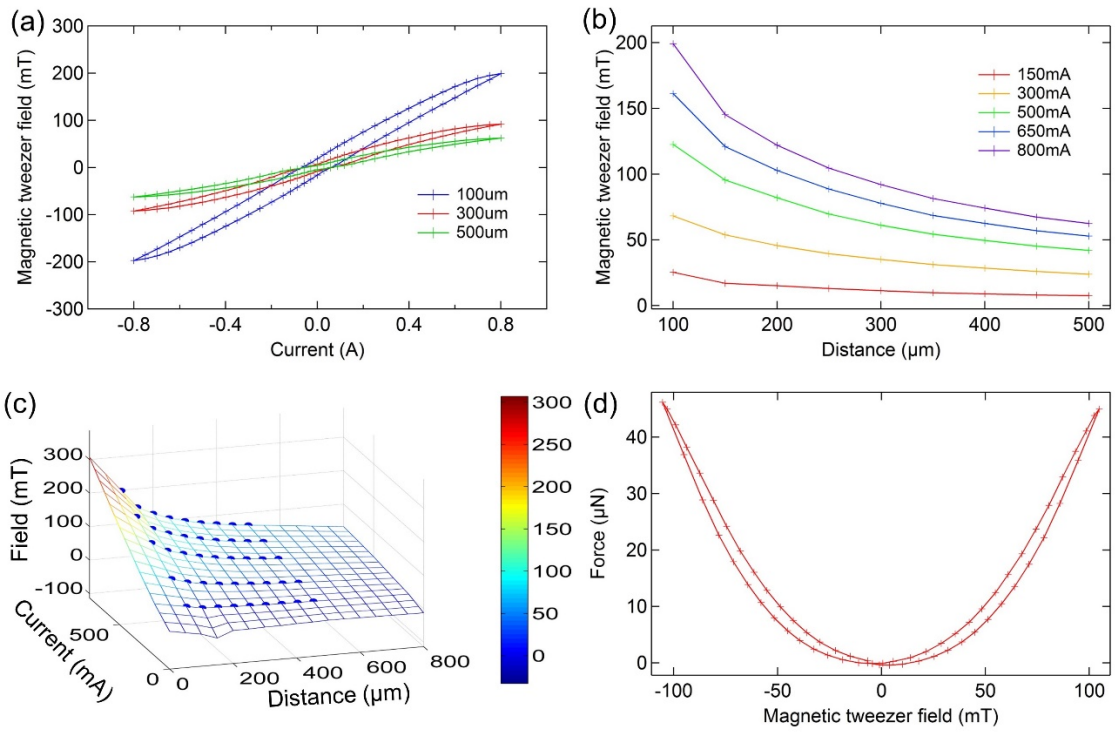

Figure 2.8 Magnetic field profile. (a) Magnetic fields at three distances were measured while cycling the current in solenoid. (b) Magnetic field vs. distance for 5 selected input currents. (c) 3D interpolation of magnetic field magnitude based on data in (a) and (b). Blue dots indicate actual data. Color bar denotes magnitude of magnetic field in mT. (d) Force experienced by nickel microsphere due to applied magnetic field [33].

The magnetic forces generated by this system are enough to strain the microtissues up to ~10%, as will be shown in later Chapters. Figure 2.9 below shows the alignment of magnetic tweezer tip in relation to the microtissues and the deflection caused by an applied force of ~28 μN.

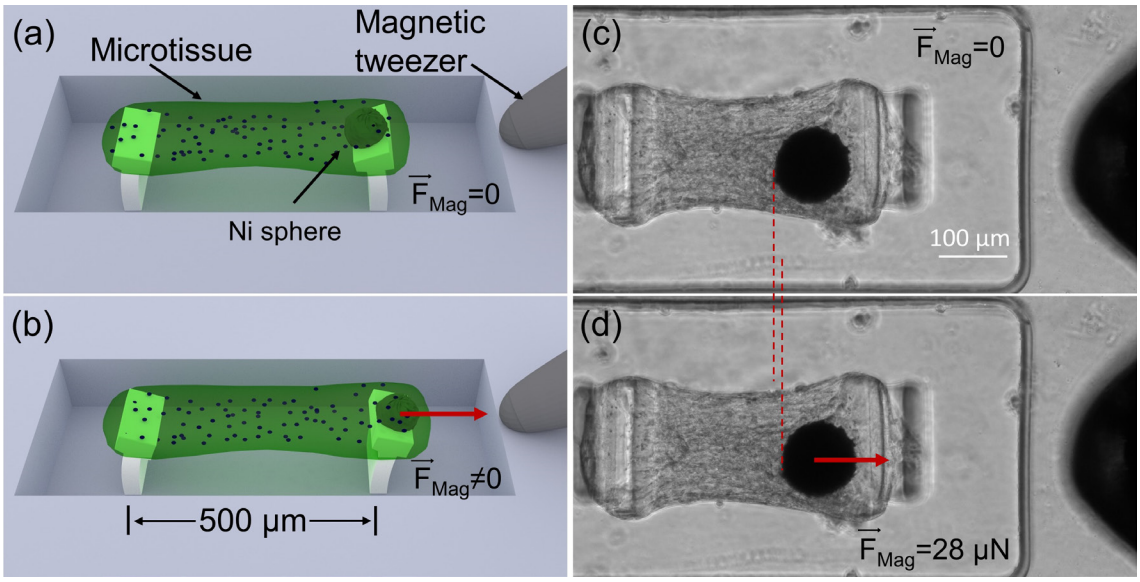

Figure 2.9 Microtissue stretching through application of magnetic force. Magnetic microtissue platform for the study of the dynamics of self-assembled smooth muscle tissue constructs. (a) Schematic three quarters view showing a microtissue suspended between two flexible PDMS micropillars whose deflections report the microtissue's contractile force. (b) A magnetic force, $\mathbf{F}_{Mag.}$, applied via a magnetic tweezer to a magnetic Ni sphere bonded to one of the pillars is used to apply strains to the microtissue. (c) and (d) show top-views of a SMC microtissue (c) as grown, and (d) subjected to a 2% strain under $\mathbf{F}_{Mag.}$ = 28 µN. The Ni sphere appears as a black circle, and the tip of the magnetic tweezer is visible at the right edge of the images.

2.5.2 Pillar tracking

Pillar positions were determined using two different imaging modalities: fluorescence imaging at approximately 1 frame every 10 seconds and high speed phase microscopy at a frame rate of 100 fps. Both types of imaging were performed on a Nikon TE-2000 microscope.

A single quasistatic stretch experiment sometimes lasted up to 25 minutes. At 1 frame every 10 seconds, up to 150 fluorescent images were captured with a Roper Scientific CoolSnap HQ camera during a single experiment. These images were all imported into ImageJ (NIH) and converted into a stack. The ImageJ Spot Tracker plugin

(Ecole Polytechnique Fédérale de Lausanne) was then used to isolate and track single fluorescent particles (Figure 2.10).

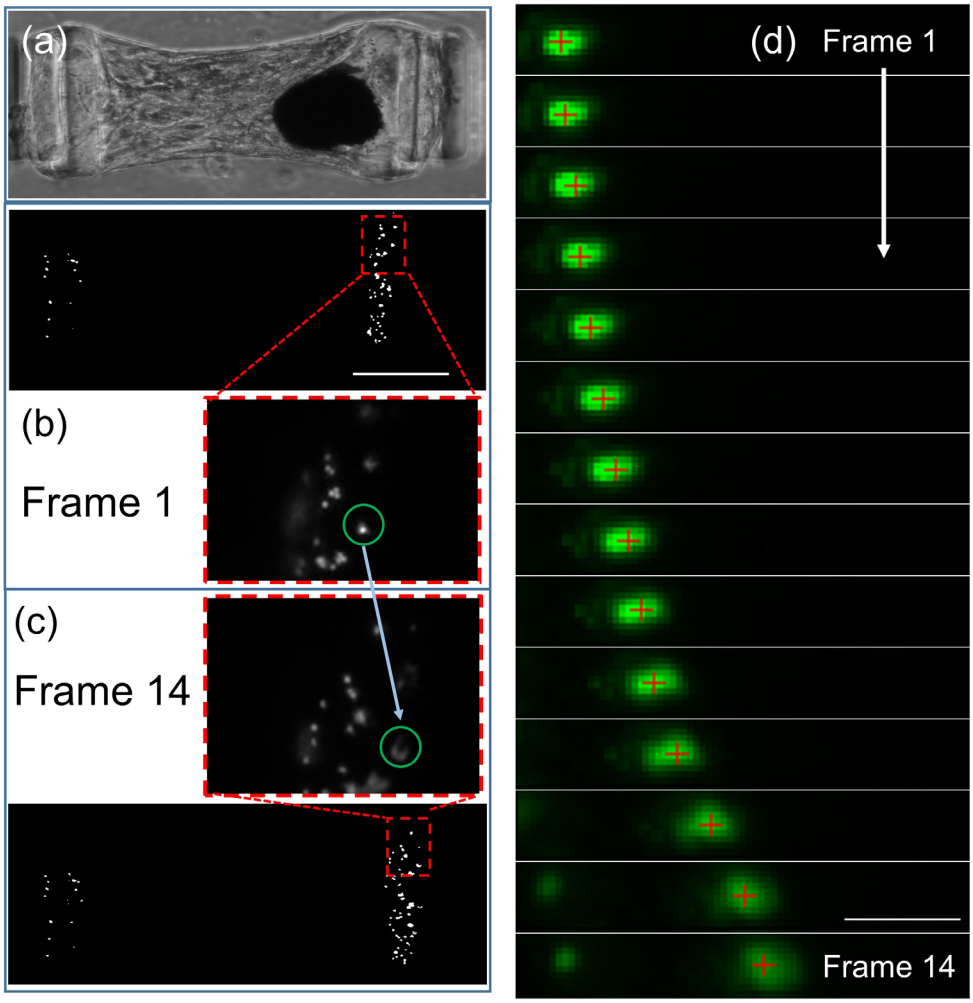

Figure 2.10 Pillar position tracking using fluorescence microscopy. (a) Phase image of microtissue. (b) First frame of fourteen frame widefield fluorescence image sequence of fluorescently tagged μTUG pillar tops. Two groupings of points can be seen which correspond to the two pillar tops. Scale bar=100 μm. Red inset shows detail of topmost portion of right pillar. Prominent fluorescent particle is circled in green. (c) Last frame of image sequence which corresponds to maximum deflection of pillar. Right-most group of fluorescent particles is noticeably shifted towards the right, the direction of $\boldsymbol{F_{Mag}}$. Red inset shows same area as in (a); same particle is highlighted in green. (d) 14 frame image sequence showing detail of ImageJ tracking of single particle. Scale bar = 10 μm.

Relevant Spot Tracker settings are presented in Table 2.2 below. These values can be adjusted based on the quality of imaging, range of pillar movement, and size of fluorescent spot.

Parameter	Value
Maximum displacement	35 pix
Intensity factor	85%
Intensity variation	20%
Movement constraint	30%
Center constraint	20%

Table 2.2. Spot Tracker settings which give good particle tracking results.

Imaging data for dynamic oscillatory experiments were recorded in one minute long video segments with an Allied Prosilica GX camera at five minute intervals. In order to ascertain pillar positions in this modality, image analysis was undertaken using the software package Igor Pro (Wavemetrics). The approach was to track the motion of identifiable features, such as the edge of the Ni bead on the magnetic pillar, or the edge of the PDMS head of the non-magnetic pillar (Figure 2.11a). A region of interest (ROI) that encompassed the horizontal motion of the feature of interest was defined for each pillar. As the motion of the pillars is only in the x-direction, for each region of interest, pixel intensity values along the y-direction were averaged to improve signal-to-noise, and a single value was assigned to the corresponding x-position. An example of such a y-averaged intensity trace for the ROI shown in Figure 2.11a is shown in Figure 2.11d.

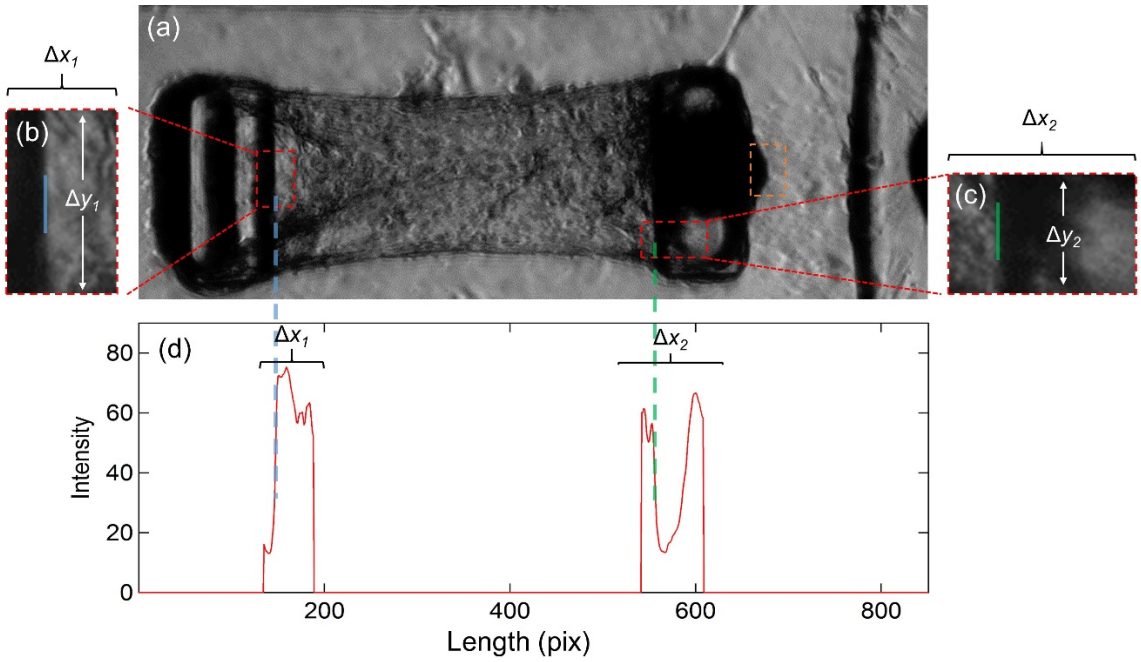

Figure 2.11 Region of interest selection and creation of y-averaged intensity plot. (a) Image of microtissue and μTUG substrate with red ROIs highlighted, one associated with each micropillar. These ROIs were selected because of the high contrast difference at the edge of the micropillar. Alternatively, the area near the edge of the nickel microbead could have been selected (orange). (b) Detail of left ROI with dimensions Δx_1 and Δy_1. Blue bar indicates area of high contrast gradient along the x-direction. (c) Detail of right ROI with dimensions Δx_2 and Δy_2. Green bar indicates area of high contrast gradient along the x-direction. (d) Intensity plot of image in (a). Intensity values corresponding to Δx_1 are intensities averaged over Δy_1. Intensities corresponding to Δx_2 are intensities averaged over Δy_2. Blue and green dashed lines help show correspondence between visual light/dark contrast in (a) and numerical light/dark contrast in (d).

Each intensity plot was fit with either an error function to track edges between high and low intensity or with IgorPro's built-in "peak-finder" feature to track peaks or valleys, as appropriate. Figure 2.12 below shows a representative intensity profile fit with an error function. For this particular trace, the edge was identified at x=146.73.

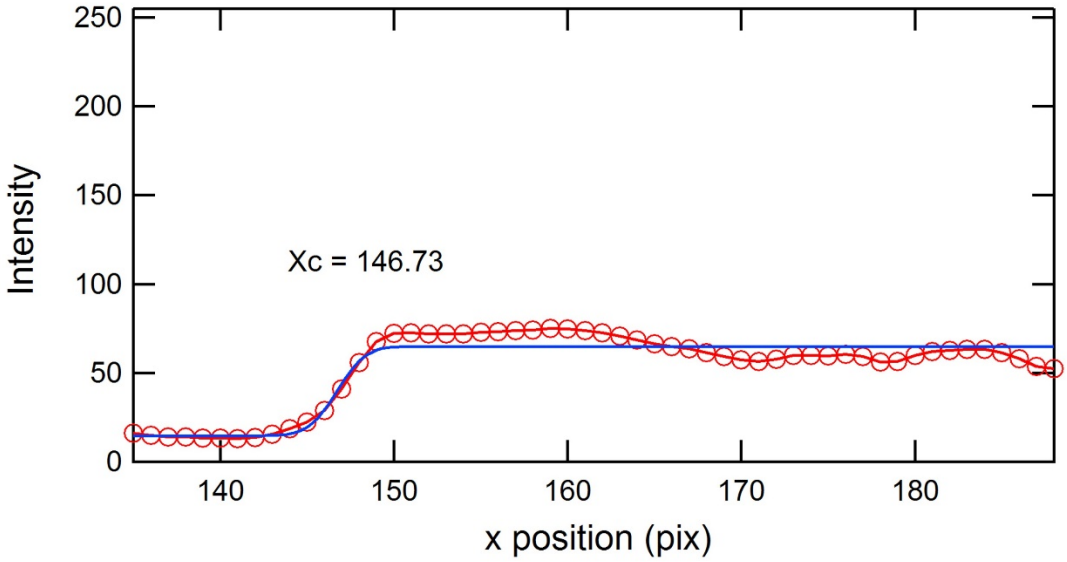

Figure 2.12 Fitting intensity plot to determine edge position. Representative plot of intensity associated with a single ROI. Data (red dots) was fit with an error function (blue line). Edge was identified at x=147.

The motion of high contrast edges is conveniently visualized by aggregating intensity traces for all frames in a video as the rows of a matrix (i.e. each row represents the intensity trace of a single frame of video). An intensity (image) plot of such a dataset yields what we termed a "waterfall plot" with distance on the horizontal axis, and time running vertically down. Contributions of all frames in the video leads to the complete waterfall shown in Figure 2.13a. The red sinusoidal line marks the positions of high contrast edges identified through the fitting procedure described above. This line also tracks the x-position of the high-contrast edge (along the waterfall plot's horizontal axis) versus time (running vertically down the waterfall plot's vertical axis).

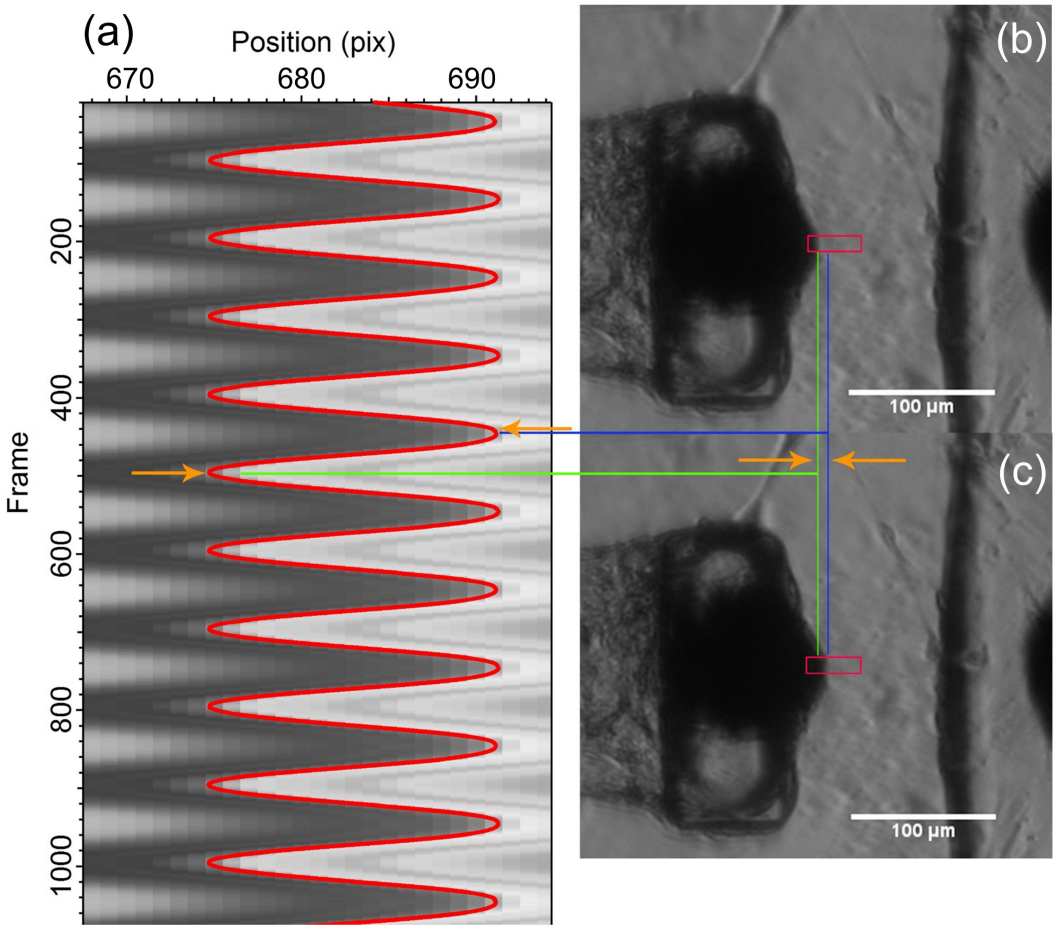

Figure 2.13 Pillar position tracking using phase microscopy. (a) A 'waterfall' plot was created by aggregating single-frame intensity traces (e.g. Figure 2.11d). In this example, the waterfall plot associated with the right-most micropillar is shown. Red line marks the x-position of high contrast edges determined through the fitting of intensity traces as described in Figure 2.12. (b) Phase microscopy image showing minimum deflection of right micropillar. Green line highlights the x-position of the edge of the pillar. (c) Micropillar at its maximum deflection, and its edge is highlighted by the blue line. Position of the red ROI box is preserved between (b) and (c). Orange arrows show the extent of micropillar deflection. Minimum deflection (green) is associated with horizontal 'valleys' in the waterfall plot, and maximum deflection (blue) is associated with horizontal 'peaks'.

Chapter 3 Microtissue design and validation

3.1 Introduction

Although μTUG devices had previously been used to construct microtissues composed of 3T3 fibroblasts, airway smooth muscle cells, and cardiomyocytes [26, 27, 30, 34], experimental parameters such as ECM concentration, cell seeding density, and maturation time could not be directly carried over from these previous results but had to be determined for the BPA-SMCs microtissues. Ultimately, I chose experimental parameters in order to maximize stable microtissue morphology and longevity and to maximize the correspondence in force generation between engineered microtissues and *in vivo* tissue. Microtissues were also altered through treatment with biochemical agents to recapitulate results from established experimental systems and clinical outcomes in order to validate the μTUG device as a viable platform for pharmacological testing. Lastly,

microtissues were characterized as a mechanical system by modifying the levels of cellular contractility.

Microtissues formed using optimal experimental parameters exhibited tissue morphology reminiscent of that of microtissues formed with other cell types. Immunofluorescent staining for collagen, cell nuclei, and actin stress fibers showed uniform distribution of collagen and cells, actin stress-fiber alignment along the main stress axis, and elongated nuclei long the long axis (Figure 3.1).

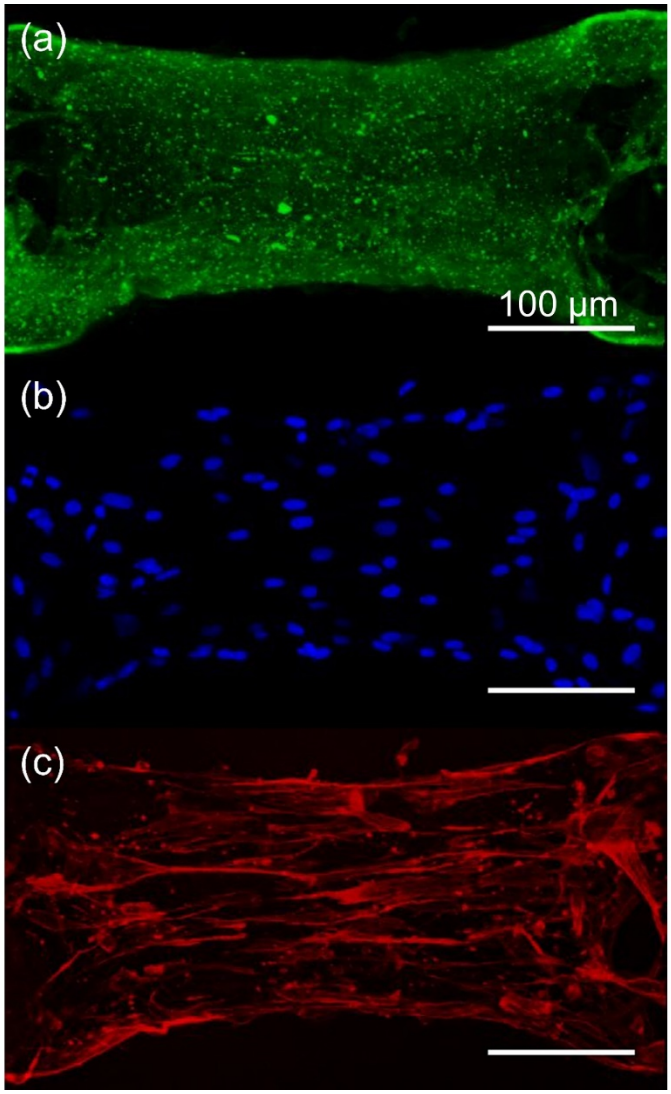

Figure 3.1 Microtissue morphology. (a) Collagen is uniformly distributed throughout the microtissue. (b) Cell nuclei staining shows elongation along the direction of the main stress axis, indicating that the cells are elongated. Cells are uniformly distributed throughout the microtissue. (c) Phalloidin staining of actin shows stress fiber alignment along the main stress axis.

3.2 Determination of experimental conditions

3.2.1 ECM and cell seeding density

Following the procedure outlined in §2.3.2, a range of ECM concentrations and cell seeding densities were tested. Collagen concentration ranged from 1 mg/mL to 2.5 mg/mL, and cell seeding density ranged from 200,000 cells/mL up to 2 million cells/mL. This range of cell seeding densities led to per microwell cell densities of 200 cells/microwell to over a few thousand cells/microwell (exact number cannot be determined due to optical occlusion). Fibrin concentration was held constant at 2 mg/mL because I found that using any lower concentration would not lead to viable microtissues.

Initially, ECM concentrations were held constant at 1 mg/mL collagen and 2 mg/mL fibrin while cell seeding density was changed from 500,000 cells/mL to 2 million cells/mL. In these early experiments to find the optimal conditions for microtissue engineering, 33 μg/mL of aprotinin (Sigma A6103) was also added to the microtissue media in order to impede fibrin degradation and to increase the range of experimental parameters that gave good results [35]. Once the general range of the parameters had been found, parameter values were fine-tuned to obviate the need for aprotinin. As seen in Figure 3.2, varying cell seeding density while preserving ECM concentrations lead to very diverse tissue morphologies. All images were taken 48 hours post cell seeding.

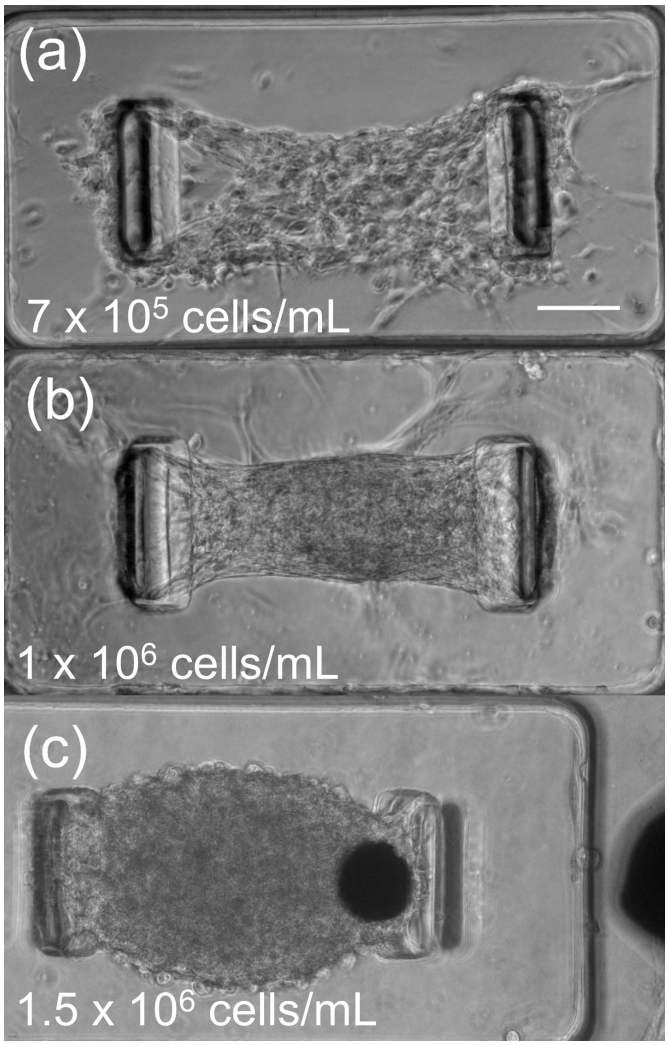

Figure 3.2 Initial determination of optimal microtissue engineering parameters. All microtissues here seeded with ECM concentrations of 1 mg/mL collagen and 2 mg/mL fibrin. (a). 700K cells/mL seeding density lead to a poorly formed, loose microtissue with poor force generation (evidenced by small deflection of pillars). (b) 1 million cells/mL allowed microtissue to form well, but again, did not provide much force generation. (c) Higher seeding density (1.5 million cells/mL) lead to thicker microtissues which generate more force. However, maximum force generation may be limited by the extent to which the microtissue can be compressed.

The microtissue in Figure 3.2b represents the microtissue conditions which produce the morphology with the highest potential for maximum force generation. I optimized around the parameters used for this particular microtissue, 1 million cells/mL seeding density, 1 mg/mL collagen, 2 mg/mL fibrin, and 33 μg/mL aprotinin, and found final microtissue seeding parameters.

Subsequent experiments which characterized microtissue properties and microtissue mechanical response were performed using the seeding parameters of 2.5 mg/mL collagen, 2 mg/mL fibrin, ~300,000 cells/mL, and no aprotinin. This cell seeding density lead to a density of 200-600 cells per microwell and reduced the variability in the

number of cells per well. The microtissues have a gel compaction ratio, the ratio between their final and original volume (i.e. the volume of the microwell less the volume of the micropillars), of ~10%.

Figure 3.3 below shows a few different morphologies due to changing parameters in microtissue creation.

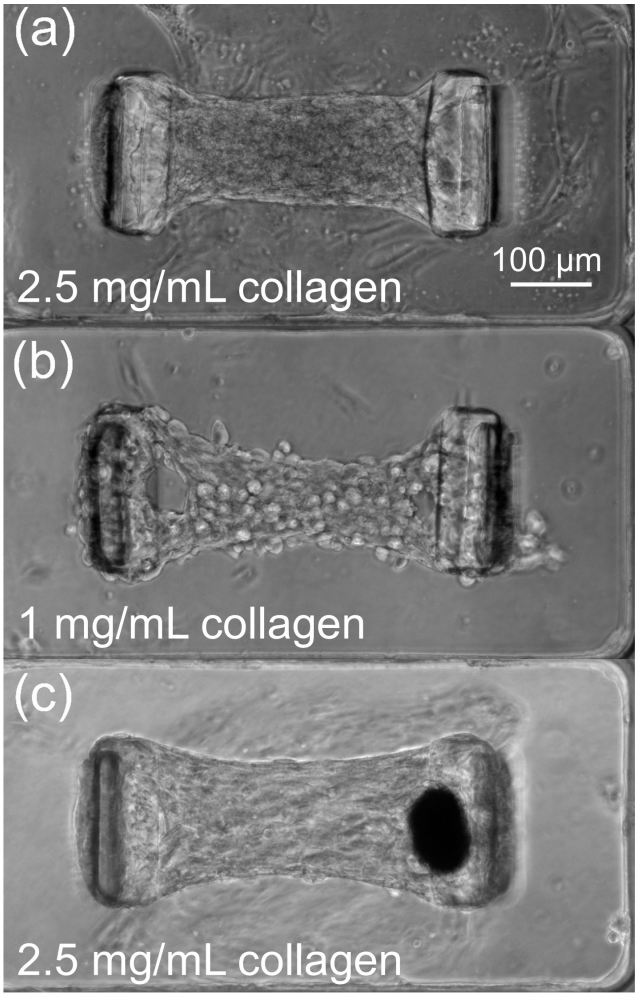

Figure 3.3 Final optimization of microtissue engineering parameters. (a) A 700k cells/mL seeding density combined with a higher collagen density (2.5 mg/mL) and no aprotinin additive allows a stable microtissue to form. (b) Maintaining a 1 mg/mL collagen density allows microtissue to form, but with a loose morphology. Microtissues seeded with a lower ECM concentration quickly tear off the micropillars due to THE contraction force of the cells– the ECM does not have the structural stability to support the forces generated by the cells. (c) Microtissue created with a cell seeding density of 300k cells/mL and 2.5 mg/mL collagen. This lower cell seeding density was used in subsequent experiments in order to reduce variability in the number of cells per well. All images taken at 48 hours after initial seeding except (b), which peeled off the micropillars within 24 hours. Microtissue shown in (c) includes the addition of nickel microsphere and is representative of control BPA-SMC microtissues used throughout this project.

3.2.2 Time required for stable microtissue formation

After optimal microtissue parameters had been determined, microtissues created using these parameters were monitored until endogenous force generation reached a plateau. Images were taken of microtissues every few hours up to 48 hours after seeding. Force generation plateaued before the 48 hour mark.

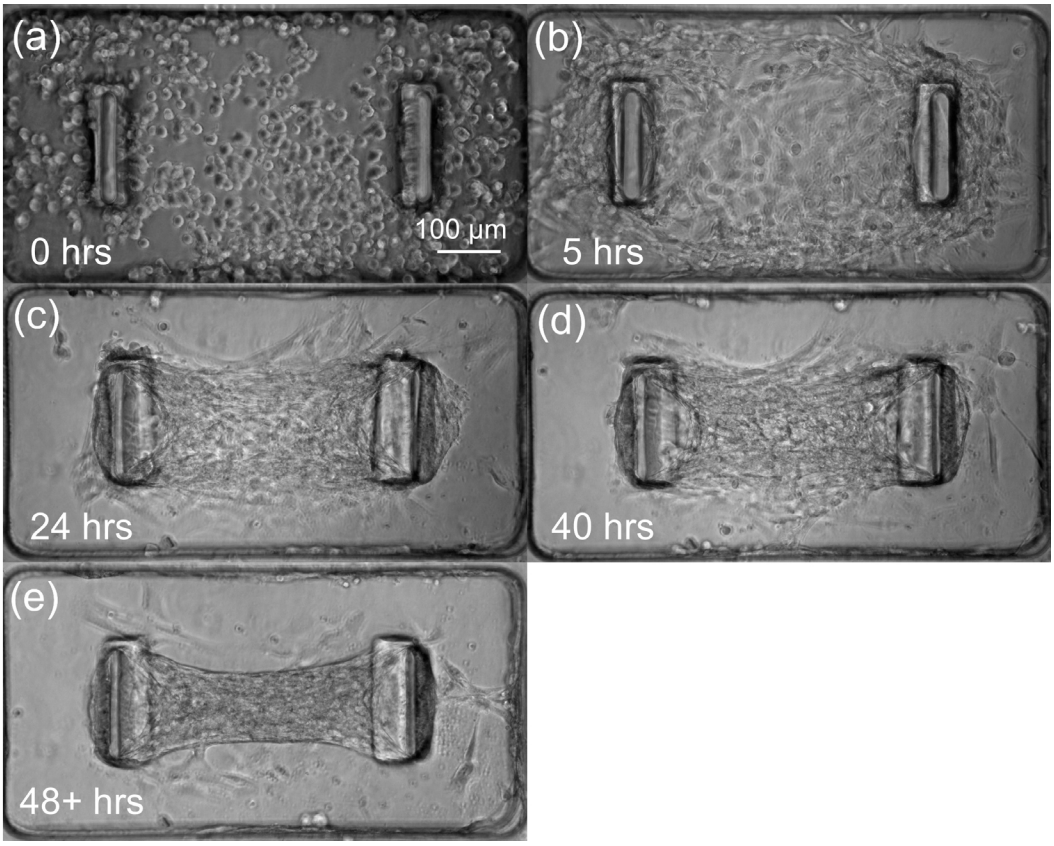

Figure 3.4 Microtissue formation sequence. (a) Immediately after seeding, cells are uniformly dispersed in the microwell. (b) ~5 hours after seeding, cells have elongated and have begun contracting towards the center of the microwell. (c) ~24 hours after seeding, microtissue has reached a recognizable morphology. (d) ~40 hours after seeding, microtissue morphology has almost reached final state. (e) Microtissue morphology reaches final state by 48 hours after seeding.

Figure 3.4 above shows the time evolution of microtissue morphology immediately after cell seeding to 48 hours post seeding. Immediately after cell seeding, individual cells are discernable in the micrograph, and it is at this stage where a cells/microtissue count can be undertaken. As the microtissue matures, it contracts towards the center of the microwell due to the forces generated by the cells. However, this movement is constrained by the micropillars, and the microtissue begins to form a 'dogbone' shape with concave boundaries. The deflection of the micropillars also simultaneously report the force generated by the forming microtissues, and this force can be monitored throughout the formation process as seen in Figure 3.5 below. Microtissues developed force fairly linearly until a peak near 24 hours after which endogenous force plateaued. Due to this pattern in force generation, subsequent experiments involving force application were performed at 48 hours post seeding when changes in endogenous force were small relative to total developed force.

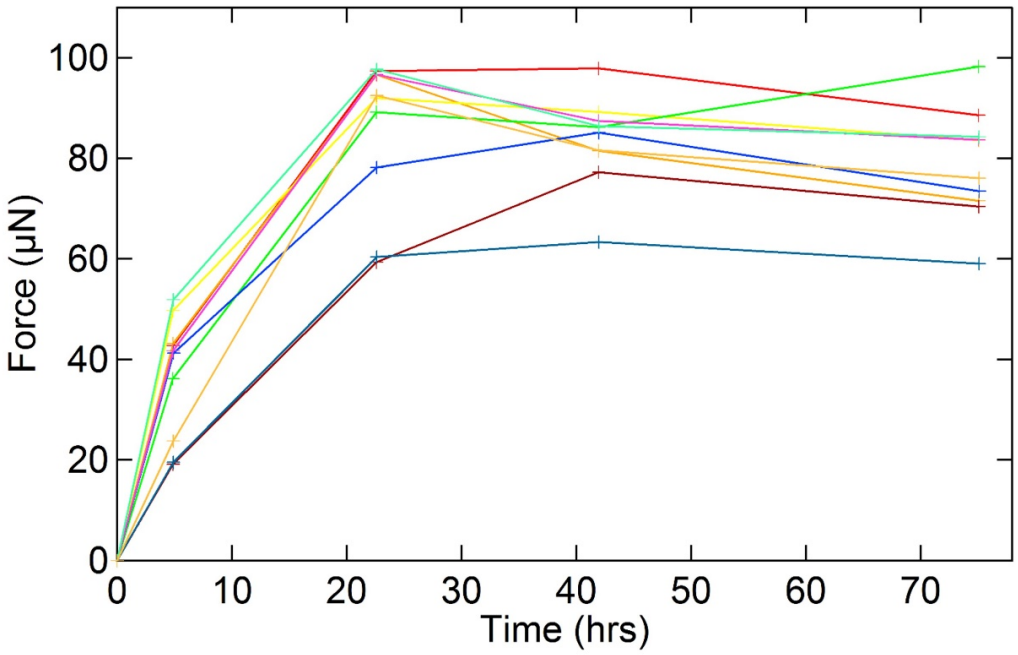

Figure 3.5 Microtissue force generation over time. The force generation of selected microtissues was recorded from the moment immediately after seeding to 78 hours post seeding. Microtissue force was seen to plateau by 48 hours. Simpler, linear post bending mechanics was used in this analysis as we are only concerned about the relative, and not absolute, changes in force generation.

3.3 Microtissue static force characterization

3.3.1 Standard conditions

With the optimal seeding parameters found in §3.2.1, each microtissue generates an average static force of ~300 μN. Each tissue comprised between 200-600 fairly uniformly distributed cells, and total tissue force generation scaled in a roughly linear manner with the number of cells within the tissue. Static tension can be converted to a static stress by dividing by the cross-sectional area of the narrowest portion of the microtissue. The average stress of each microtissue was 19 ± 5 kPa.

3.3.2 Response to biochemical agents

Microtissues were treated with a variety of biochemical agents in order to corroborate previous findings on different experimental systems and to validate the μTUG platform as a viable means of pharmacological testing. Y-27632, a known inhibitor of cellular contraction, was used to demonstrate the similarity in mechanical response to known biochemical agents between microtissues, single cells, and excised tissue. Nimesulide, a NonSteroidal Anti-Inflammatory Drug (NSAID), which inhibits cyclooxygenase-2 (COX-2), an inflammatory enzyme, potentially has important consequences for cardiovascular medicine and was used to demonstrate the ability of the μTUG system to act as a high throughput platform for testing the biomechanical effect of pharmaceuticals.

The ROCK (Rho associated protein kinase) pathway regulates cellular contraction in two ways: directly by promoting the contraction of actin fibers and indirectly by increasing the number of actin fibers. As illustrated in Figure 3.6, phosphorylated myosin light chain kinase (MLC) leads to actin fiber contraction. ROCK both phosphorylates MLC and suppresses MLC phosphatase, leading to increased levels of cellular contractility [36, 37]. Furthermore, ROCK indirectly suppresses the activity of cofilin, an actin disassembler, by activating LIM kinase, the protein upstream of cofilin [38]. ROCK levels are directly correlated with cellular contraction.

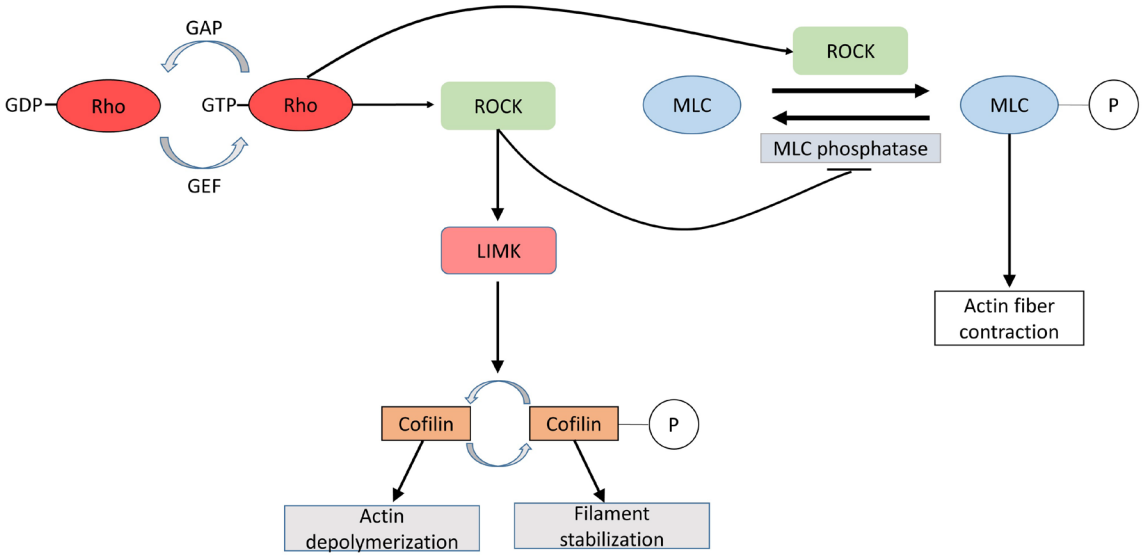

Figure 3.6 ROCK Pathway. Rho-GTP is an upstream activator of ROCK. ROCK phosphorylates myosin light chain kinase (MLC) as well as MLC phosphatase. These actions lead to actin fiber contraction. ROCK also stabilizes actin filaments through the LIMK-cofilin pathway. (adapted from [39])

Y-27632 inhibits ROCK, leading to fewer stress fibers and lower cellular contraction as seen in 3T3s, cardiac myofibroblasts, and human mesenchymal stem cells [2, 40, 41]. Microtissues were cultured in media containing 1 µM Y-27632. Figure 3.7 shows the dramatic effect of Y-27632 treatment. Tissue morphology and baseline stress of treated tissues were markedly different from control tissues.

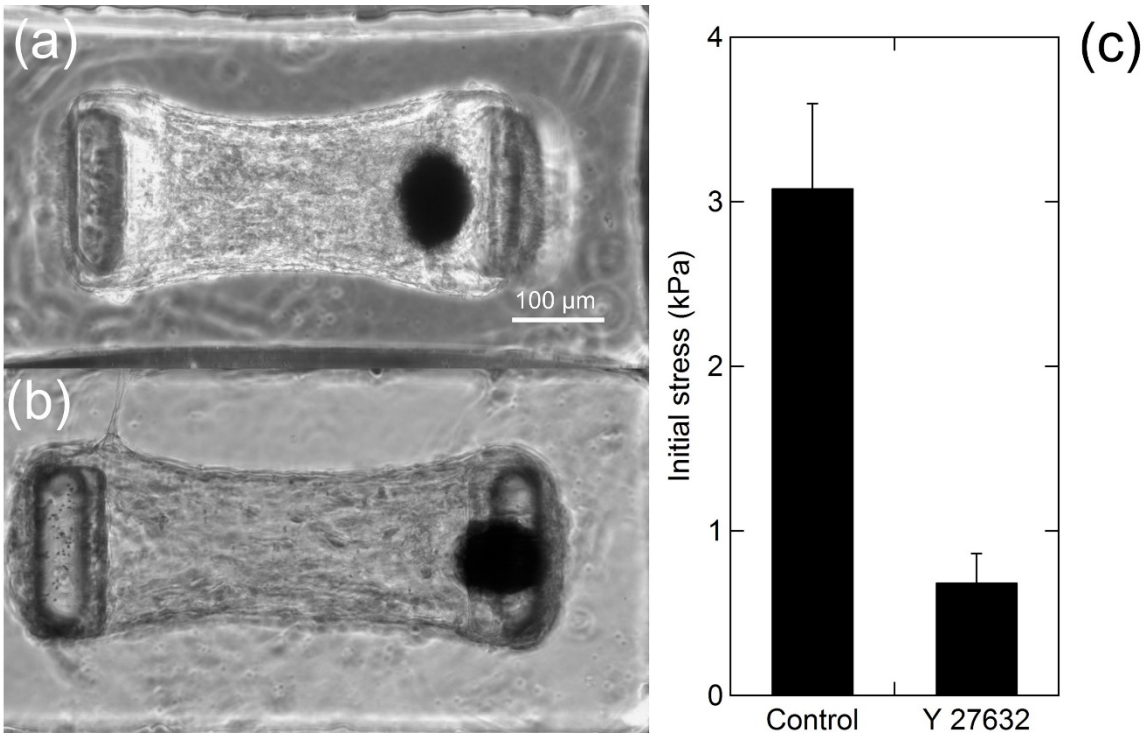

Figure 3.7 Effects of Y-27632 treatment. Treating microtissues with a 1 µM of Y-27632 decreases cellular contraction. (a) Control microtissue displayed more coherent and compact tissue morphology. Scale bar: 100 µm. (b) Y-27632 treatment lead to diminished contractile force and thus a longer microtissue. (c) Static, baseline stress for Y-27632 treated microtissues was 22% that of control microtissues (n=4, $p < 0.002$).

Nimesulide is a cyclooxygenase-2 (COX-2) inhibitor. These inhibitors are a class NSAIDs which result in fewer adverse gastrointestinal events compared with traditional NSAIDs [42, 43]. However, the use of COX-2 inhibitors also leads to higher blood pressure and risk of adverse cardiovascular events, [44-47]. To ascertain whether COX-2 inhibitors induce changes within the vasculature which might explain increases in blood pressure, microtissues were cultured in media with 2 µM nimesulide. Initial stresses generated by nimesulide treated tissues were almost double that of corresponding control tissues (Figure 3.9). In these experiments, nimesulide was introduced into tissue culture medium by dissolving solid nimesulide in dimethyl sulfoxide (DMSO) to 20 mM and

then by mixing this solution into normal tissue media to the working concentration of 2 μM. The media used to culture the corresponding control microtissues include the equivalent concentration of DMSO as in the nimesulide case in order to account for the effect of DMSO on the experiment.

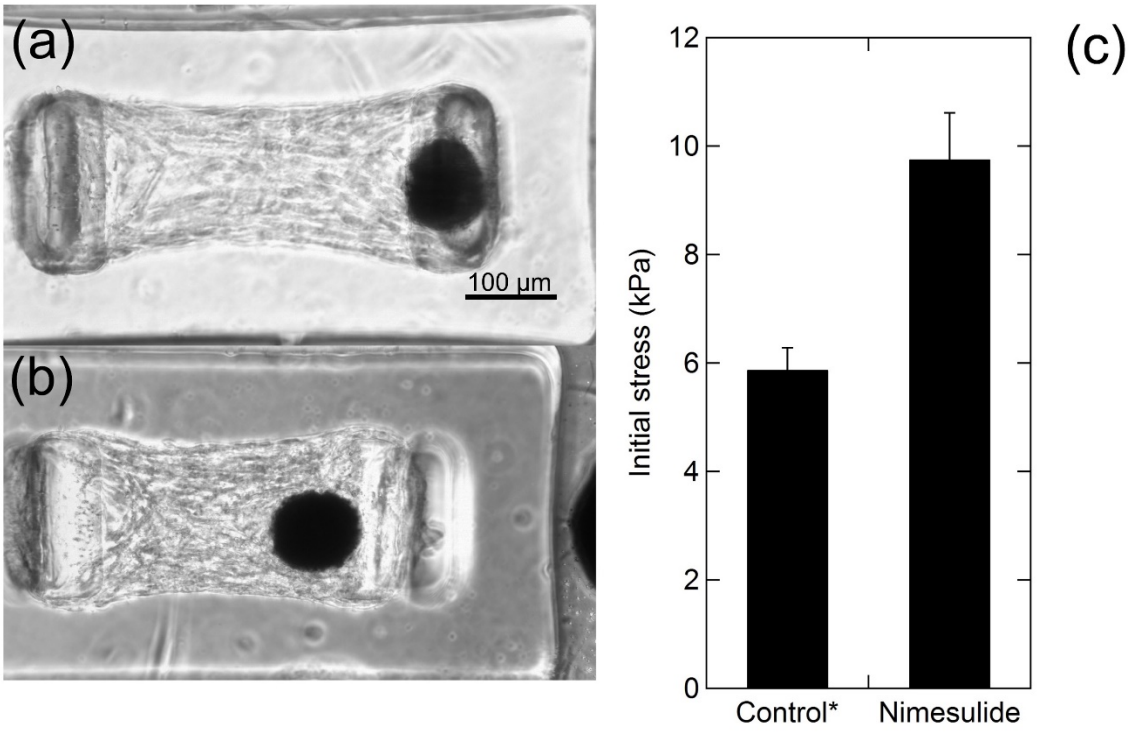

Figure 3.8 Nimesulide treatment. Morphologically, control (a) and nimesulide treated (b) microtissues appeared similar. (c). Nimesulide treated microtissues, however, exhibited 1.7 times the contractility as control; note higher levels of pillar deflection in (b) ($p < 0.001$). * "Control" here refers to DMSO control.

Because Y-27632 and nimesulide affect the structural stability of the tissues, causing them to detach from the micropillars, data for these two sets of experiments were taken after 1 day of maturation. Coherent tissue morphology was validated before data was recorded.

3.3.3 Response to modifications to force generation

The structure and mechanical behavior of the microtissues can be thought of as a synergistic interplay between the SMCs which actively generate contractile force and the extracellular matrix which passively contributes to the tissues' biomechanical properties. To divorce this interplay, SMC force generation was either enhanced by constitutively activating Rho-V14 or eliminated by lysing the cells. An adenovirus construct with constitutively active Rho-V14, the upstream activator of ROCK (Figure 3.6), was added to tissue growth media 24 hours post cell seeding in order to increase cell contractility [2]. To lyse cells, microtissues were treated with a 0.1% solution of Triton X-100, a detergent, for 10 minutes immediately before data collection. Importantly, Triton X-100 has no discernable effects on the mechanical structure of the extracellular matrix over this treatment time [27, 48].

Unsurprisingly, Rho-treated tissues experience more stress than control and Triton-treated tissues (Figure 3.9d). Mechanical inputs to these two different types of tissues will elucidate further implications of the Rho and Triton treatment.

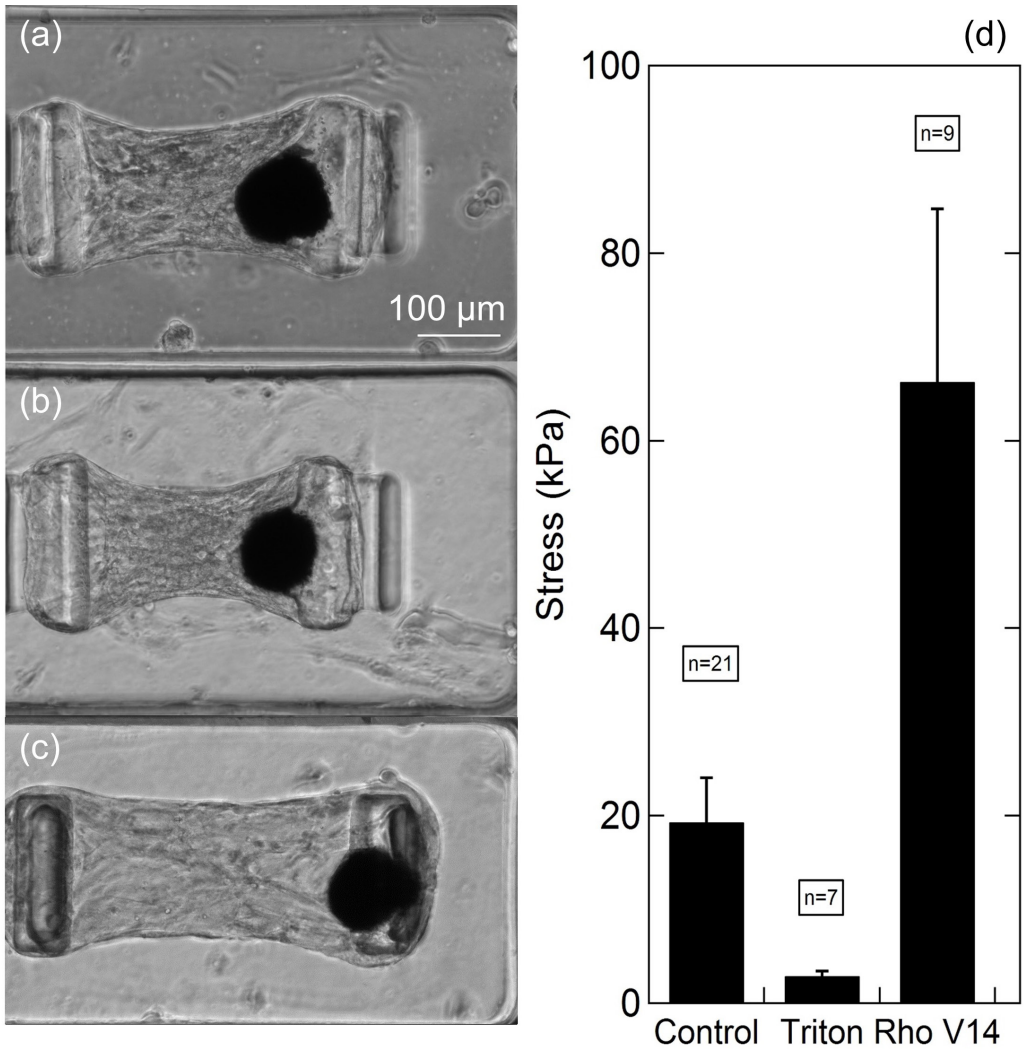

Figure 3.9 Effects of microtissue structural changes. (a) Control microtissues generated static stresses in between that of (b) virus treated microtissues and (c) Triton treated microtissues; note amount of deflection of the micropillars. (d) Control microtissues generated approximately 3 times as much static stress as Triton treated microtissues and approximately 1/3 as much stress as virus treated microtissues ($p < 0.005$).

3.4 Discussion

3.4.1 Standard conditions

We have been able to engineer BPA-SMC microtissues which require significantly less material and three times less maturation time than similar macro-scale engineered tissues [21]. Compared with 3T3 fibroblast based microtissues, which have been extensively studied before, these SMC based microtissues show similar morphology but an approximately order of magnitude higher static stress generation (~20 kPa compared with ~2 kPa) as would be expected for cells responsible for maintaining vascular tone compared with cells responsible for ECM synthesis [26, 33]. The engineered microtissues recapitulate very well the mechanical properties of *in vivo* bovine arteries. Bovine blood pressure in the pulmonary artery is approximately 40 mm Hg [49]. Bovine pulmonary arteries which have a uniform population of well-differentiated SMCs in their *tunica media*, have diameters <1500 μm [50]. Calculating the associated circumferential stress of an artery with a diameter of ~ 1500 μm and the thickness of our microtissues (~100 μm) results in a value of ~40 kPa, which compares favorably with the equilibrium stress of the microtissues, 19 kPa [51]. To increase the equilibrium stress of the microtissues to better match that of real arteries, stiffer micropillars or a higher collagen density could be used to form the microtissues [52].

3.4.2 Biochemical treatment

Treating microtissues with the biochemical agents Y-27632 and nimesulide demonstrates that microtissues respond in a predictable manner to known drugs and validates the SMC-μTUG system as a potential device for pharmacological testing.

Y-27632 treatment greatly reduces the stress generated by the microtissues compared with control culture conditions. This result recapitulates the mechanical effect of Y-27632 treatment on excised tissue and single cells [40, 53]. The similarity in these effects suggests that the μTUG system, which sits at a length scale between that of excised tissue and single cells, does not inhibit the diffusivity of small molecules and reacts appropriately to these compounds.

To prototype the μTUG system as a platform for biomechanically related pharmacological testing, microtissues were treated with the COX-2 inhibitor, nimesulide, to investigate if mechanical changes in arterial tissue could explain the increased risk of adverse cardiac events associated with the use of COX-2 inhibitors. As seen in Figure 3.8, nimesulide increases the baseline force generated by the microtissues. In a clinical setting, stiffer blood vessels are associated with hypertension and thus nimesulide may produce undesirable cardiovascular outcomes by affecting the mechanical properties of the vasculature [54, 55]. The μTUG system may one day see further use in explaining clinical observations.

3.4.3 Changes to force generation

The ability to separate and identify cell and matrix contributions to tissue mechanical properties are crucial to current bioengineering applications where the

relative mechanical properties of cells and matrix are integral to the formation and longevity of engineered tissues [26, 37]. Furthermore, this ability will be paramount for the future as bioengineering efforts more and more involve stem cells whose fate is partially determined by the external mechanical environment [2, 56].

Chapter 3 has shown that stable microtissues can be formed which generate similar amounts of stress when compared to *in vivo* tissue. These microtissues also demonstrate appropriate behavior when exposed to biochemical agents. By applying an external force to control tissues and tissues which have undergone the Triton treatment described in §3.3.3, dynamic mechanical properties of the tissue can be found, and the separate contributions of active cell mechanics and passive ECM mechanics can be determined. From this data, a mathematical model can be developed for the mechanical response of the microtissues. This will be the topic of the next chapter.

Chapter 4 Delineation of cell and matrix response to applied force

4.1 Introduction

The reciprocal relationship between cells and the surrounding extracellular matrix is fundamental to the structure and function of tissues. This interplay affects such diverse processes as matrix remodeling [57], cell proliferation [58], and intracellular signaling [59]. Cell-populated collagen gels have long been used as a simple model system that recapitulates the 3D environment which cells experience *in vivo* [60]. Mechanical testing using excised and engineered tissues have led to the development of many mathematical models that attempt to explain the tissues' response to an external stretching force. These models are diverse, and collectively they contain aspects of viscoelasticity and viscoplasticity [23, 61-63]. However, with these models, it is difficult to determine the relative contributions of the mechanically active cells and the mechanically passive ECM to these material properties.

To make this determination, I will present the use of bovine pulmonary smooth muscle cells (BPA-SMCs) in engineered microtissues composed of hundreds of cells in order to investigate overall microtissue and separate cellular and ECM response to external mechanical input. Data from the doctoral work of my labmate, Craig Copeland, involving single cell strain gauges was used to corroborate the behavior of the cells seen in the microtissue studies [40, 64]. In collaboration with Hailong Wang and Dr. Vivek Shenoy at the University of Pennsylvania, a phenomenological mathematical model was developed to explain this behavior and was used to determine important stiffness, viscosity, and plasticity parameters for tissues and cells.

To determine the mechanical properties of SMCs, both microtissues and single cells were subjected to a stretch-unstretch-observation protocol. In microtissues, the cellular contribution to the mechanical response can be removed by Triton X-100 treatment, which lyses the cells, and can be enhanced by Rho-V14 upregulation. To study the response of microtissues and cells to an externally applied force, stress and strain were measured. We used these stress-strain curves to quantitatively determine mechanical parameters and show that our mathematical model can accurately recapitulate the combined response of both the active and passive elements of our model system. Our results revealed that the microtissues we have studied show a viscoplastic behavior, but that the cells and matrix contribute different components to these dynamics, with the active mechanics of the cells dominating the viscous properties of the microtissues while the plasticity is largely due to the ECM. Crucially, these experiments show that the cells can effectively “shield” the ECM from plastically yielding when under tension.

4.2 Microtissue response to applied force

In order to measure the time-dependent biomechanical response of model tissues to external mechanical stimuli, a mechanical force was applied to the microtissues as shown in Figure 4.1a. A stretch-unstretch protocol was applied wherein the applied magnetic force, $\mathbf{F}_{\mathrm{Mag,}}$ was steadily increased to 25-35 μN over 120 s, and then decreased to zero over a similar time interval. The pillar deflections for the microtissues under test were recorded by time-lapse phase contrast and fluorescence microscopy during force application and then for a 15 min interval after the cessation of the applied force. The deflection of the non-magnetic pillar reported the force, and the tissue strain was determined by the pillars' separation [27, 65]. Figure 4.1b shows the evolution of a microtissue's strain with time due to the $\mathbf{F}_{\mathrm{Mag}}$ shown in Figure 4.1a, and Figure 4.1c depicts the corresponding stress. The resulting stress-strain loop is shown in Figure 4.1d. Analogous data for two other microtissues are shown in Figure 4.3. Both the stress and the strain increased with increasing magnetic force, but while the peak in the stress tracked closely with that in $\mathbf{F}_{\mathrm{Mag.}}$, the peak strain lagged the peak stress by ~40 s, a hallmark of a viscoelastic response. At the cessation of applied force at time t = 240 seconds, the microtissues were still in a strained state, while the stress was lower than its initial value. Over the subsequent observation period, the tissues recovered to close to their initial states, but with some residual strain. This suggests that plasticity may play a role in the microtissues' dynamics.

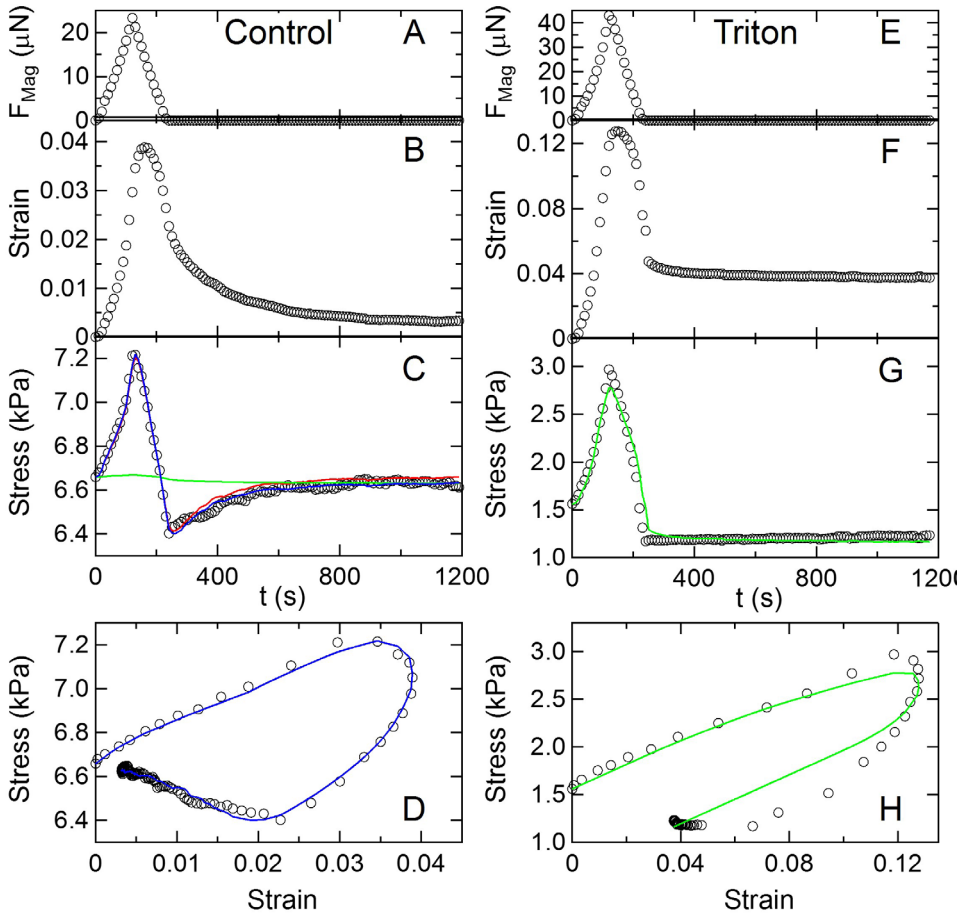

Figure 4.1 Dynamic response of untreated control microtissues and Triton X-100 treated microtissues to magnetic forcing. (a) Magnetic force profile $\mathbf{F_{Mag}}$. vs. time *t* applied to Ni sphere on control microtissue. Resulting (b) strain and (c) stress profiles, and (d) stress-strain curve. (e)-(h) Corresponding results for a Triton-treated microtissue. The control tissue's response is characterized by an active recovery to close to its initial state. The Triton-treated tissue shows plastic deformation. The blue curves in (c) and (d) are the result of a fit to the model described in the text and shown in Figure 4.5. The red and green traces in (c) show the cell and ECM contributions to the stress, respectively, as determined from the model. The green curves in (g) and (h) are a fit encompassing ECM contributions of the model only. The parameters for these fits are summarized in Table I.

The residual strain observed in the tissues following force application indicates that plasticity is present in the tissues' dynamics. This property is seen more clearly in the behavior of tissues after lysing the cells with a 0.1% solution of Triton X-100 (§3.3.3) to remove any active cellular processes from the microtissues' force dynamics. Triton-

treated microtissues generally showed similar morphologies to untreated control tissues, but with reduced baseline stress (Figure 4.1g), as expected from the lysis of the cells. The response of a Triton-treated microtissue to the stretch-unstretch actuation is shown in Figure 4.1e-h and data for two additional such microtissues are shown in Figure 4.4. Their initial response to the stretch-unstretch actuation was qualitatively similar to the control tissues, although with reduced initial stiffness, as measured by the initial slope of the stress-strain curves (Figure 4.1h and Figure 4.2). Rho V14 adenovirus-treated tissues also had qualitatively similar stress-strain responses, but with higher stiffness when compared with control tissues. The average stiffness for untreated tissues was 140 ± 20 kPa while that for Triton-treated tissues was 42 ± 9 kPa. Tissues with upregulated Rho-V14 had the highest stiffness, 270 ± 60. The Triton-treated microtissues notably were significantly stretched permanently, as shown in Figure 4.1f, and showed no recovery toward their initial state after the cessation of applied force, as illustrated in Figure 4.1g and the corresponding stress-strain loop in Figure 4.1h. This behavior is recapitulated in the microtissues shown in Figure 4.4. Virus tissues, however, showed dramatic recovery responses (Figure 4.6). These results show that the recovery observed in the control tissues is due to active mechanical processes in the cells, and importantly, also suggest that the observed plasticity may be predominantly contributed by the ECM. Notably, modeling the virus-treated tissues showed an almost complete dominance by the active cellular mechanics.

.

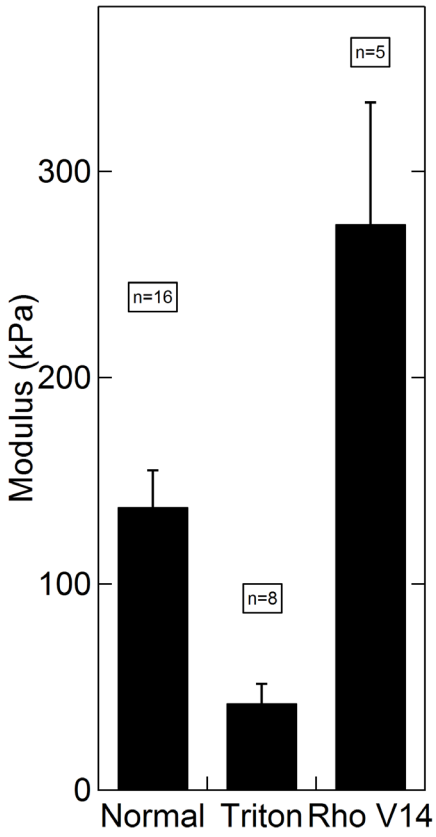

Figure 4.2 Microtissue modulus. Analogously to microtissue stress, microtissue modulus was the lowest in Triton-treated tissues and highest in RhoV14 upregulated tissues.

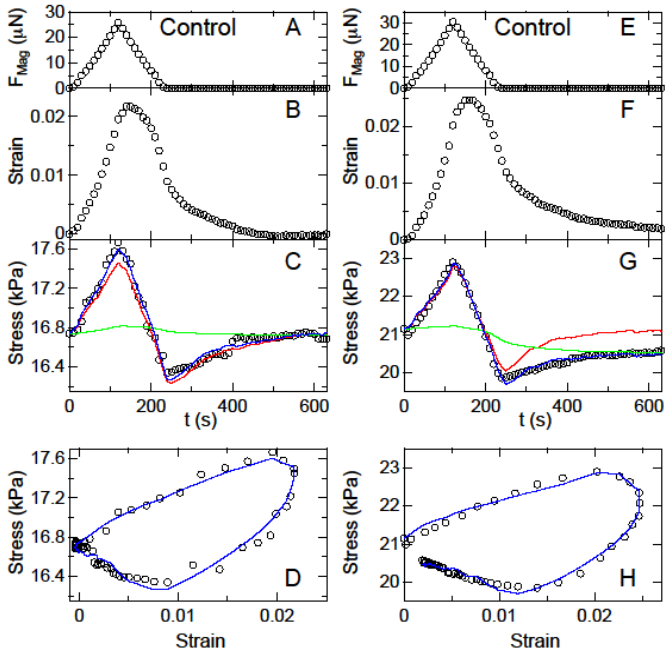

Figure 4.3 Two further examples of control tissues. Blue is the overall mathematical fit to experimental data; red and green are the cell and matrix contribution, respectively, to the overall fit.

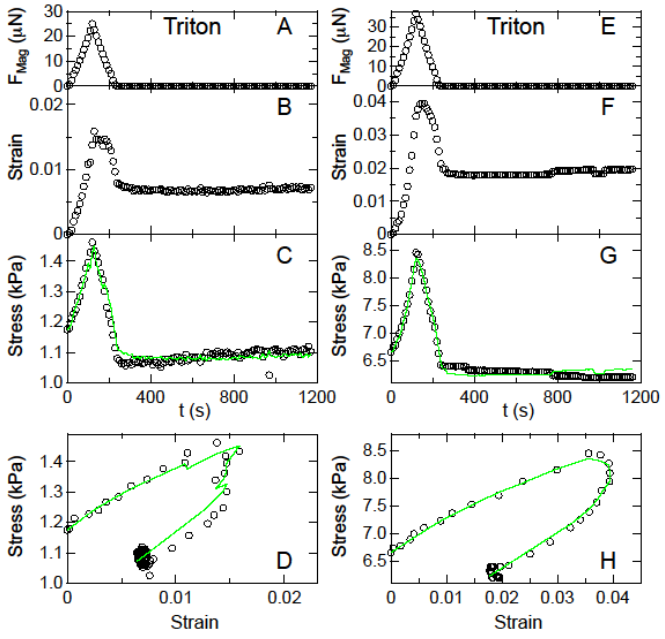

Figure 4.4 Two further examples of Triton treated tissues. Blue is the overall mathematical fit to experimental data.

4.3 Mathematical model of microtissue mechanics

In order to better describe this behavior and to quantitatively determine the material parameters of our constructs, we developed a four-element phenomenological mathematical model for the biomechanical response to applied force and used it to fit the data from our tissue and single cell experiments (Figure 4.5).

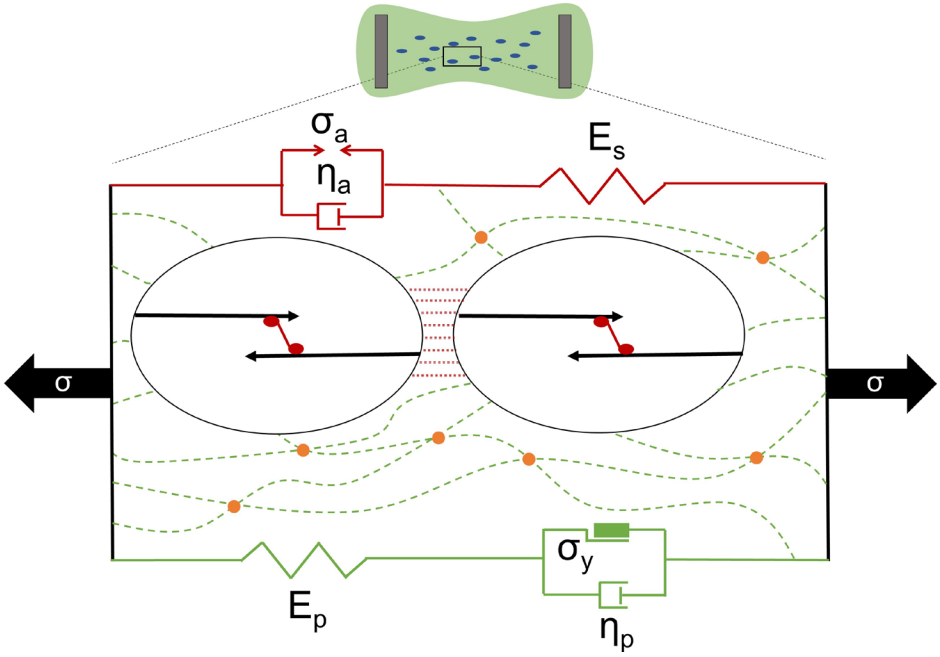

Figure 4.5 Mathematical model. Model for the mechanical response of the microtissues (shown at top). The model is shown above, where cell stiffness E_S (red) that includes internal cell stiffness (black) and cell-cell contact stiffness (dashed red) is modeled in series with an active contractile element (red) with constant active stress σ_a and active viscosity η_a. Passive elements (in green) act in parallel to the active elements and represent the behavior of the ECM (green dashed lines), and include stiffness E_p and a plastic element with yield stress σ_y and plastic viscosity η_p. σ denotes the microtissue's stress.

This model builds upon previous work [66], but adds additional features to account for the potential effects of ECM plasticity. As shown in Figure 4.5, the model contains an active element with stress σ_a and viscosity η_a to represent the contractility of the cells in the tissue. It also contains two passive linear elastic elements, of which one, E_S, models the stiffness of the cellular actin filaments and the stiffness of any cell-cell contacts, and acts in series with the active element. The second, E_P, models the ECM stiffness, and any cellular components that may act in parallel with the active element.

The series stress can be written as:

$$\sigma_s = \sigma_a + \eta_a \dot{\epsilon}_a = E_s(\epsilon - \epsilon_a) \tag{4.1}$$

where σ_s is the stress in the top (series) branch, σ_a is the active stress, η_a is active viscosity, corresponding to the viscosity of the cells, ε_a is the strain in the active element, and ε is total strain. The parallel stress can be written as

$$\sigma_p = E_s(\epsilon - \epsilon_p) \tag{4.2}$$

where σ_p is the parallel stress and ε_p is the plastic strain.

The inelastic effects are modeled by an elastic-perfectly-viscoplastic Bingham-Norton element

$$\dot{\epsilon}_p = \begin{cases} \frac{1}{\eta_p}\left(\sigma_p - \sigma_y^c\right), & \sigma_p < \sigma_y^c \\ 0, & \sigma_y^c \le \sigma_p \le \sigma_y^t \\ \frac{1}{\eta_p}\left(\sigma_p - \sigma_y^c\right), & \sigma_p > \sigma_y^t \end{cases} \tag{4.3}$$

where σ_p is the stress in the bottom branch (ECM component) of the model in Figure 4.5, is the plastic strain, σ_y^c and σ_y^t are the compressive and tensile yield stresses, respectively. η_p is plastic viscosity.

	Sample	Active viscosity η_a (MPa.s)	Series stiffness E_s (kPa)	Parallel stiffness E_s (kPa)	Yield stress σ_y^t (kPa)	Plastic viscosity η_p (MPa.s)
Control	C1	1.6	30.3	.9	σ_p^0 +0.004	0.01
	C2	3.8	82.7	7.8	σ_p^0+0.170	any
	C3	6.9	198.3	27.8	σ_p^0	0.28
Triton	T1	--	--	64.3	5.0	3.9
	T2	--	--	12.9	1.9	1.1
	T3	--	--	27.2	0.047	2.0
Virus	V1	44.4	897.8	6.0	σ_p^0	0.005
	V2	75.0	3768	0	any	any

Table 4.1 Fitting parameters. Fitting parameters for Control, Triton-treated, and virus-treated microtissues. Active cellular contractility is represented by series elements and matrix properties are represented by parallel elements. [From Hailong Wang]

To compare the model to the data, the measured strain was taken as input, and the stress vs. time was fit by Hailong Wang using a custom C program that incorporated numerical solutions to the constitutive equations with a least-squares fitting algorithm (See Appendix 8.3). A representative best-fit curve for the fit to the full model for the control tissues is shown in Figure 4.1c,d and additional examples are shown in Figure 4.3. The fit parameters determined for these fits are shown in Table 4.1.

Since the cells' contributions to the tissues were removed by the lysing procedure, the Triton-treated tissues were fit with a reduced version of the model to describe the ECM (lower branch only in Figure 4.5). These fits are shown in Figure 4.1g,h and in Figure 4.4, and parameters from these fits are given in Table 4.1 as well. This reduced model provides a good description of the observed behavior, including the observed plasticity.

The fits to the data for virus-treated microtissues showed an almost complete dominance by the cells over the overall stress-strain response of the microtissues (Figure 4.6)

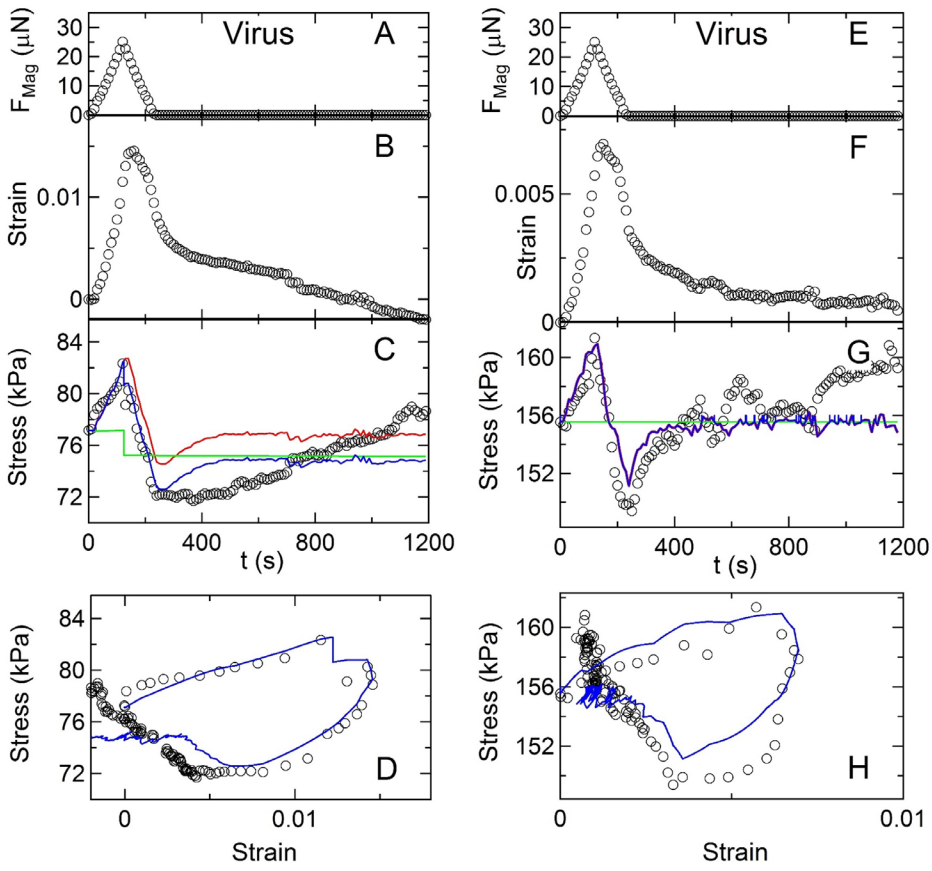

Figure 4.6 Virus-treated tissues. (a) Magnetic force profile $\mathbf{F}_{Mag.}$ vs. time *t* applied to Ni sphere on virus-treated microtissue. Resulting (b) strain and (c) stress profiles, and (d) stress-strain curve. (e)-(h) Additional example of virus-treated tissue. The blue curves in (c) and (d) are the result of a fit to the model described in the text and shown in Figure 4.2. The red and green traces in (c) show the cell and ECM contributions to the stress, respectively, as determined from the model. Of note here is that the matrix contribution is unimportant in this tissue condition (especially in panel G).

Figure 4.1c also shows the breakdown of the stress response as measured in the model fits into its "cellular" and "matrix" associated components. It can be seen that the cellular components are significantly larger than that of the matrix components of the

model. These results suggest that the cells dominate the active properties of these tissues. To provide independent input into the assessment of the cellular contributions to the microtissues' dynamic response, we measured the time-dependent mechanical response of single SMCs to stretch. These experiments were performed using micropost array detectors (mPADs) [64, 67] which we have previously demonstrated are effective in recording the contractility dynamics for these SMCs [68]. For these experiments, we used stretchable mPAD arrays (Figure 4.7) [9, 69] fabricated on thin PDMS membranes, and applied biaxial strain with a custom-built vacuum-actuated stretching device [40]. As illustrated in Figure 4.7, the cells were linearly strained by ~10% over 3 minutes and then unstretched over the same time interval, followed by a 15 min. strain-free observation period similar to that employed for the microtissues. Figure 4.7c,d illustrates the increase in the subcellular forces as a cell is stretched. Figure 4.7f shows the time evolution of the summed magnitudes of the individual forces exerted on the microposts, $F = \sum_i |\boldsymbol{F}_i|$, which provides a measure of the overall contractile state of the cell. Plotting this total force vs. strain in Figure 4.7g shows a response reminiscent of that seen for the microtissues: the total cellular force is lower than its initial value at the cessation of applied strain, and this total force recovers toward its initial values during the 15 minute observation period at the end of the forcing protocol.

As shown by the fit curves in Figure 4.7f,g, the single-cell dynamics can be described using only the top branch of the overall model (Figure 4.5), and from these fits, we can determine the average active viscosity, η_a^c, of an individual cell to be 3 x 10^5 nN.s (n=4).

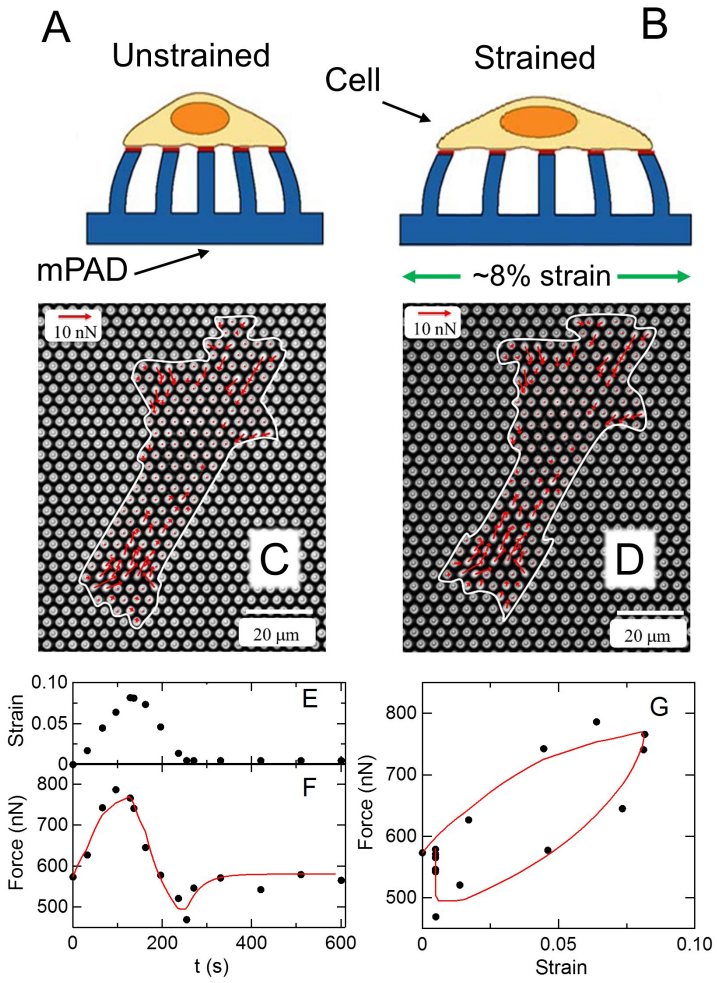

Figure 4.7 Single cell stretching. (a) Sideview schematic of cell adhered to micropost substrate (mPAD) in unstretched conditions. The magnitude and direction of the deflections of the microposts are used to determine the forces exerted by the cell. (b) As the underlying mPAD substrate undergoes biaxial stretch, so too does the adherent cell. (c) Micrograph of SMC on an mPAD substrate. The microposts had diameters of 1.8 µm, spacing 4 µm, height 5.7 µm, and an effective spring constant for small lateral deflections of 22 nN/µm. Red arrows show measured cellular forces, and the outline of the cell is shown in white. (d) shows change in cellular forces upon application of 8% strain. (e) Strain profile applied to mPAD substrate results in the increases in cellular force shown by the circles in (f). (g) The force-strain curve shows viscoelastic response and recovery reminiscent of that observed in the microtissues. The red curves in (f) and (g) are a fit using solely the cellular components of the model shown in Figure 4.5. Data from [40]

From this value of the active viscosity of a single cell, the active viscosity of an entire microtissue, η_a^t, can be estimated using the volume of the microtissue, V_t, and the number of cells per the microtissue, *N*:

$$\eta_a^t = \frac{N^{\frac{2}{3}}\eta_a^c}{(V_t)^{\frac{2}{3}}} \tag{4.4}$$

The reasonably close agreement between the values for η_a^t obtained through this calculation, and the values for the active viscosity derived from the fits to the microtissue data (Table 1), together with the lack of stress recovery in the triton treated tissues (Figure 4.1) support the conclusion that cellular actomyosin active mechanics dominates the active dynamics of the microtissues. Table 2 below compares tissue viscosity estimates derived from single cell viscosity measuements as well as from fitting tissue stress-strain data. As additional confirming evidence for the dominance of active cell processes, we note that microtissues formed from cells expressing constitutively active Rho to upregulate myosin activity also show significant increases in both baseline stress (Figure 3.10(d)) and initial stiffness (Figure 4.2, Table 1)

Sample	Fitted active viscosity η_a (MPa.s)	Estimated active viscosity η_a (MPa.s)
C1	1.6	0.55
C2	3.8	0.71
C3	6.9	0.66
Average	4.1	0.64

Table 4.2 Tissue viscosity. Tissue active viscosity found using two different methods give close agreement.

4.5 Discussion

The microtissues are a composite system, consisting of smooth muscle cells and extracellular matrix. Their behavior as a whole incorporates the passive plastic properties of the ECM and the active contractile properties of the SMCs. In this work, we were able to separately discern the mechanical properties of the whole microtissue, the microtissues' ECM, and the individual cells that compose the microtissue. However, these properties are not simply additive. Through mathematically modeling these mechanical properties, we see that the cellular component of the microtissues' response to external force dominates that of the ECM component (Figure 4.1). It is only when active cellular processes are removed that the properties of the supporting ECM are strongly manifested. The presence of the cells effectively masks the mechanical properties of the matrix from being expressed and shields the matrix from plastically yielding in tension.

Our picture of the coupling of the structure and mechanical dynamics of the individual microtissue components is outlined in Figure 4.8. As shown in Figure 4.8, when the cell/ECM mixture is initially seeded (Point A), it evolves via cell contractile action to form the microtissues (Point B), with compressive stress developing as the ECM contracts. The irreversible nature of this contraction implies that the ECM has reached its point of compression yield. Additional ECM crosslinking also occurs during this process due to matrix remodeling by the cells. The mechanical loading and unloading of the tissues during our magnetic forcing experiments causes the microtissues to travel around the path in Figure 4.8 between Point B and Point C. In the stretched state (Point C), the

shielding of the ECM by the cells is apparent, as the ECM is stretched but not deformed plastically.

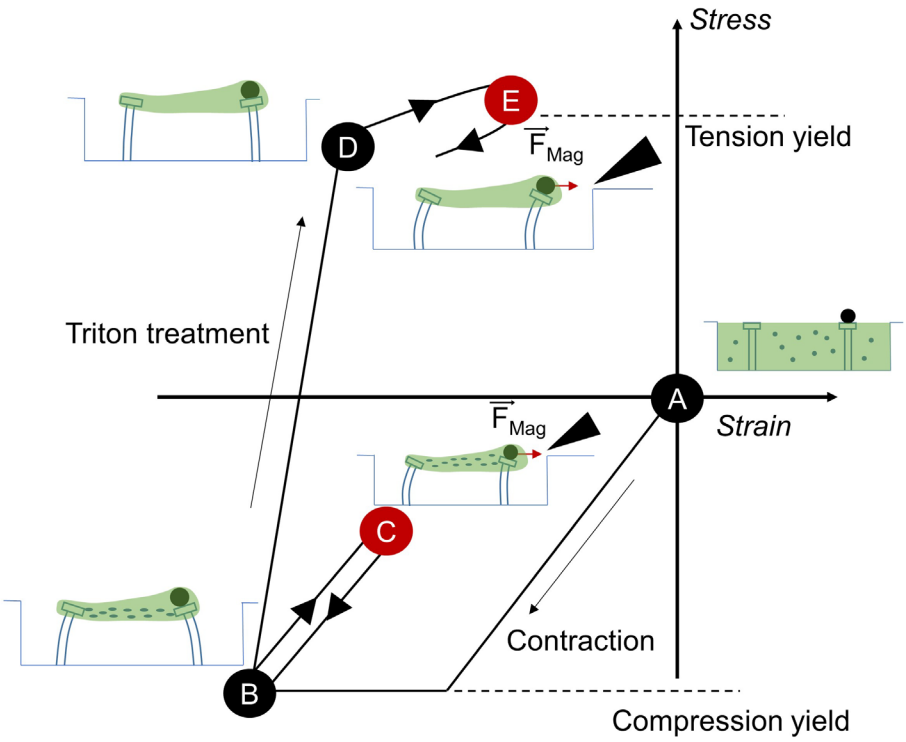

Figure 4.8 Phase space diagram of microtissue mechanical behavior. Inset figures show the relative deflection of the micropillars as the microtissue travels around this space. Red indicates that the magnetic field is active. We define the moment of cell seeding (Point A) to be the zero stress and zero strain condition. Micropillars are completely vertical. As the microtissue matures, cell contraction causes the microtissue to undergo compression (Point B) Mechanical loading and unloading causes untreated microtissues to travel around the path between point B and point C, where the maximum strain is experienced. Treating microtissues with Triton X-100 lyses the cells. The microtissues are now under tension instead of compression due to the outward stress exerted by the micropillars with no active cellular contraction to counterbalance this stress. Applying the loading profile to Triton-treated microtissues causes them to move from point D to point E. However, these microtissues never fully recover to point D as they plastically deform due to the mechanical loading.

Upon cell lysis (Triton X-100 treatment), the cessation of the cells' myosin machinery removes the ECM from its state of compression, and instead it shifts to a state of tension (Point D) due to the action of the micropillars' spring forces that are

attempting to restore the pillars to a vertical orientation. The micropillars, however, are still deflected inward after Triton treatment. When the magnetic forcing stretches the tissue (Point E in Figure 4.8), the cells are no longer present to shield the ECM. The ECM yields under tension and undergoes plastic deformation.

This residual tension that remains in the microtissues following Triton treatment indicates that the ECM had yielded in tension during the tissue formation process. This behavior may be attributed to collagen compaction and subsequent crosslinking during the formation process. The average viscosity associated with the matrix, 3.5 MPa.s (Table 1) also hints at high levels of crosslinking, as pure collagen gel treated with a relatively high concentration of 0.2% glutaraldehyde, a compound which enhances collagen cross-linking, only has a viscosity of ~0.63 MPa.s [70].

The matrix-shielding effect seen in our SMC microtissues is different than that seen in other cell/matrix constructs. Measurements that probed the cell and matrix contributions to the mechanical properties of fibroblast populated collagen microtissues have shown relatively equal contributions of these two components to the tissue stiffness [27]. Furthermore, the SMC microtissues had an order of magnitude higher stiffness [27]. At a high level, the difference in behavior between SMC and fibroblast microtissues may be due to the dissimilar roles that these cells play within the body: arterial SMCs regulate vascular tone while fibroblasts produce ECM [71].

To explain force transmission through the microtissue, we use the inclusion model of Evans and Barocas: in collagen gels, cells have a radius of influence of approximately 150 μm, where, within that radius, the cells act to form “high density (and high modulus)” regions of collagen [72]. Direct imaging of fibroblasts in fibrin gels have also

shown areas of high density fibrous regions connecting individual cells [73]. Based on the volume and cell density of the microtissues, direct physical interaction between cells is unlikely. The microtissues include ~ 500 cells and have a volume of ~ 1 x 10^7 μm^3. Each cell is associated with a microtissue volume of 2 x 10^4 μm^3, or a cube with a side length of ~27 μm. However, the volume of each cell is approximately 2000 μm^3 (radius ~8 μm), and so nearest neighbors are approximately an entire cell diameter away [74, 75]. Additionally, the statistics of polymer networks also indicates that the cell density within these microtissues is not high enough to reach the percolation threshold, the density at which a contiguous body of cells is likely to form [76]. The concentration needed for percolation is defined as

$$C = N{l_0}^3 \tag{4.5}$$

where C represents the dimensionless number of cells per unit volume, N is the number of cells per unit volume and l_o is the initial cell length. The percolation threshold is C~11, whereas in these tissues, C~0.25.

With the inclusion theory, however, cell-cell coupling can take place through mediated interaction by high density collagen regions. Again, tissue volume, V, is ~1 x 10^7 μm^3. The radius of influence of a cell on its surrounding collagen is, R~150 μm. Dividing $V/(4/3\pi R^3)$~ 2.5 which is much less than the number of cells per microtissue, indicating that cellular areas of influence on collagen overlap. The idea of areas of high density, high modulus collagen are also supported by earlier modified versions of the Zahalak model of cell-ECM interaction in artificial tissue constructs [63]. In this model, at cell concentrations below the percolation threshold, cells experience hundreds of times

less strain than does the overall tissue construct during applied stretch—cells and the area around them, have a much higher stiffness than the surrounding matrix [61, 76].

The inclusion theory may also help explain the behavior of microtissues treated with BAPN, an inhibitor of collagen cross-linking. In fibroblast-populated microtissues treated with this compound, their stiffness decreased compared with that of control tissues [65]. BAPN may have reduced the radius of influence of the fibroblasts on the surrounding collagen and accordingly, the periphery of the high density regions may be more pliant (Figure 4.9).

This current study may have implications for future tissue engineering efforts. Previous work has shown that mechanically conditioning of vascular tissue constructs leads to more robust tissue properties [77, 78]. Building on the experimental and mathematical tools described in this work for the *in situ* mechanical conditioning of microtissues has the potential to provide a better fundamental understanding of how tissue mechanical properties change as the component cells and ECM develop and mature. This information can provide insights into the effects of tissue engineering parameters on the quality of the ultimate construct.

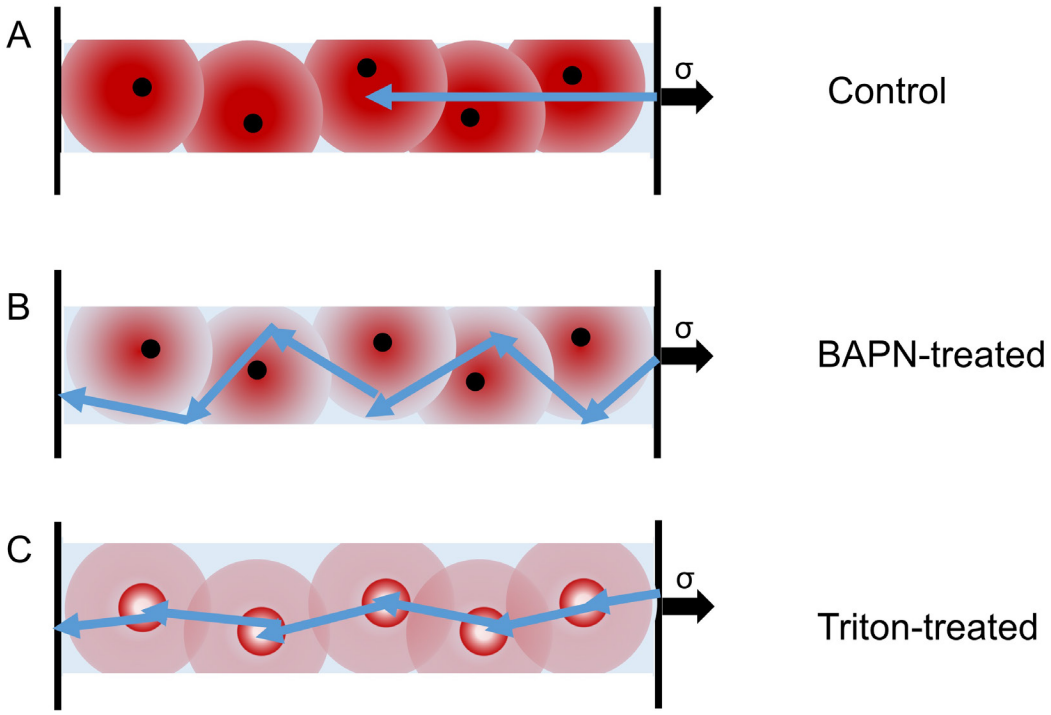

Figure 4.9 Microtissue microstructure. σ is applied stress (a) In control microtissues, cell density as well as local collagen and crosslinking density (represented by large red graded circles; redness indicates degree of density) in the area of each cell (solid black circles) is high enough such that force transmission (blue arrows) across the tissue necessarily has to pass through contiguous volumes of high local density associated with cells. Light blue represents less dense regions of collagen. (b) In BAPN treated tissues, the area of effect of high cell-associated crosslinking density may be reduced (graded red circles which are more blue). Force transmission across the microtissue now preferentially elongates collagen fibrils near the periphery of this region. Measured modulus is thus lower than non-BAPN treated microtissues, but is still higher than that of pure collagen gels. (c) Triton-treated tissues now have areas of weakness where cells once were. Measured modulus is now very low, but is higher than that of pure collagen gels.

Chapter 5 Microtissue response to repeated stimulation

5.1 Introduction

The previous chapter elucidated the mechanical properties of BPA-SMC microtissues through the application of a triangle wave pulse of force. The mechanical environment of tissues *in vivo*, however, are subject to more complex changes than a single increase and decrease in force. In this light, I subjected the microtissues to repeated strain loading at strain rates similar to those presented in Chapter 4 and to periodic, 1 Hz cycles in analogy to the strains experienced by the vasculature due to the pulsatile flow of blood. Untreated microtissues demonstrated active reinforcing behavior to multiple triangle wave inputs, while cell-free, treated microtissues did not. Microtissues to subjected to 1 Hz stimulation showed strain hardening.

5.2 Microtissue conditioning and relaxation

In order to investigate how microtissues respond to repeated actuations, I applied force profiles similar to those presented in Chapter 4. In this case, however, the typical triangle wave pulse was either applied 3 times in succession or 2 times with a 10 minute recovery interval in between. Microtissues were also treated with Triton X-100 (as in Chapter 4) as well as Trypsin-EDTA (Life Technologies) to investigate the response of the ECM to these applied forces. The experiments in this chapter were performed on stiffer microcantilevers which had a spring constant of 1 μN/μm, and a linear analysis was used to determine the force associated with the deflections.

5.2.1 Successive actuations

Using a similar procedure as outlined in Chapter 4, the microtissues were stretched through the application of an external magnetic force. This force consisted of three successive, symmetric triangle wave pulses, each lasting 240 s and reaching up to ~25 μN in magnitude. The total time for each actuation lasted around 700 s. Figure 5.1 below shows the typical magnitude and time course of the applied force.

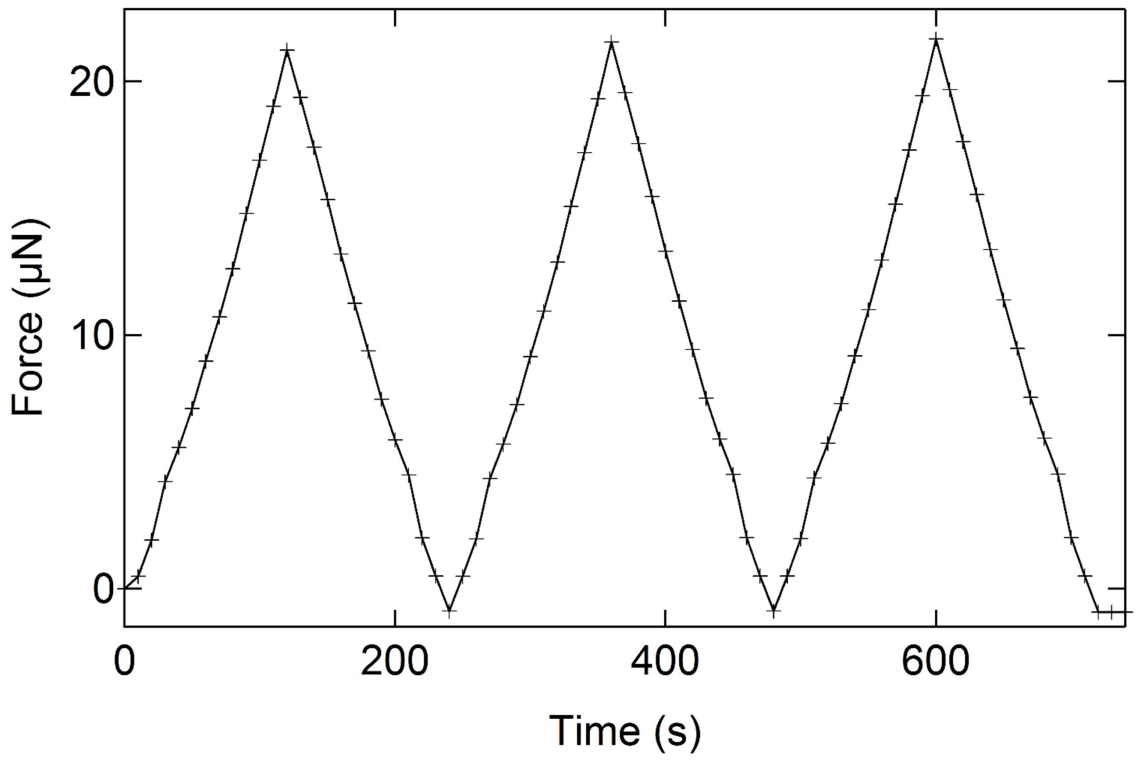

Figure 5.1 Force vs. time of successive actuations. Each symmetric triangle wave pulse had a period of ~240s. Force was increased and decreased linearly, with peak force reaching ~25 μN.

The stress-strain response of the microtissues was determined as described previously in Chapter 4; two representative examples are shown in Figures 5.2 below. Tissues were strained up to 7% and increased in stress by up to 2 kPA. Peaks in stress occurred at the same time points as peaks in the applied force profile. The broad peaks in strain, which lagged peaks in stress, highlight the viscoelastic nature of the microtissues.

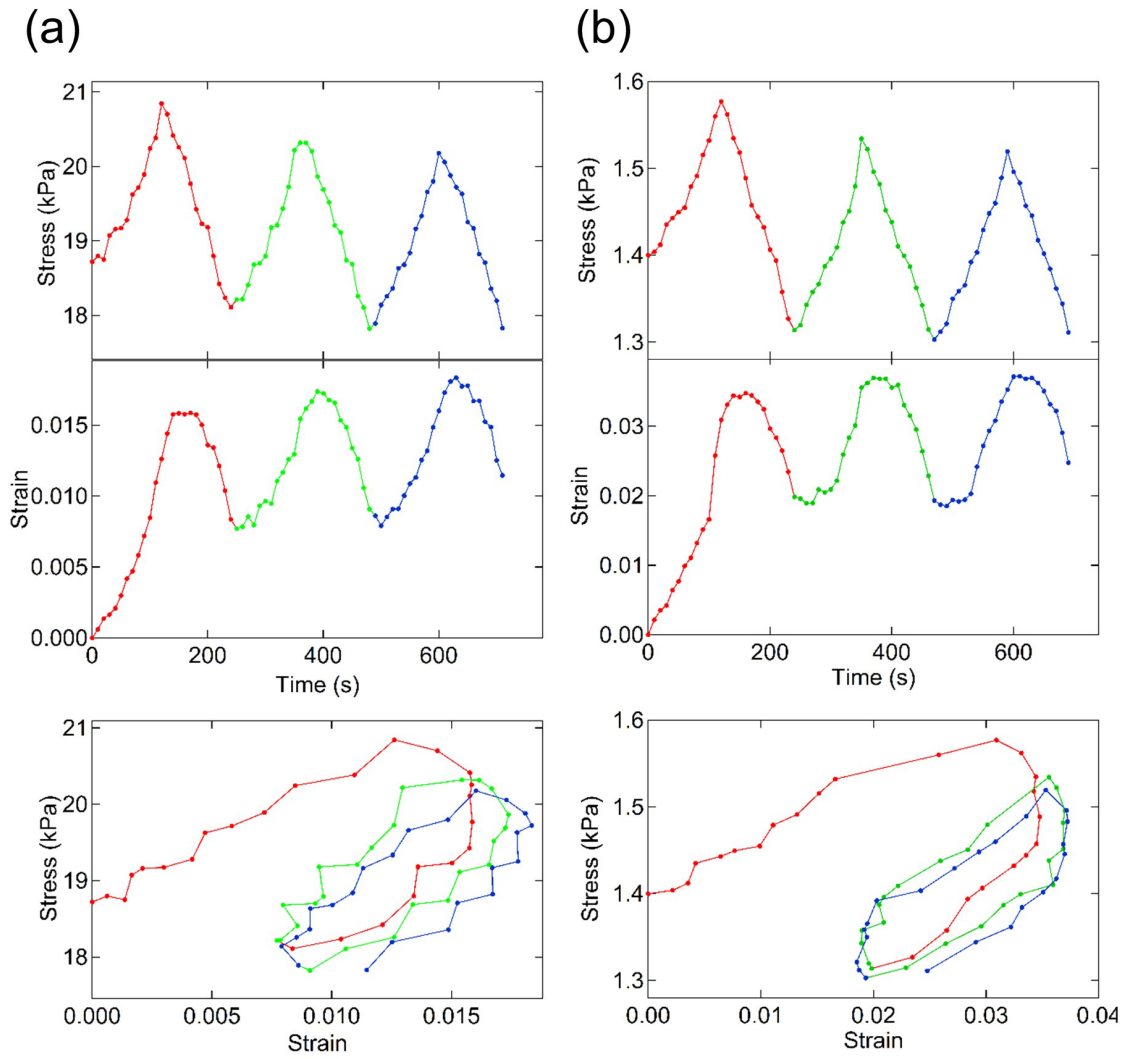

Figure 5.2 Microtissue repeated stress-strain. Two samples which show qualitatively similar responses, with decreasing maximum stress and increasing maximum strain during successive actuations. Color coding helps associate data between vertical panels.

As the microtissues are first actuated, their initial stress-strain behavior matches that of the tissues presented in Chapter 4 (Figure 5.2, red data). Unlike those tissues, however, they were not given the opportunity to recover to their initial states in the stress-strain phase space. Immediately after the first actuation, they were actuated again. This repeated, non-stop actuation causes the microtissues' equilibrium length to increase by 1-

3%, which can be seen by the shifts in the strain minimums corresponding to the second and third actuation (Figure 5.2, strain). The stiffness of the microtissues can be found by fitting the initial linear portion of the stress-strain curves for each successive stretch, corresponding to periods where applied force was steadily increased. Notably, the modulus associated with the second and third stretch was much higher than that of the modulus associated with the initial stress, indicating that the microtissues show stiffening behavior. The microtissue modulus approximately doubles between the first and third stretch, with the most dramatic change occurring between the first and second stretch.

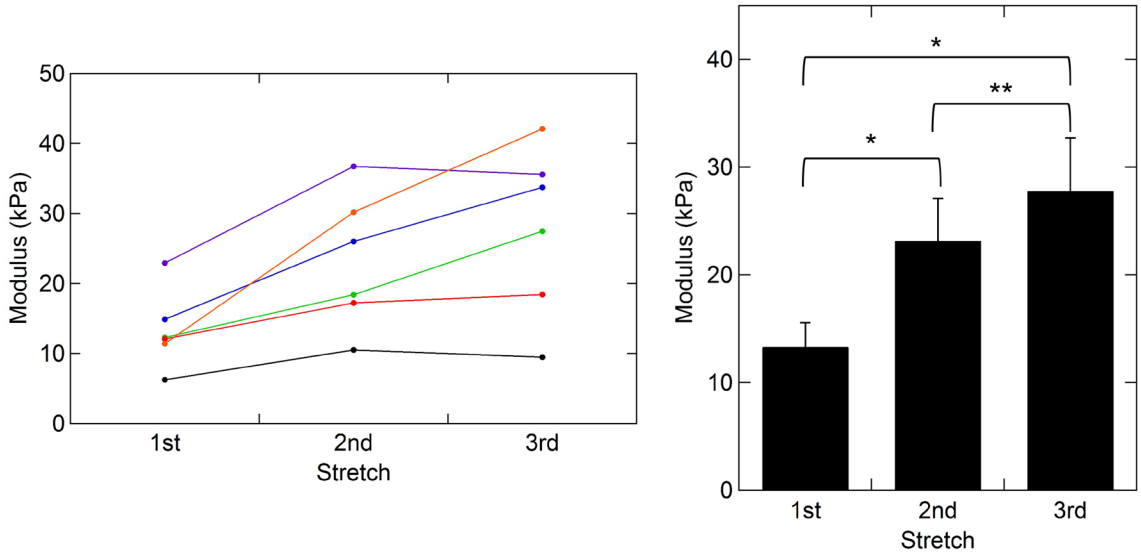

Figure 5.3 Increases in microtissue modulus. (a) Modulus of selected microtissues during successive actuations. (b) Average modulus of microtissues during the three stretches, showing greatest change between 1st and 2nd stretch. * $p<0.01$, **$p>0.05$, n=6.

Treatment with Triton X-100 and trypsin

Similar to the single pulse experiments described earlier, these microtissues were also treated with Triton X-100 in order to ascertain the matrix-only response to applied force. In this set of experiments, microtissues were also treated with 0.25% trypsin EDTA, a compound that detaches cells from the ECM, in order to corroborate the findings of the Triton X experiments. Detailed steps of trypsin treatment can be found in the Appendix. Unlike the results presented in Chapter 4, the results presented in this chapter are paired (i.e. mechanical measurements were made on a microtissue, it was treated with either Triton or trypsin, and mechanical measurements were again made on the same tissue).

Figures 5.4-5.7 below show the representative response of untreated microtissues adjacent to the same microtissue following Triton or trypsin treatment to three successive triangle wave actuations. Data is presented in order of stress vs. time, strain vs. time, and stress vs. strain, and this pattern will be maintained for the remainder of this section.

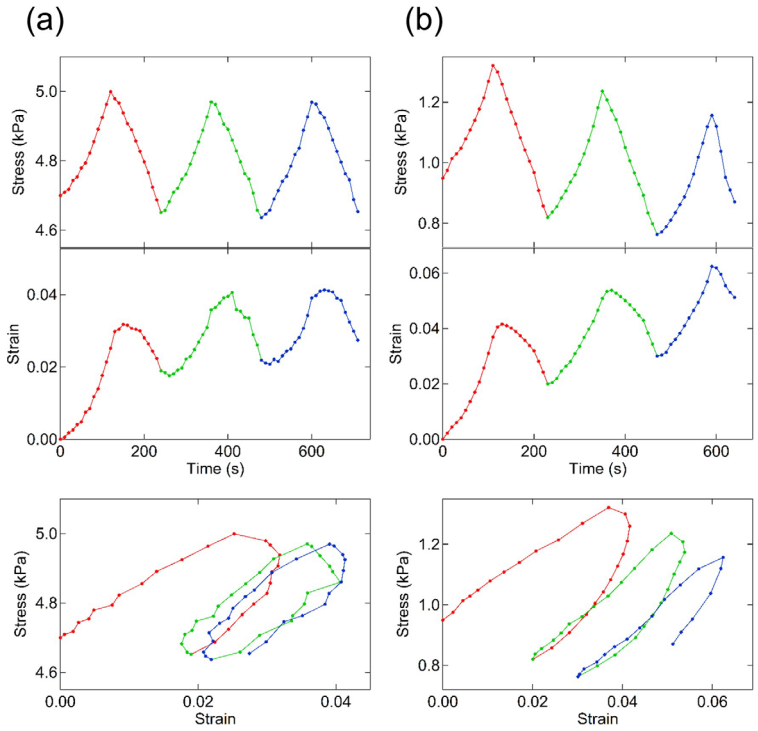

Figure 5.4 Triton treatment. (a) Untreated control. (b) Treated with Triton.

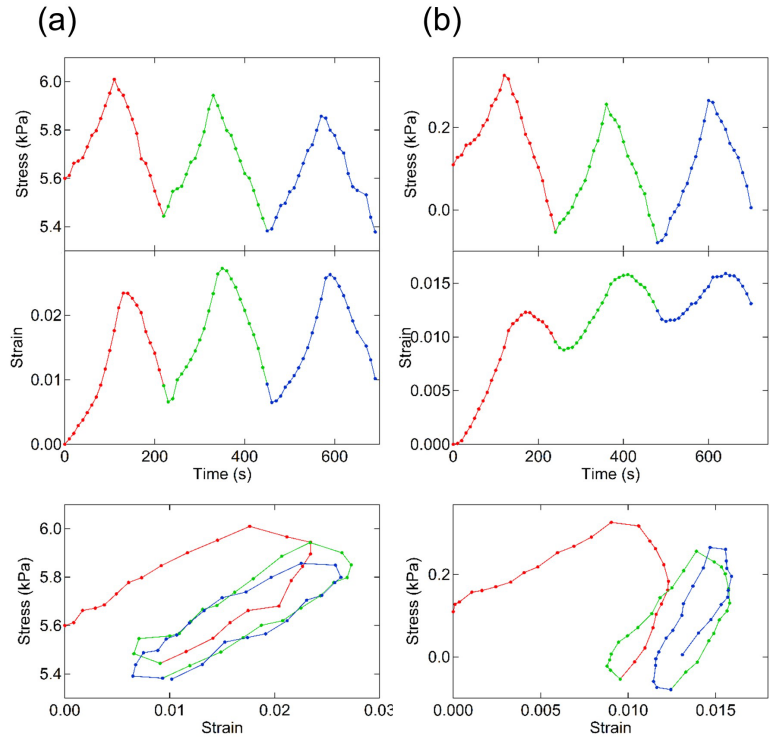

Figure 5.5 Triton treatment. (a) Untreated control. (b) Treated with Triton.

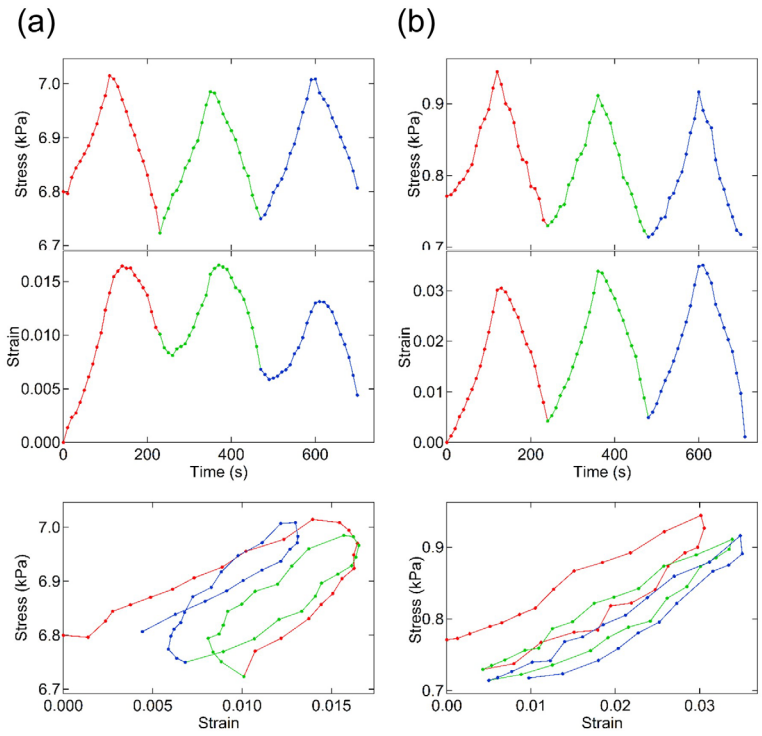

Figure 5.6 Trypsin treatment. (a) Untreated control. (b) Treated with trypsin.

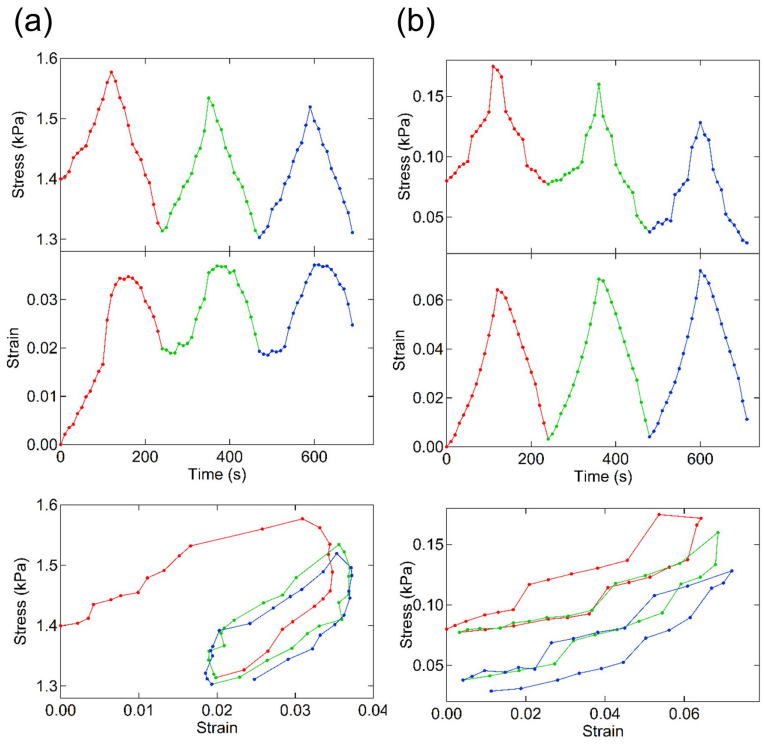

Figure 5.7 Trypsin treatment. (a) Untreated control. (b) Treated with trypsin.

The behavior of Triton and trypsin treated microtissues was qualitatively similar. Compared with their untreated counterparts, these microtissues showed dramatic decreases in their pre-stretch, initial stress (which can be seen in the initial stress in Figures 5.4-5.7 above) as well as decreases of around 50% in their stiffness as they are first actuated (Figure 5.8)

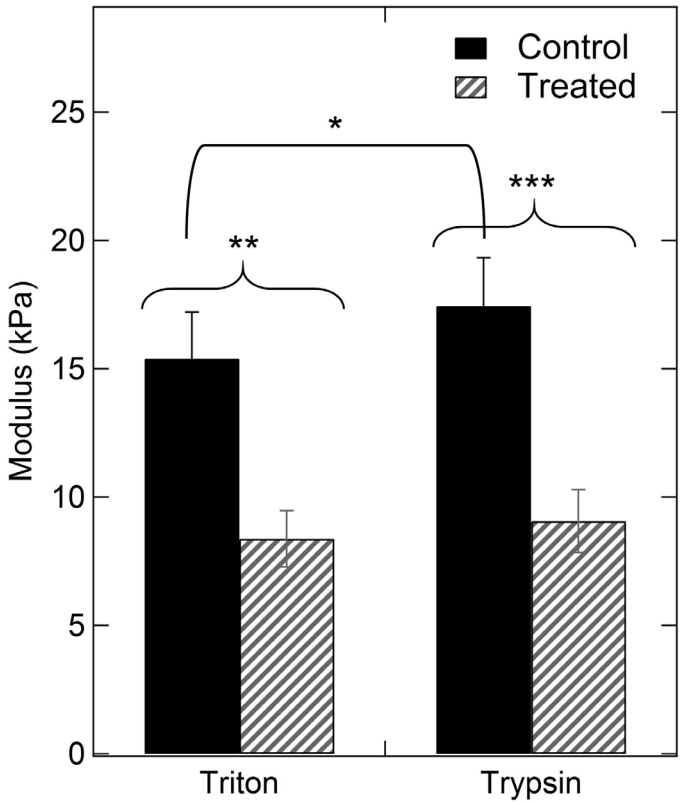

Figure 5.8 Modulus changes in microtissues, initial stretch, paired. Treating microtissues with either Triton or trypsin decrease their initial modulus by ~50%. * p=0.24, ** p<0.01, *** p <0.04, n=4, for each

The peaks in stress response matched peaks in the applied force for both untreated and treated microtissues (Figures 5.4-5.7). In the strain vs. time panels of these figures, there is a notable difference in the strain response between untreated and treated tissues. The peaks and valleys in the strain of untreated tissues lags the corresponding peaks and valleys in the stress. Contrastingly, for treated tissues, peaks and valleys in stress and strain are much more aligned in time; there is very minimal lag in the strain response to changes in stress, a characteristic which can also be seen in the sharp peaks in the strain-time graphs in Figures 5.4-5.7. Tissue stress decreased with increases in tissue strain due to lower applied stress from the micropillars (i.e. the longer the microtissue, the less the micropillars are deflected, and the less stress the micropillars apply to the microtissue).

In the stress-strain figures, although the first loops look qualitatively similar between treated and untreated microtissues, the subsequent loops show very different behavior. In the control condition, the loops sometimes moved left (or roughly maintained their position after the first actuation) along the strain axis, indicating active contractility, while in the Triton/trypsin condition, the loops invariably moved towards the right. This response is another indication of the fundamental difference between untreated and treated tissues. BPA-SMCs within untreated tissues stiffen through the contractile action of the cellular force generation machinery as a result of the application of external force while the Triton and trypsin treated tissues plastically deform.

The modulus associated with each stress-strain loop for Triton/trypsin treated microtissues was measured as well, and notably, there was no statistical difference in their stiffnesses during the first loop and the last loop, in contrast to untreated

microtissues, where a 2-fold increase was seen in their modulus between the first and last actuation. ("Successive" data, Figure 5.9).

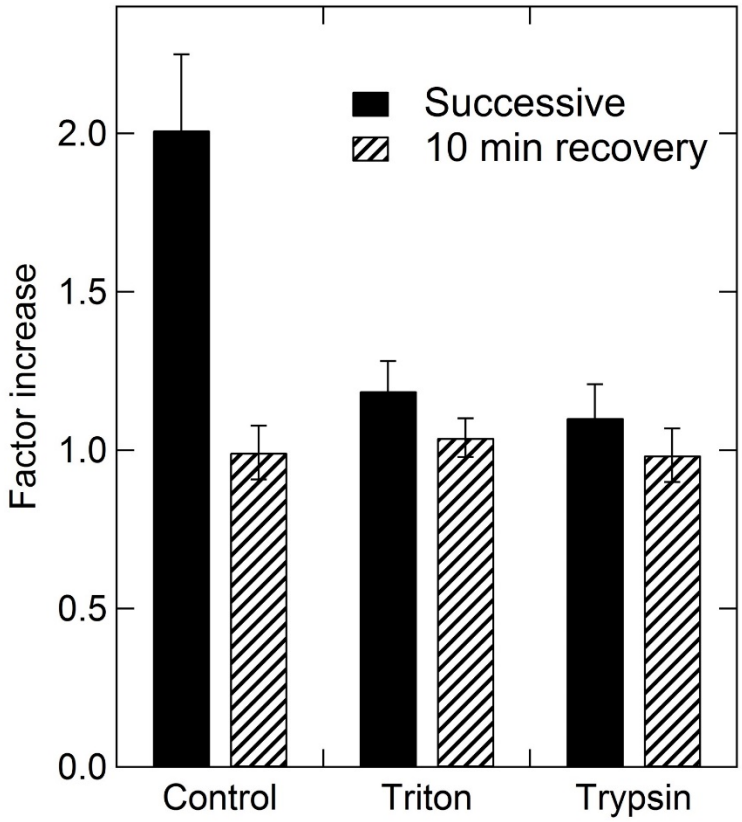

Figure 5.9 Changes in modulus. Factor increases between 1st and 3rd moduli for microtissues actuated successively and 1st and 2nd moduli for microtissues which were allowed to recover for 10 minutes.

5.2.2 Effect of recovery period

In order to investigate the mechanical recovery of these microtissues and the effect of this mechanical recovery on subsequent actuations, untreated, Triton-treated, and trypsin-treated microtissues were subjected to the force profile seen in Figure 5.10 below. The unit triangle wave pulse described previously was applied to the microtissues, they were allowed to recover for 10 minutes, and then they were subjected to the triangle wave pulse again.

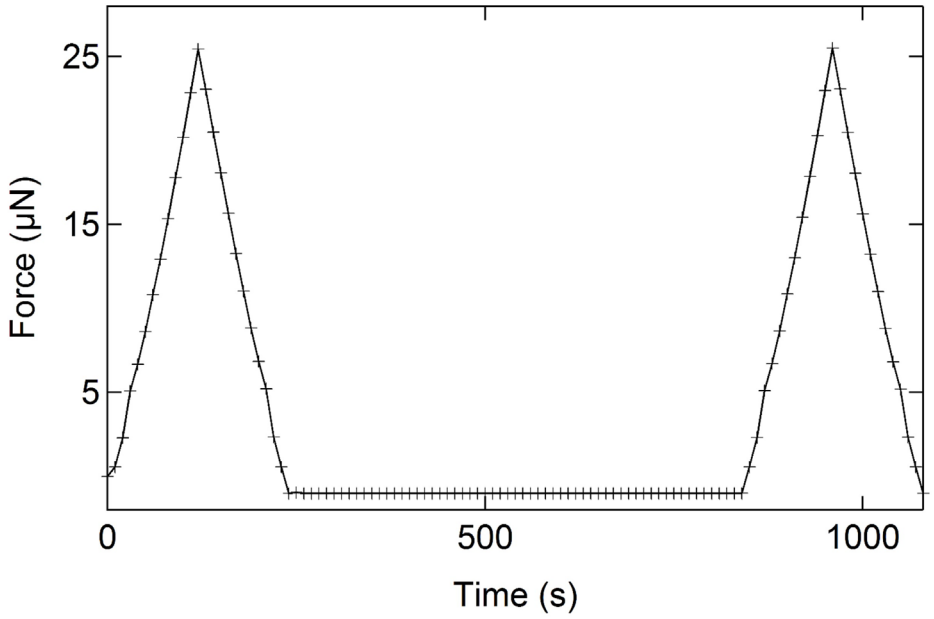

Figure 5.10 Force vs. time with 10 minute recovery period. Two triangle wave force inputs separated by a 10 minute interval were applied to the microtissues.

Analogously to the protocol presented in §5.2, microtissues were actuated with a force profile, treated with either Triton or trypsin, and then actuated again immediately afterwards. Representative stress and strain responses of these tissues are shown in Figures 5.11-5.14 below.

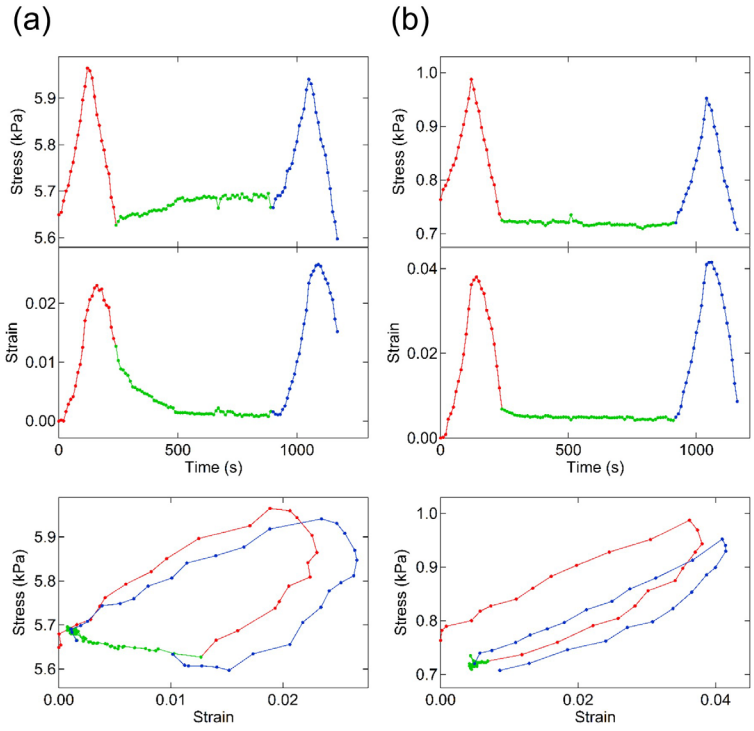

Figure 5.11 Triton treatment. (a) Untreated control. (b) Treated with Triton.

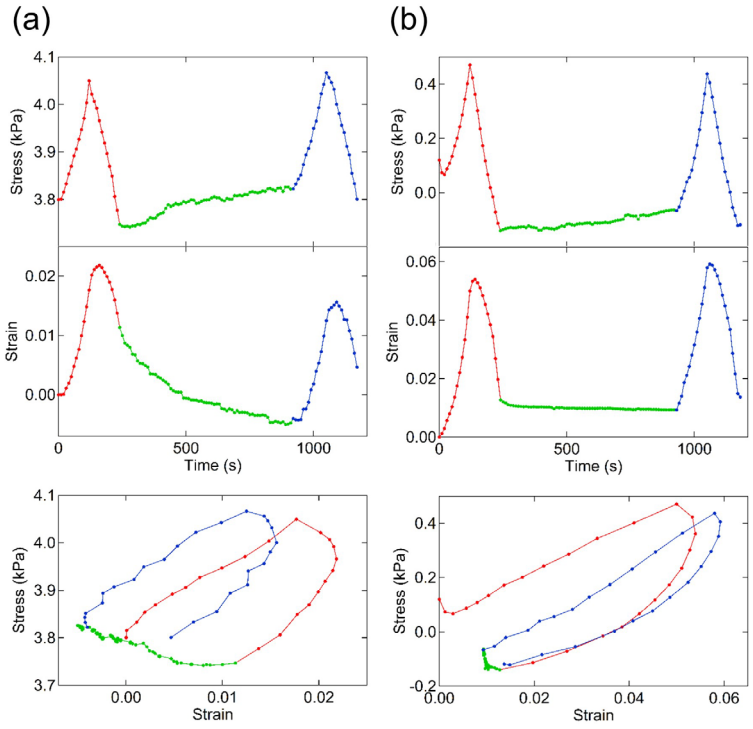

Figure 5.12 Triton treatment. (a) Untreated control. (b) Treated with Triton.

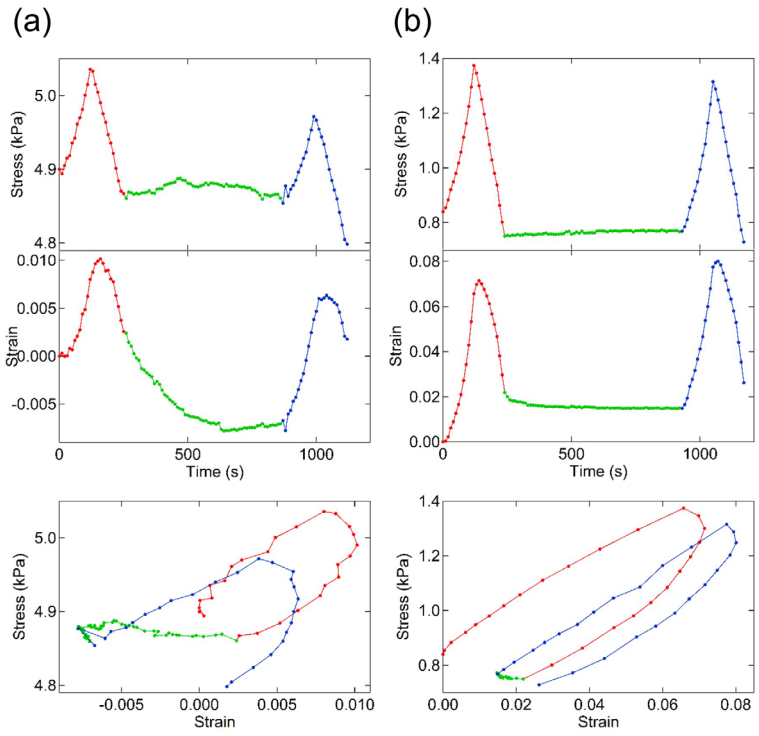

Figure 5.13 Trypsin treatment. (a) Untreated control. (b) Treated with trypsin.

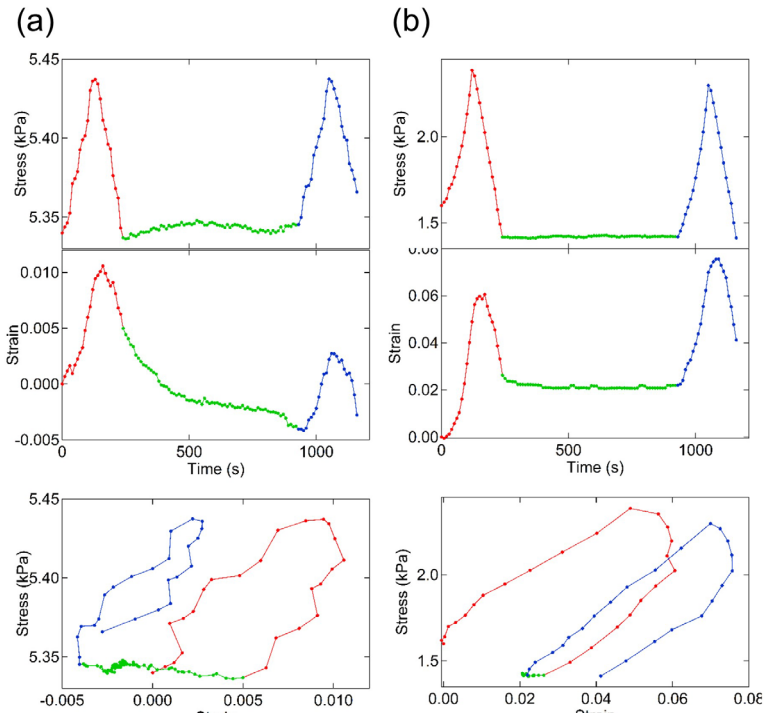

Figure 5.14 Trypsin treatment. (a) Untreated control. (b) Treated with trypsin.

The characteristics of the microtissues' stress-strain response to this force profile are similar to those observed from the three pulse actuation. Again, for untreated tissues, stress changes tracked with changes in applied force, and strain changes lagged the stress changes. This lag, the broad peaks in strain, and the long recovery tail seen from ~200-500s in the strain vs. time panels of Figure 5.11a-5.14a highlight the viscoelasticity of the microtissues. This tail can be attributed to the active force generation of the cells and was also observed in Chapter 4 previously.

Similarly, the qualitative mechanical response of Triton/trypsin treated tissues actuated with this two pulse signal mirrored that of treated tissues actuated with the three pulse signal. Stress and strain response were aligned more closely in time, and stress-strain loops moved progressively towards the right. These microtissues lengthened after the application of the first stretch and showed a concordant decrease in baseline stress.

The ten minute recovery period between the two actuations helps highlight the differences between untreated and Triton/trypsin treated tissues. In the former, tissue length recovered to its initial, zero-strain condition. Tissue stresses increased at the cessation of the initial force stimulus to either initial values or beyond. The stress-strain loops associated with the second actuation qualitatively mirrored those associated with the first actuation. Quantitatively, the tissues' measured stiffness remained constant between the first and second instances of increase in applied force. In treated tissues, there was no active restoration to initial stress and strain states during the ten minute recovery period. Instead, microtissues remained deformed. The moduli associated with the first and second actuations of these microtissues were also similar.

5.2.3 Discussion

BPA-SMC microtissues were subjected to two types of repeated actuations: successive and time separated quasistatic triangle wave pulses with a period of 240 s and an amplitude of ~25 μN. Comparing the response to repeated quasistatic mechanical stimulus of untreated and treated microtissues to the response of these tissues subjected to a single stimulus (as presented in the previous Chapter) serves to reinforce the idea that the bulk of the microtissues' mechanical properties can be attributed to the active contraction of the cells. Removing the cell contribution to the microtissues' mechanical structure, whether through lysing with Triton or detachment with trypsin, dramatically changed the mechanical response of the microtissues.

Untreated microtissues

Microtissues subjected to successive triangle wave pulse actuations showed dramatic changes in their mechanical characteristics as they were repeatedly stretched. In some samples (Figures 5.4a, 5.5a, 5.7a) overall microtissue stress decreased from the first pulse to subsequent pulses, akin to the response seen in the repeated stretching of collagen gels populated with chicken embryo fibroblasts [23]. In other samples (Figure 5.6a) however, stress increased. Although this disparate response has not yet been reported for engineered vascular smooth muscle microtissues, insight into this bimodal behavior can be drawn from stretching studies performed on single vascular smooth muscle cells plated on micropost substrates. In these studies, cell force either relaxed or reinforced up to 20% of original force following the cessation of an applied stretch [9,

40]. Microtissue stress changes (< 10%) were not quite this large, most likely due to averaging across hundreds of cells.

The overall strain of the microtissues increased slightly over the successive stretches, indicating a minor plasticity. This behavior can be explained by the results presented in Chapter 4—the plastic properties of the ECM are mostly masked by the cells.

Plotting stress versus strain allowed for the easier comparison of the evolution of mechanical response over time and makes apparent the increase in modulus between the first and subsequent actuations. This behavior is reminiscent of the differences between the first and subsequent stretches of fibroblast populated collagen gels and may be explained by the reinforcement of active cellular contractility after the first loading cycle [24].

The inclusion of a ten minute recovery period in between successive stretches allowed for the observation of stress recovery following an applied stretch. Previous investigations into the response of single airway smooth muscle cells showed traction force increases following the cessation of the application of an inhomogeneous mechanical force [10]. This result may help explain the response of the microtissues. As the microtissues are uniaxially stretched, embedded cells experience global as well as local inhomogeneity in force. On a global scale, cells are subjected to relatively larger forces along the stretch direction and relatively smaller forces in the direction normal to stretch (due to gel compaction in this direction). On a subcellular scale, cells may also experience inhomogeneity in force due to non-uniform distribution of focal adhesion sites which transduce ECM forces to the cell.

The recovery period also helps set the time scale for cellular and tissue reorganization following the initial force stimulus. From the data, microtissues return to their initial stress-strain states during this ten minute recovery, possibly due to actin remodeling. Studies on the effects of Cytochalasin D, a compound which disrupts actin polymerization, on both actin polymer and airway smooth muscle microtissues have shown that its effects manifest within ten minutes [34, 79]. The similarity in time scales between BPA-SMC microtissue recovery and a compound which disrupts actin polymerization may indicate that microtissue recovery is dependent upon the reorganization of the internal actin-myosin force generation machinery.

Treated microtissues

The response of Triton/trypsin treated microtissues reinforces the conclusions drawn from the mathematical model and numerical fitting presented in Chapter 4. When cells do not contribute to the mechanical properties of the microtissues, microtissue mechanical properties mimic that of a pure collagen gel. Stress-strain loops from successive loadings show sometimes dramatic cyclic creep previously seen in studies of pure collagen gels [80-82]. Notably, however, these loops show none of the strain-hardening effect seen in pure collagen gels, most likely due to the quasistatic nature of the actuation [80].

The stress-strain behavior associated with the force profiles that include a ten minute recovery highlights the plastic deformation the microtissues experience due to the initial stretch. More importantly, however, their shape, when compared to the stress-strain loops of untreated microtissues, are more reminiscent of an elastic-plastic

unloading response—treated microtissues are much more plastic and much less viscous than their untreated counterparts [83]. This assertion is corroborated by the values of the viscosity fit parameters presented in Chapter 4. The viscosity associated with the ECM can be some two orders of magnitude lower than that associated with the cells (i.e. with the untreated microtissue).

5.3 AC stimulation at physiological frequencies

The 1 Hz frequency regime is fundamentally important to the cardiovascular system and, when applied to the microtissues, results in strain rates an order of magnitude higher than those presented in §5.2. The response of the microtissues may give insight on behavior of the vasculature *in vivo* as it is stretched due to pulsatile blood flow.

In the experiments that follow, a 1 Hz signal created by a signal generator (Stanford Research), coupled with a current source (Kiethley BOP 50-2), was input to the magnetic tweezer apparatus. The amplitude of this signal was adjusted manually, starting at 0 mA and slowly ramping to up to 800 mA. The maximum current was set when it could be visually confirmed that the microtissue was undergoing periodic strain at a level that did not risk rupture. Video data at 100 fps was recorded for this initial ramping-up segment as well for a minute following the determination of maximum amplitude. After 5 minutes of actuation, another minute-long segment was recorded to determine tissue behavior after the cessation of any initial transients.

5.3.1 Results

Five selected microtissues are presented below to represent the range of strains and applied stress involved in this experiment. While the microtissues showed a variety of responses during the initial ramp up (possibly due to the different changes in strain rate caused by the manual tuning of the current), at the 5 minute mark, their stress-strain behavior converged.

Initial ramp up

Microtissue length was defined as the distance between the inner edges of the micropillars, and this distance was tracked using the edge detection scheme presented in §2.5.2. Two lengths can be associated with the microtissue as the AC drive is applied: a baseline length when applied force is at its minimum (green squares in Figure 5.15) and a maximum length (red squares in Figure 5.15). As seen in the representative figure below, both baseline and maximum length steadily increased during the ramp up in applied force (ending at ~45s). After maximum force was reached, these lengths quickly reached a new equilibrium within a few periods.

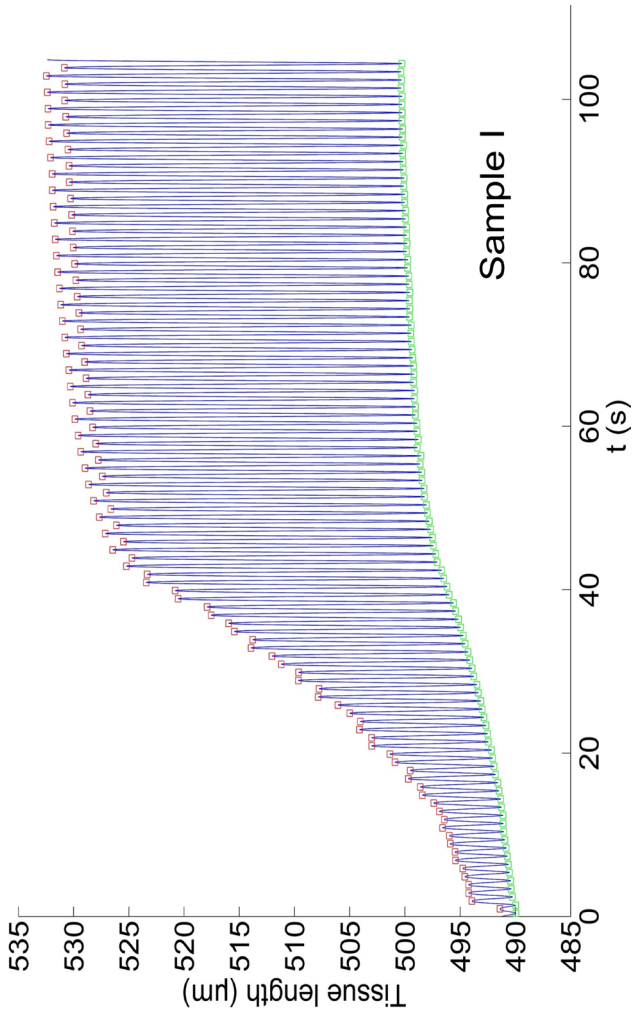

Figure 5.15 Length of microtissue vs. time. Ramp up in current can be seen between 0-~45 seconds. Tissue length stops changing shortly after maximum current is set. Maximum and minimum lengths are labeled with red and green squares, respectively. Variation in maximum tissue length can be attributed to magnetic artifacts.

Strain and stress, variables which characterized the mechanical response of microtissues subjected to quasistatic force inputs were, in this case, tracked continuously. Strain was defined as the microtissue length relative to the trailing minimum length, and stress was defined as increases in stress relative to the trailing stress minimum. Maximum strains reached 1-7% across all microtissues, and maximum applied stress ranged from 100-500 Pa.

Stress is plotted against strain in Figure 5.16. A range of applied stress and strains were chosen in these examples: from low stress and low strain (Figure 5.16b) to high stress and high strain (Figure 5.16e) The stress-strain loops of each microtissue converged as the amplitude of force input steadies and the space between the 'upstroke' and 'downstroke' of the loops highlights the viscoelastic behavior of the microtissues at the 1 Hz forcing frequency. The colorbar associates the data with the period: blue indicates data near the beginning of the measurement, and red indicates data taken near the end. These stress-strain loops travel in a clockwise direction, and this behavior is denoted by the blue arrows in Figure 5.16a.

The stiffness of each tissue was also found by fitting each 'upstroke' with a linear function. The average moduli of these 5 tissues was 9 ± 4 kPa.

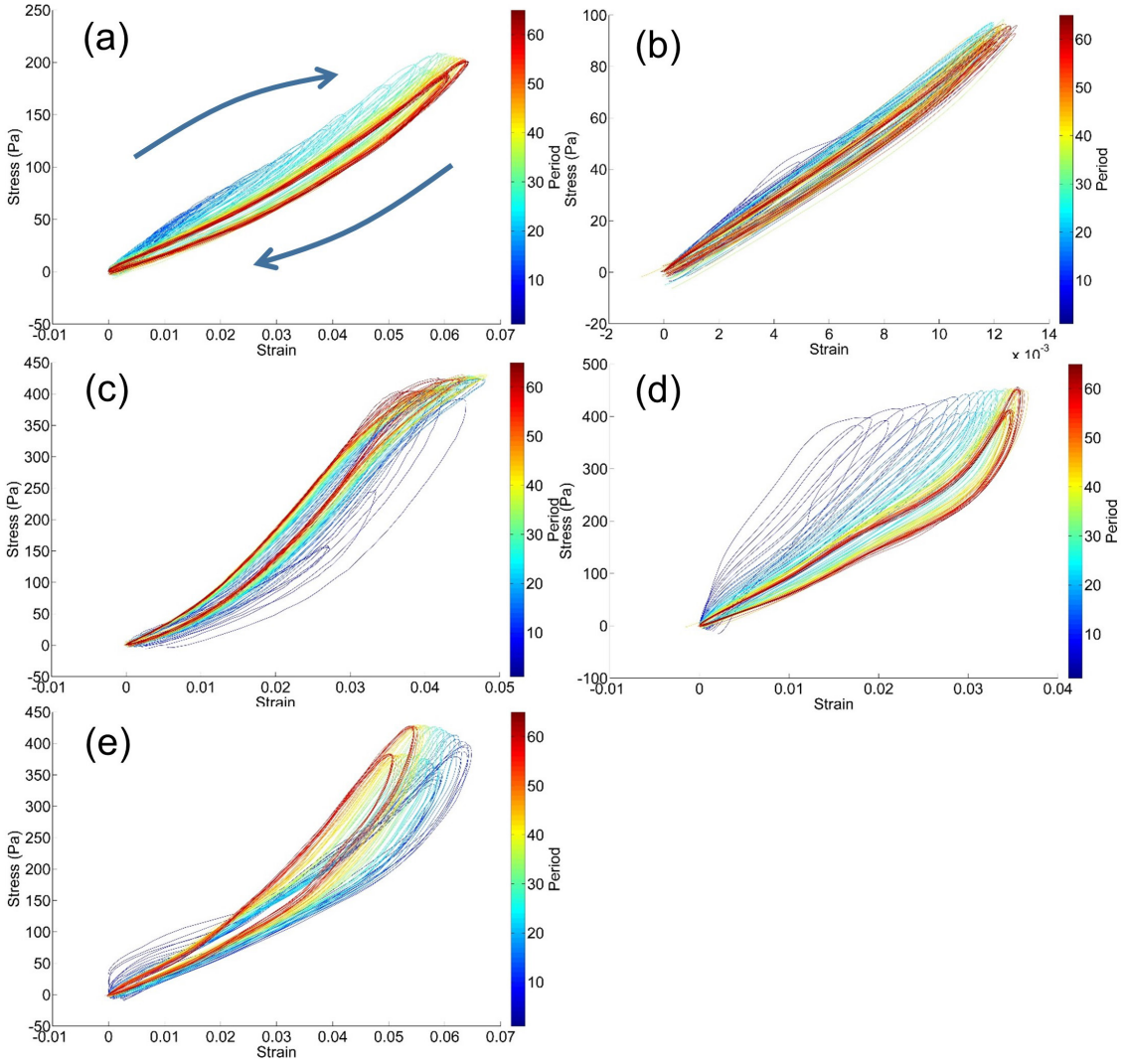

Figure 5.16 Initial cyclic stress strain. Stress-strain loops show transient behavior (blue curves) due to initial increases in current. After maximum current was established, changes in the stress-strain behavior diminished (red curves).

Steady state behavior at 5 minutes

For these microtissues, baseline strain, defined as the minimum length of the microtissue during actuation relative to the length of the microtissue before actuation, stabilized at ~2% strain. Figure 5.17 is the Figure 5.15 analog for the segment at 5 minutes, and it shows that baseline microtissue length remains constant. Figure 5.18 below shows that baseline strain only varies up to ~0.03% over the observation period, and these variations can be attributed to measurement uncertainty. Baseline microtissue length remains constant during the application of cyclic strain.

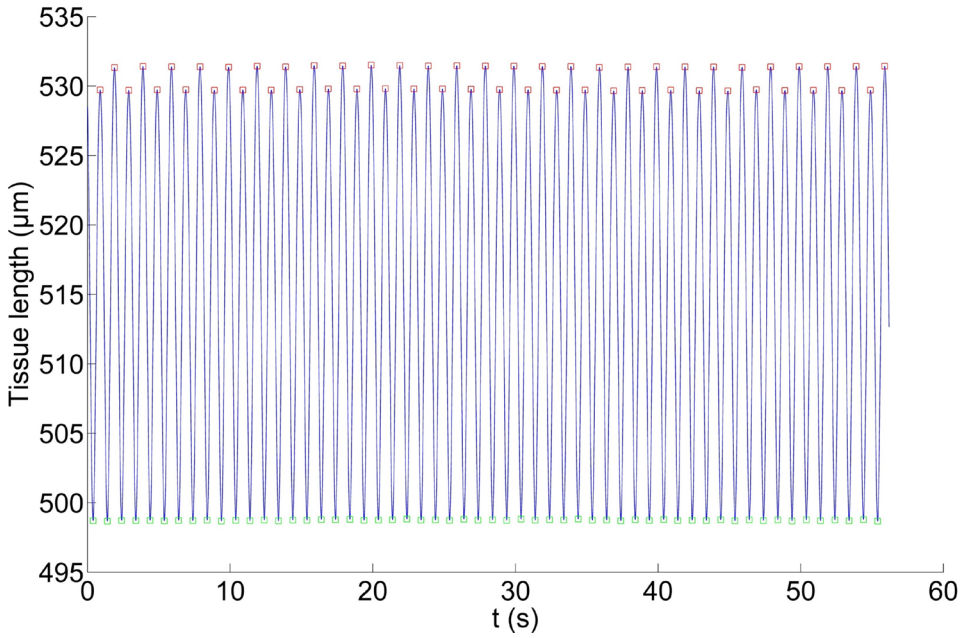

Figure 5.17 Microtissue length. Microtissue minimum (green squares) and maximum (red squares) length reach new equilibrium after 5 minutes of cyclic strain.

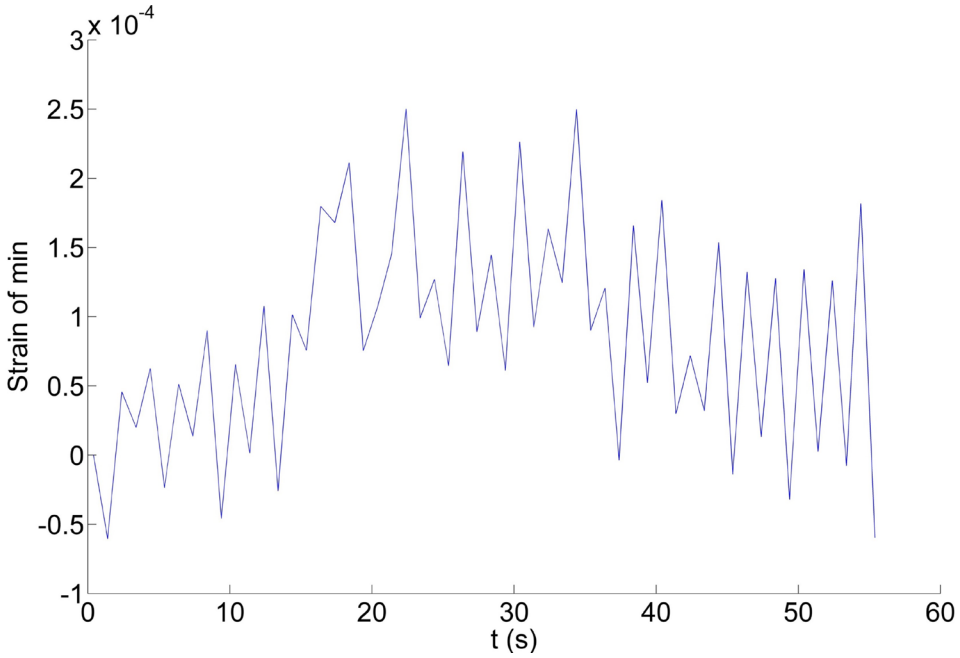

Figure 5.18 Variation in microtissue length. Minimum microtissue length (green squares in Figure 5.19) varies by at most 0.03% over the 1 minute observation period after 5 minutes of cyclic strain

Stress was again plotted against strain for data recorded after 5 minutes of cyclic actuation for the same tissues shown in the previous section (Figure 5.19). At 5 minutes, microtissue stress-strain behavior had reached a steady state. Some of the more dramatic non-linear behavior seen in Figure 5.18c-e now relaxes to a slight strain stiffening. Qualitatively, although these stress-strain loops are similar, the higher the maximum strain (and thus the higher the strain rate), the more strain stiffening was observed. Little changes in stress-strain behavior occurred during this minute-long observation as seen in the intermixing of colors in the stress-strain loops. The stiffness associated with these microtissues was also measured, and the average stiffness was 10 ± 4 kPa.

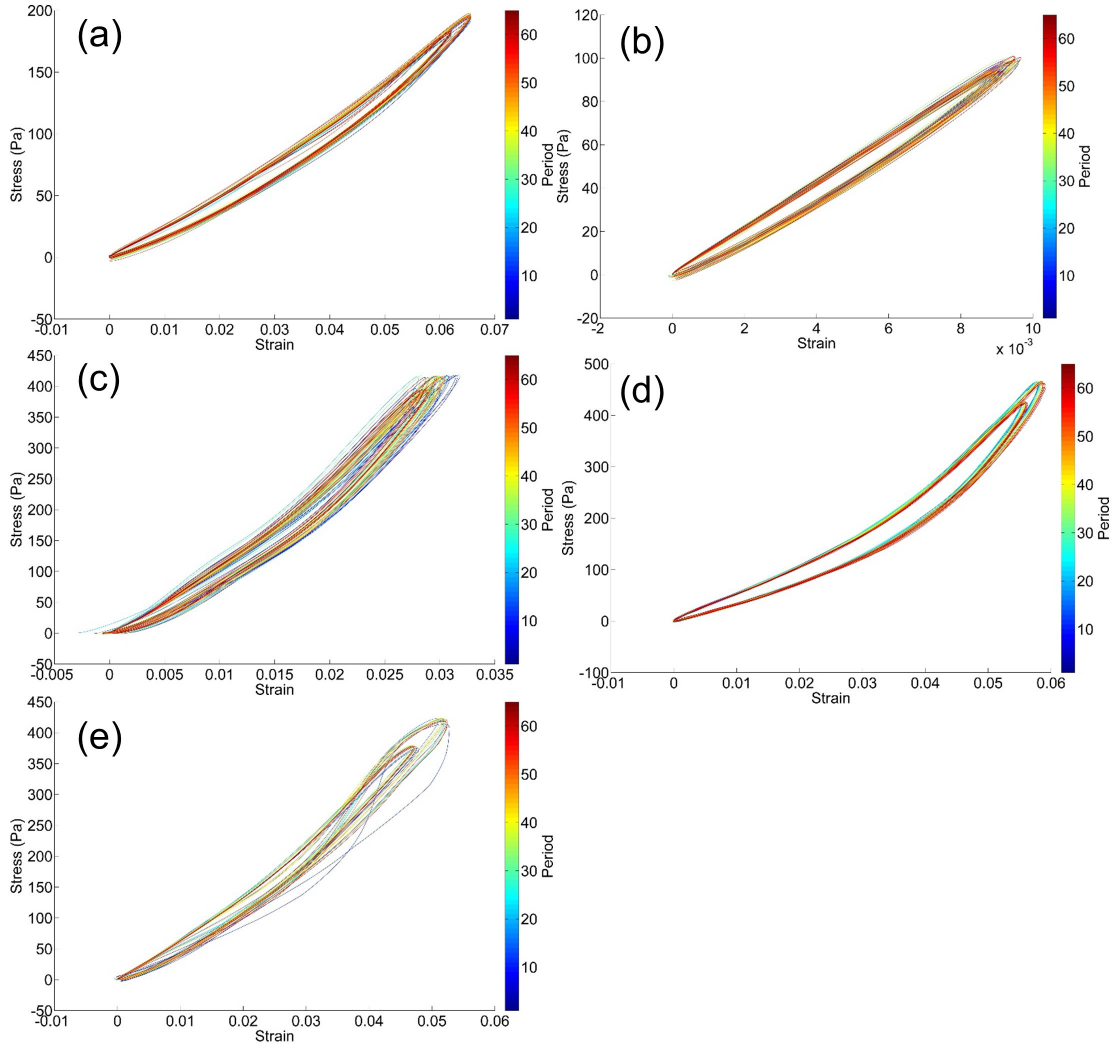

Figure 5.19 Microtissue stress strain at 5 minutes. The stress-strain behavior of these microtissues is qualitatively similar, regardless of their different initial transient behavior seen in Figure 5.18. Tissues that reached higher maximum strains (d) demonstrated more non-linear behavior than tissues that reached lower maximum strains (b).

5.3.2 Discussion

A 1 Hz cyclic strain of up to ~ 7% was applied to BPA-SMC microtissues. These strains (and thus strain rates) are similar to those seen in human *in vivo* pulmonary arteries [84-86]. Two responses were observed due to the application of this cyclic strain, a linear viscoelastic response and a non-linear viscoelastic response. The viscoelasticity of the microtissues is characterized by a ~15 ± 6° phase lag angle calculated by measuring the distance between peak stress and strain responses to cyclic stretch. This value for the phase angle is similar to the ~ 10° phase angle measured from fibroblast populated collagen gels [23].

During the initial increase in applied force, the microtissues lengthened by 1-2% and this new length was generally maintained throughout the course of the experiment. This elongation may be a result of collagen fiber realignment in the strain direction [87] and of a relatively fast cyclic strain rate. It was shown in the previous section that microtissues require a minutes-long relaxation to recover to their original stress and strain states, and a 1 Hz periodic strain does not afford enough time for this relaxation to occur. Notably, the elongation seen in the microtissues as a result of repeated quasistatic stretches is similar to that seen as a result of cyclic stretch, and this similarity in behavior reveals that timescales on the order of ~1 s to ~1 min are equivalent in terms of the microtissue relaxation response.

The microtissues' also exhibit a varied and highly nonlinear stress-strain response to the initial increases in cyclic strain. This behavior is most likely a reflection of the strain-hardening characteristics of the underlying actin network within the SMCs [88] and is associated with the dashpot elements in the mechanical model presented in

Chapter 4. Because strain rates and changes in strain rate were manually and non-uniformly adjusted, cellular stresses, which scale as the strain rate, contribute to dramatically different stress-strain behavior. The tissue stiffness was measured to be 10 ± 4 kPa once the microtissue behavior reached an equilibrium after the cessation of these initial transients.

After five minutes of cyclic stimulation, the microtissues reached an equilibrium behavior, and the stress-strain loops associated with this behavior displayed markedly less strain-stiffening than the loops associated with the initial measurements. This change in behavior happened over a minutes-long time period and, based on this time scale, may indicate that active cellular processes have diminished the strain-stiffening behavior. The loops at five minutes were reminiscent of the non-linear strain-stiffening seen in *ex vivo* arteries as well as pure collagen gels. [80, 89]. There was, however, a major difference seen in the behavior of the microtissues. The onset of the strain stiffening occurs at much lower strains than either of these two materials, although this effect may be a consequence of the higher strain rate applied to the microtissues. Strain stiffening does not occur at low maximum strains (as seen in Figure 5.19b) and suggests that strain-stiffening behavior may be a function of the strain rate. Rheological-type experiments performed on the microtissues would help elucidate this effect. Furthermore, although the matrix-only contribution to this strain-stiffening behavior can be theoretically captured by lysing the cells with Triton, the μTUG substrate, unfortunately, is an unsuitable vehicle to perform these experiments. Collagen gels begin to show strain stiffening at strains greater than ~10% [80], but microtissues built on the μTUG substrate become mechanically unstable beginning at around 8% strain.

The differing responses between these samples demonstrates the high variability seen in mechanical measurements of biological systems. However, the general shape of the microtissues' stress-strain response seems to be converging as cyclic stretch progresses, suggesting the homogenizing effects of mechanical conditioning [20]. Systems which can practically impart a cyclic strain to the microtissues over a longer period of time will be useful in examining how microtissue mechanical properties evolve and will be the subject of the next chapter.

Chapter 6 Fabrication of high throughput microtissue stimulation device

6.1 Introduction

Although the μTUG system has demonstrated its ability as a high throughput method to measure the contractility and stiffness of the microtissues, the dynamic stretching experiments reported in previous chapters were carried out successively on individual microtissues with magnetic tweezers. The capabilities of this system would clearly be enhanced by the ability to apply external forces to multiple microtissues simultaneously and to carry out external force application over extended periods of time, neither of which the magnetic tweezer-based approach can easily provide.

This chapter will discuss the design, fabrication, and use of a device we termed a "Lid Array" that can transduce a uniform magnetic field into locally non-uniform gradient fields in multiple locations on a μTUG array, and hence magnetically actuate many microtissues at the same time. 3T3 microtissues were used to validate the effects of

the Lid device [78]. The Lid consists of a through-etched piece of silicon with patterned gold fingers on which bars of nickel are created through template electrodeposition. The through-etched holes in the silicon allow media and optical access to the underlying μTUG, and the nickel bars are responsible for the local transduction of the global magnetic field (Figure 6.1).

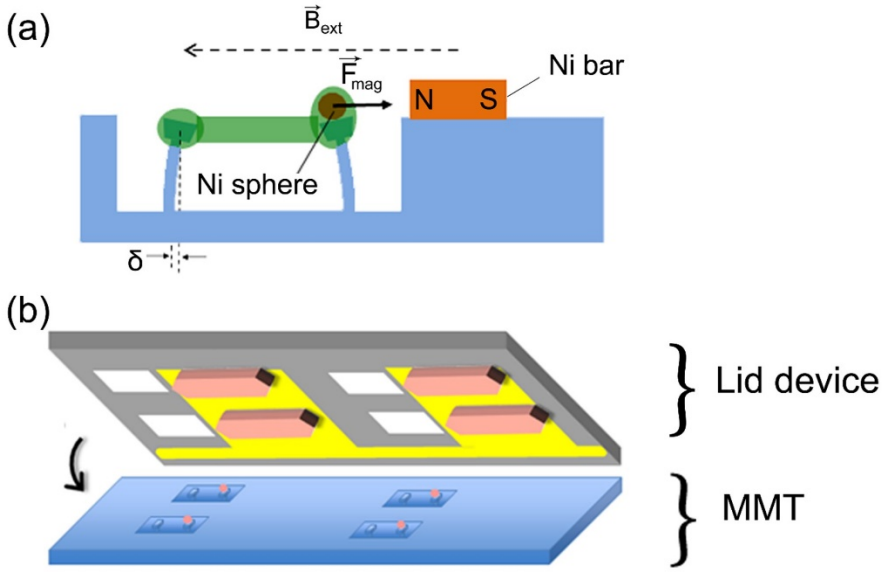

Figure 6.1 Lid device. (a) Demonstration of premise behind Lid device. Uniform magnetic field $\boldsymbol{B}_{ext}$ magnetizes both the nickel microsphere and the nickel bar (tan) and creates a force between the microsphere and the bar, $\boldsymbol{F}_{mag}$. The deflection of the left pillar, δ, reports the tissue's force. (b) Schematic of complete Lid-μTUG system. Silicon wafer contains gold fingers (yellow) that serve as electrodes during the electrodeposition of nickel bars. Through-etching (white) allows optical and media access to underlying microtissues.

6.2 Fabrication and apparatus

6.2.1 Lid fabrication

The fabrication of the Lid device can be broken down into three segments: gold circuitry definition, nickel electrodeposition, and wafer through-etching. The component steps in these segments were not completed in order, but instead interwoven in order to ensure survivability of the features on the substrate.

Figure 6.2 shows the overall fabrication process. The substrate of the Lid consists of a double-side polished Si_3N_4 coated silicon wafer. On this wafer, metal circuitry (45 nm Au on top of 7 nm Cr base layer) was created using standard photolithography, thermal evaporation, and lift-off techniques (Figure 6.2a). The shape and location of the metal circuitry was designed to fit in between adjacent microwells of the μTUG with which the Lid will ultimately be used. After metal circuitry creation, a 120 μm SU-8 photoresist was then spun over the metal side of the wafer, and patterns in the desired shape of the nickel bars were defined in this resist layer on the Au circuitry (Figure 6.2b). To ensure clean Au surfaces for the subsequent Ni electrodeposition, the top side of the substrate was RIE etched in O_2 for 5 minutes to remove any remaining SU-8 on the exposed Au regions. A mask for wafer through-etching was then defined on the backside of the wafer. This through-etching pattern consists of an array of 1200 μm x 800 μm rectangles and was translated into a mask through photoresist lift-off to expose the nitride layer and reactive ion etching in CF_4 and O_2 to remove selected parts of the nitride layer (Figure 6.2c).

A potentiostat (Model 263A, Princeton Applied Research) was used in galvanostatic mode and was set to -1 V relative to a platinum reference electrode in order

to electrodeposit the nickel bars into the patterns defined in Figure 6.2b. These bars could be constructed to a thickness of 50-100 μm, as desired, and used the Au circuitry as a working electrode (Figure 6.2d). The nickel deposition solution consisted of 80.5 g nickel (II) sulfamate, 6.25 g nickel chloride, 10 g boric acid, and 0.05 g sodium dodecyl sulfate (SDS), in 250 mL water. By design, nickel bars include tips on both ends in order to accommodate future substrate geometries whereby one nickel bar could actuate two adjacent microtissues. In these experiments, the nickel bar only actuated one microtissue.

Finally, to create through-etched holes which match the dimensions of the wells on the μTUGs, the Si wafers were etched in a 30% w/v KOH solution at 150 °C for approximately 6 hours (Figure 6.2e). The KOH bath had the added effect of removing any remaining photoresist adhered to the wafer.

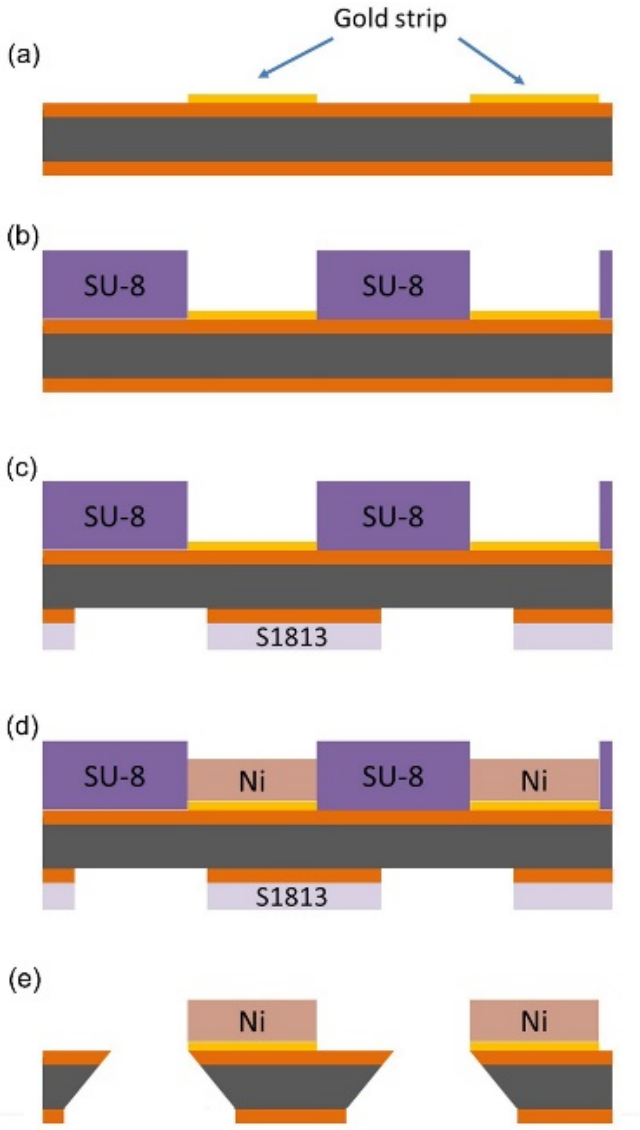

Figure 6.2 Lid fabrication process. (a) Chrome/gold arrays were patterned onto double-side polished Si_3N_4 wafers using standard lithography techniques. The Si is shown in gray and the Si_3N_4 in orange (vertical dimensions not to scale). (b) SU-8 photoresist was patterned to define the shapes of electrodeposited Ni bars. (c) S1813 photoresist was patterned on the bottom of the wafer using back-side alignment, and the exposed silicon nitride was removed by reactive ion etching in CF_4 to define a mask for wafer through-etching (d) Nickel bars were electrodeposited into the patterns established by the SU-8. (e) The wafer was etched in 30% w/v KOH at 130 °C to create rectangular holes. Any remaining photoresist was removed by the KOH etch.

6.2.2. Magnetic field generation with solenoid coils

For both characterization measurements and probing of microtissues the Lid Arrays were mounted and aligned under a microscope on μTUG devices. The arrays were actuated with a microscope-mounted dual-coil programmable electromagnet capable of producing magnetic fields of up to 50 mT with a uniformity of 3% over the largest arrays studied (Figure 6.3). To benchmark the Lid devices' performance, actuation of individual

microtissues was also carried out using the electromagnetic tweezer device employed in the work described in previous chapters of this thesis.

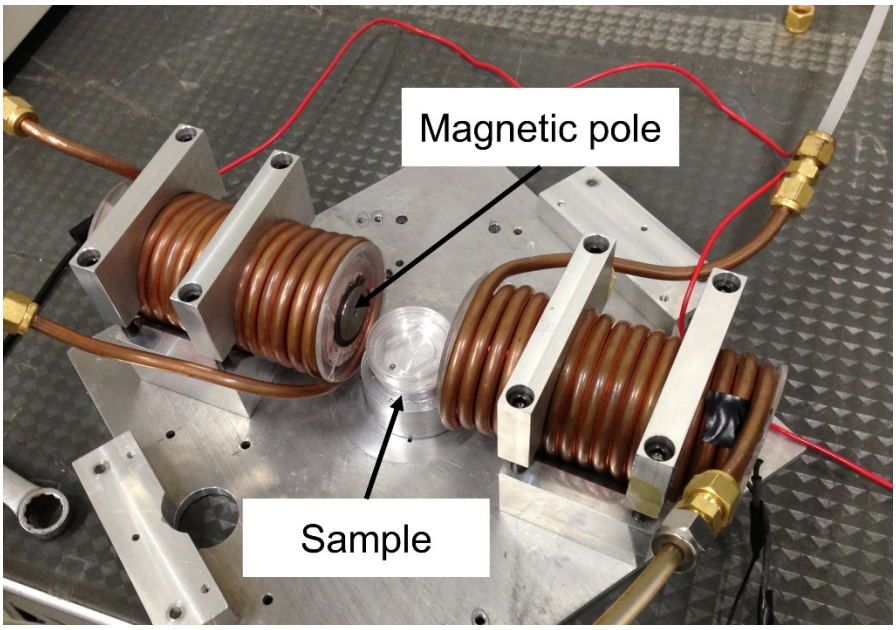

Figure 6.3 Magnetic coils. μTUG sample sits between two magnetic poles. Water cooling coils are visible around the magnetic poles.

6.3 Characterization

The relevant geometric dimensions and magnetic properties of the Lid were characterized. Lateral dimensions were verified by optical microscopy. The thickness of the Ni bars were measured by optical profilometry (VK-VX100, Keyence). The magnetic properties of the Ni bars were determined by removing individual Ni bars from the Si wafers and measuring them in a vibrating sample magnetometer (VSM) (DMS Model 10, ADE Technologies, Westwood, MA). Finite element modeling was also used to determine the characteristics of the magnetic field around individual nickel bars.

6.3.1 Geometric characterization

Arrays of up to 20 nickel bars and corresponding through-holes were fabricated. The nickel bars had maximum overall dimensions of 1.6 mm by 450 µm. The central rectangular region had a length of 775 µm, and the tip width was 90 µm (Figure 6.3). The Ni bars were fabricated with pointed ends to concentrate magnetic flux and create larger field gradients near the magnetic pillars. Nickel bars were arrayed in a rectangular grid with center-to-center spacing of 3.2 mm along the bars' long axis and 1.2 mm along the short axis, corresponding to the spacing of the microwells in the underlying µTUG substrate. Overall lateral dimensions of the nickel bars varied by < 0.6% along the long axis and < 2% along the short axis. The through-etched holes in the Si wafers showed a 5% variability in their dimensions. However these dimensions are not critical as the holes merely needed to be larger than the underlying µTUG microwells to allow optical access through the Si wafer.

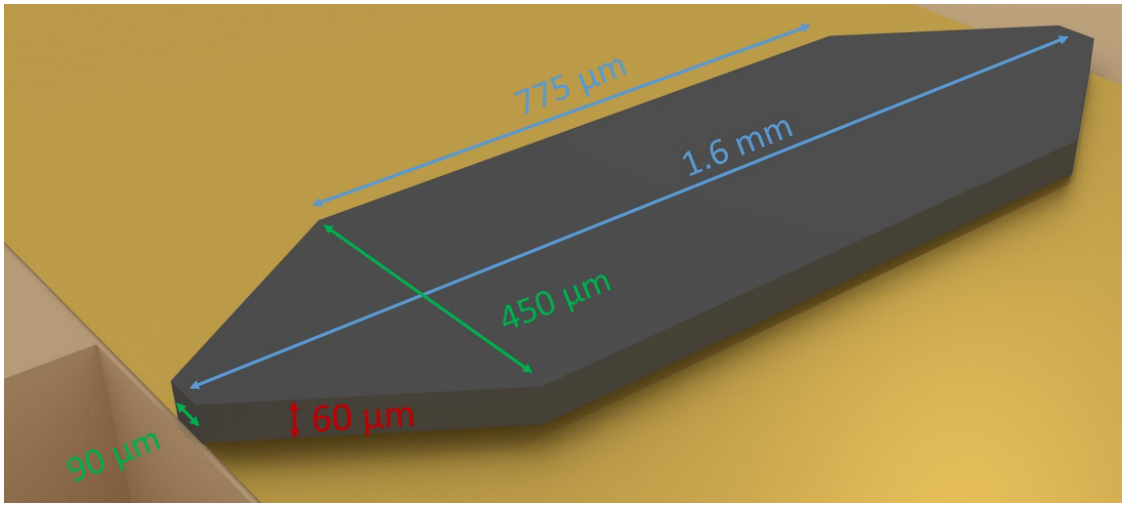

Figure 6.4 Nickel bar dimensions. Digital representation of single nickel bar. Relevant dimensions are shown.

The height of the nickel bars was characterized with optical profilometery. There was an approximately 10% variation in the bars' thicknesses, t=60 ± 7 μm (N=27), likely due to variations in the deposition current across arrays.

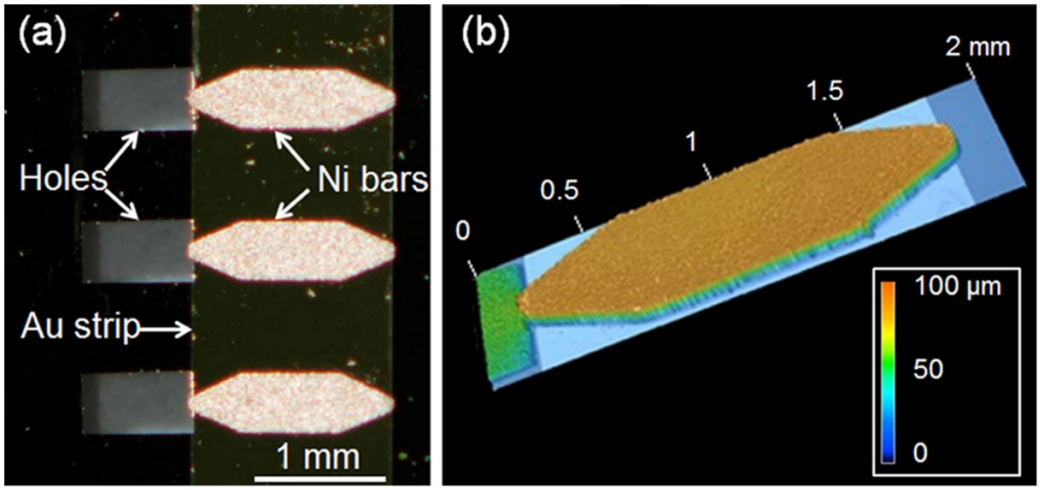

Figure 6.5 Lid geometry. (a) Photograph of a section of a Lid array, showing three Ni bars, their underlying Au strip, and corresponding through-holes. The Ni bars appear bright due to reflected light from the camera flash. The vertical-running edges of the Au strip are clearly seen, and the Si surface appears black. The holes appear gray due to the background below the wafer. (b) Height profile of a Ni bar, as indicated by the color scale. The thickness variation across the bar is < ±2 μm.

6.3.2 Magnetic characterization and modeling

Figure 6.6a shows the magnetic moment μ_{Bar} vs. applied magnetic field for a representative Ni bar removed from the array and measured via VSM (data from Ruogang Zhao). As shown in Figure 6.6a, the magnetic hysteresis of the bars is small, with a remanent moment approximately 10% of the bars' saturation moment μ_{Sat}. Note that the measured value of μ_{Sat} = 17.2 μA m^2 agrees very well with that expected for the design dimensions and the room temperature saturation magnetization of Ni [90]. Figures 6.7a and 6.7b show the deflection of a magnetic pillar due to the force produced by the Ni

bar on the Lid in an applied external magnetic field B_{Ext} = 40 mT. To assess the variability of the force generation, we measured a set of μTUGs on an array and found deflections of 17.4 ± 2.5 μm (F_{Mag} = 15.7 ± 2.3 μN) in a field B_{Ext} = 34 mT (N = 9). My fellow graduate student, Prasenjit Bose, carried out a finite-element modeling computation in the vicinity of one end of a Ni bar of the component B_x of the magnetic field parallel to a bar's long axis in an external field of 34 mT, using the COMSOL Multiphysics package. The results of this computation are shown in Figures 6.6b and 6.6c. Hysteresis effects were not included. From this model we may estimate the force on a Ni bead on an adjacent μTUG pillar as $\mathbf{F}_{Mag} = \nabla (\boldsymbol{\mu}_{Sph}(\mathbf{B})\bullet\mathbf{B})$, where μ_{Sph} is the field-dependent magnetic moment of the Ni sphere in the total field $\mathbf{B} = \mathbf{B}_{Ext} + \mathbf{B}_{Bar}$. At a bar-sphere spacing of 150 μm, the calculation shown in Figures 6.6b and 6.6c yields B = 51.1 mT and dB_x/dx = 180 T/m. At this field, the Ni spheres have μ_{Sph} = 0.075 μA m^2 [33], which yields F_{Mag} ~ 14 μN, in reasonably good agreement with our measured value. Varying the bar thickness and tip width in the COMSOL computations by ±10% as per the measurements given in the previous section showed variations in F_{Mag} of ≤15%, again in agreement with the measured variation of F_{Mag}.

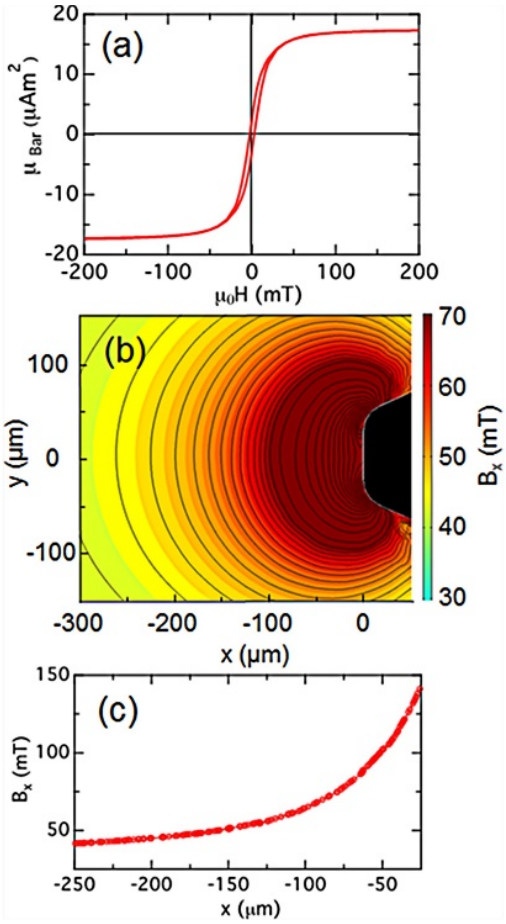

Figure 6.6 Nickel bar magnetic properties. (a) Magnetic moment μ_{Bar} of a Ni bar measured with a VSM. (b) Color contour map of computed field component $\mathbf{B_x}$ near the tip of a Ni bar (shown as black) in an external uniform field $\mathbf{B_{Ext}}$ = 32 mT directed along the x axis. For $\mathbf{B_x} \leq 65$ mT, the black contour lines have spacing 2 mT; for $\mathbf{B_x} \geq 65$ mT the spacing is 10 mT. (c) B_x vs x along the line y=0 in (b). [Data courtesy Ruogang Zhao]

To determine the suitability of the device for AC stimulation, we measured the response of the magnetic pillars to sinusoidal external fields. An example of a magnetic pillar's motion in response to a 0.5 Hz AC magnetic field of amplitude 20 mT is shown in the inset to Figure 6.7c. Since $\mathbf{F}_{Mag}=\nabla(\boldsymbol{\mu}_{Sph}(\mathbf{B})\bullet\mathbf{B})$, the force and displacement are approximately quadratic in $\mathbf{B_{Ext}}$, as we have shown previously when driving such μTUG devices with a magnetic tweezer [27, 33]. This leads to a frequency doubling for a sinusoidal driving field, and so the motion of the pillar is at 1 Hz. This motion is nearly

sinusoidal with minimal distortion. Indeed, for the data shown in the inset of Figure 6.7c, the Fourier amplitude of the largest harmonic present (at f = 2 Hz) is only 5% of the 1 Hz fundamental (Figure 6.7c, main panel), and thus despite the modest hysteresis of the bar (Figure 6.6a) and the Ni sphere [33], we see that this system can apply clean periodic signals at physiologically relevant frequencies.

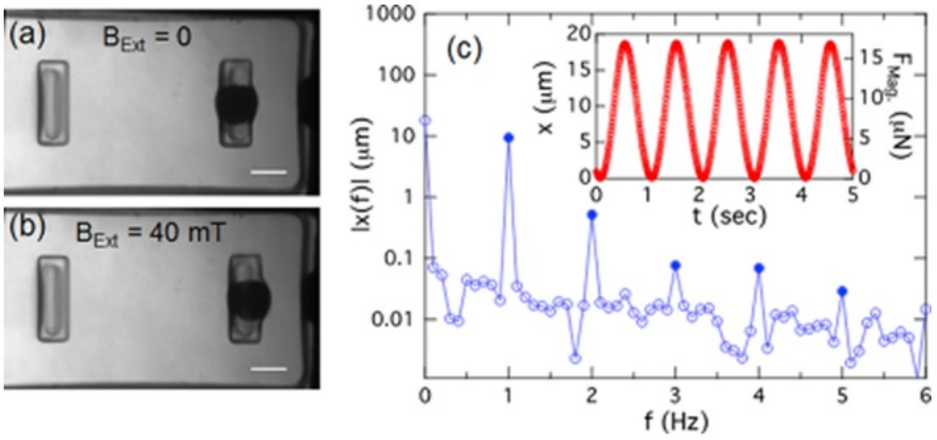

Figure 6.7 Magnetic AC drive characterization. (a) μTUG viewed through a Lid device. The Ni sphere appears as a dark circle on the right-hand pillar. The tip of the Ni bar is visible at right. (b) Application of $\mathbf{B_{Ext}}$ = 40 mT deflects the magnetic pillar 30 μm to the right. Scale bars in (a) and (b) are 100 μm. (c) Inset: Motion of a magnetic pillar in response to a sinusoidal driving field $\mathbf{B_{Ext}} = B_0 \sin(2\pi ft)$, with B_0 = 20 mT and f = 0.5 Hz. Frequency doubling produces a 1 Hz response, as discussed in the text. Right hand scale shows $\mathbf{F_{Mag}}$ as determined from the pillar spring constant k = 0.9 μN/μm. (c) Main panel: Fourier spectrum of motion shown in inset (calculated over 10 periods). Harmonics of 1 Hz fundamental are shown as solid points.

6.4 Experimental validation

In order to validate the use of the Lid device, an exchange student from Nanjing University, Xu Fan, used it to repeat the single stimulation and a variation of the AC stimulation experiments presented in Chapters 4 and 5 on 3T3 fibroblast microtissues. Briefly, after tissue formation (Figure 6.8a), a Lid device was mounted on the μTUG and

a step-wise ramped uniform magnetic field $\boldsymbol{B}_{\mathbf{Ext}}$ was applied to generate magnetic forces $\boldsymbol{F}_{\mathbf{Mag}}$ on the magnetic pillars. As shown in Figure 6.8b, these forces were sufficient to stretch the microtissues by 3%. Similar to the process presented in Chapter 4, stress and strain of the microtissues were determined. Representative examples of these stress-strain curves are plotted in Figure 6.8c. As can be seen, the stress-strain curves are quite linear, enabling the measurements of the elastic modulus for each microtissue from the slope of these curves.

For this set of data, the resulting average elastic modulus was 30 ± 6 kPa (N =7). To benchmark these results against the magnetic tweezer-based method, additional microtissues were cultured and their stiffnesses measured with the magnetic tweezer. The resulting value was 29 ± 9 kPa (N = 11) and showed good agreement with the Lid-based method ($p > 0.4$), demonstrating the Lid method as a reliable way to measure quasi-static mechanical properties of microtissues.

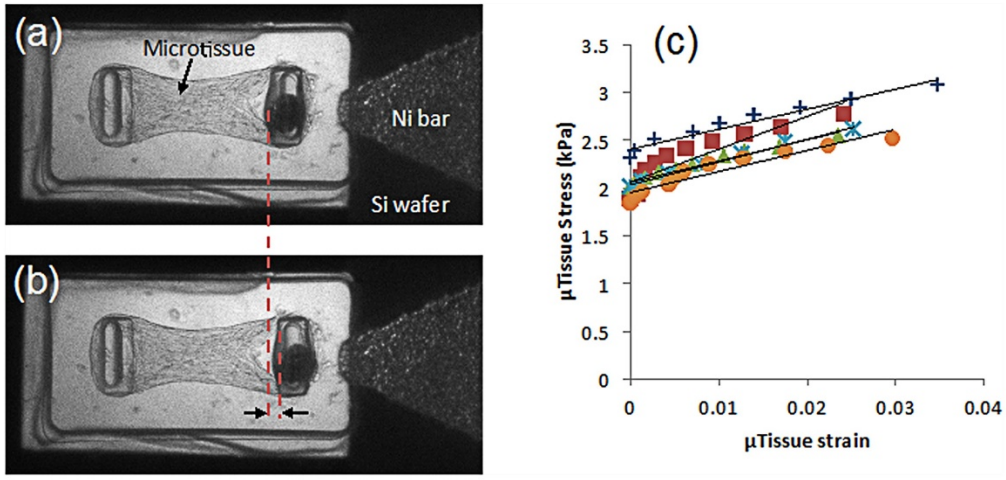

Figure 6.8 Quasistatic loading. (a) 3T3 fibrolast microtissues on µTUG with Lid device. (b) Application of a 20 mT external field displaces the magnetic pillar by 18 µm from its initial position (red dashed lines and black arrows) and causes a 3% strain. The tissue force as measured by the left pillar increase by 5 µN. (c) Examples of quasistatic stress-strain curves for a representative set of microtissues from a single µTUG array.

The dynamic loading capacity of the Lid device was evaluated by applying a sinusoidal magnetic external field of amplitude 20 mT at 1 Hz to the Lid devices on μTUGs. To verify that the microtissues underwent periodic actuation in response to this stimulation, we observed the microtissues' for brief intervals (~15 sec) while recording their motion at 100 frames/sec. Figure 6.9a shows the left pillar displacement (microtissue force) and overall length (difference in pillar positions) vs. time for a microtissue following initiation of actuation. Both the force and length are predominantly sinusoidal with second harmonic content < 6% of the 2 Hz fundamental, similar to that observed for AC actuation of magnetic pillars without microtissues (Figure 6.7). We observed temporary elongation of the microtissues, consistent with that observed over longer periods with magnetic tweezers.

To test the lids' potential for longer-term actuation, the elastic modulus of a set of microtissues was first measured by quasi-static loading with the Lid. Cyclic loading at 2 Hz (1 Hz external field) was then applied simultaneously to the tissues for 15 min, and the stiffness was re-measured. While there was some variability in the degree of stiffness change, all microtissues measured exhibited an increase in modulus (Figure 6.9b), with an average increase of 31%, again comparable to results obtained previously via the much more laborious process of serial actuation of individual microtissues with our magnetic tweezers [27].

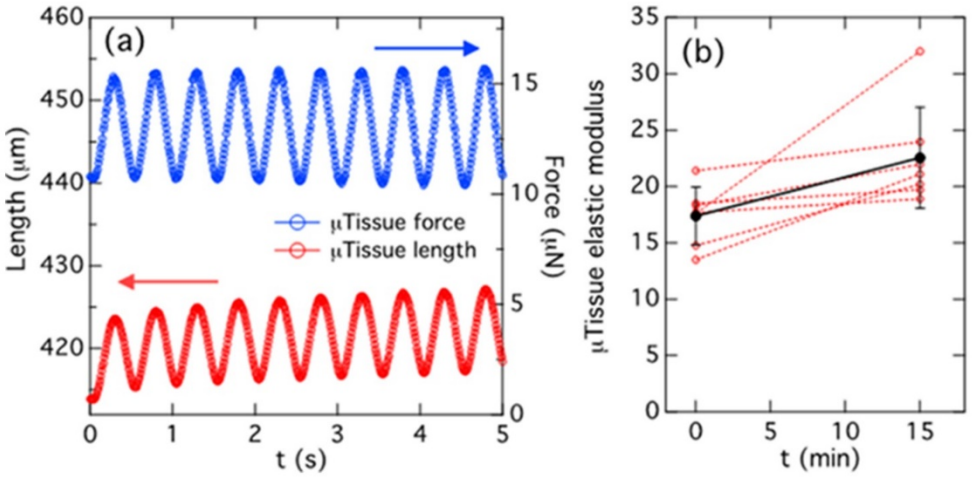

Figure 6.9 Dynamic conditioning of 3T3 microtissue. (a) Tracking of dynamic actuation of a microtissue with Lid device, showing 2 Hz modulation in force on microtissue (blue trace) and length (red trace) in response to a 1 Hz AC external magnetic field. The tissue length is reported as the inner edge-to-edge separation between the pillars. (b) Change in elastic modulus of microtissues cultured for one day and then stimulated at 2 Hz (1 Hz external field) for 15 min. (red traces). Results are taken from two μTUG arrays under identical conditions. All microtissues showed an increased stiffness. The average stiffness before and after stimulation (black symbols) showed a 31% increase.

6.5 Discussion

The Lid-μTUG device presented in this chapter can provide an excellent approach for a range of experimentation on small-scale multicellular 3D constructs, from fundamental studies of tissue biomechanics and cellular organization to drug screening and other diagnostics. In many other applications that can be envisioned, the ability to apply *in-situ* mechanical conditioning and to carry out mechanical testing are crucial ingredients, both to probe mechanobiology and to influence the development and/or maturation of the tissue constructs [20, 91-93]. The Lid-μTUG combination is able to

provide mechanical actuation to many microtissues in parallel, comparable to that generated previously with solely the magnetic tweezer and μTUG.

The primary engineering requirement for the Lid was for it to recapitulate the magnitude of force generation and level of control that an electromagnetic tweezer provides when paired with μTUG devices. The use of SU-8-based templated electrodeposition of Ni, which has been well-developed in the context of MEMS devices, provided a clean way to fabricate 100-μm to mm scale biocompatible magnetic components that are thick enough (t ~ 60-100 μm) to acquire sufficient magnetic moments [94, 95]. In modest ~30-50 mT external magnetic fields, these components were able to generate the 10s of μN-scale forces needed to actuate our microtissues.

The results from the Lid-μTUG experiments presented here mirror those from §4.2. This capability is very effectively reproduced using the Lid, and this system can also actuate multiple microtissues simultaneously at physiologically relevant frequencies. This opens the possibility of studies of maturation and other longer-term effects that are influenced by a dynamic mechanical environment. Because of the non-invasive nature of the magnetic actuation approach, long-term stimulation protocols can be readily implemented, e.g. by the simple expedient of mounting an electromagnet in an incubator that need only generate a spatially uniform (if time-varying) field.

The current visualization experiments employed conventional microscope-based imaging approaches that are best applied to single microtissues. This set-up is more than adequate for a wide range of experiments where it is not necessary to monitor mechanical properties during stimulation. However, if real-time monitoring of time evolution is

required, this system could be paired with a variety of parallel imaging approaches that can observe multiple microtissues simultaneously.

In this chapter, I have demonstrated the ability of patterned arrays of mm-scale magnetic bars to provide chronic stimulation at physiologically relevant frequencies to arrays of microtissues. These magnetic arrays are constructed using standard Si-based photolithography and micropatterning, and represent a simple and compact device for tissue mechanical conditioning and testing. The use of local magnetic features to transduce a uniform external magnetic field into the field gradients needed to produce forces on magnetic microtissue devices provides a flexible and non-contact mode of mechanical actuation that should be applicable to a variety of cell types. This approach can advance the field of tissue biomechanics, and potentially enable investigations of tissue maturation on the microscale.

Chapter 7 Future work and conclusion: applications for stem cell based studies

The mechanical interplay between cells and the surrounding ECM affects many biological processes [4]. In order to study these mechanics, engineered tissues were constructed on a microfabricated strain gauge which reported intrinsic tissue force and external force applied to the tissue via an applied magnetic field. The microtissues were stretched at two different time scales and their behavior was observed to ascertain their material properties. Finally, a device was developed which enabled the simultaneous application of external force to multiple microtissues.

Bovine pulmonary artery smooth muscle cell based microtissues may help elucidate the biomechanics of *in vivo* vasculature. By adjusting tissue engineering parameters such as cell seeding density and ECM density, the static stress generated by the microtissues was matched to that experienced by live arteries. The mechano-biochemical behavior of these microtissues was also validated and was found to behave

similarly to excised tissue in the presence of substances which either promote or inhibit force generation. The ability of the microtissues to respond to applied biochemical signals supports the use of the μTUG platform in high-throughput pharmacological testing. Future experiments which combine multiple cell types in a single microtissue, have different substrate geometries, or include other aspects of biological systems, such as fluid flow, may better mimic live tissues and lead to further insights.

To ascertain microtissue material properties such as stiffness and viscosity, an external stretching force was applied. This force was applied quasistatically and took the form of a triangle wave. Microtissue behavior was also observed for 10 minutes after the cessation of the external force. In these experiments, microtissue stiffness was highest when Rho-V14, a promoter of active cellular force, was upregulated and was lowest when the cells were lysed, suggesting that active cellular force generating mechanisms play a key role in overall microtissue mechanical properties. Furthermore, when the microtissue stress-strain behavior was modeled with a viscoplastic mathematical model, it was found that the actions of the cells prevent the microtissue from plastically yielding from tension, and that the bulk of the plasticity seen in these smooth muscle microtissues can be attributed to the ECM. It would be informative to apply this model to larger scale engineered tissues to ascertain the effect that a tissue's size has on its material properties.

Studies have shown that the mechanical behavior of collagen gels depends on their strain history [80], and to investigate whether this phenomenon held true in cell-populated collagen gels the canonical triangle wave pulse forcing established in Chapter 4 was applied multiple times to the microtissues: 3 times successively or twice with an intervening 10 minute observation period. When this force was applied 3 times

successively, tissue length and stiffness increased between the first and subsequent applications, indicating that the microtissues' mechanical behavior does indeed show a hysteretic response. However, when the successive application of force was interrupted by a 10 minute observation period, the active cellular processes within the microtissues allowed them to recover to their initial state. In both these instances, after the active cellular component had been removed through either Triton or trypsin treatment, the microtissue behaved like an inert, viscoplastic material. Modifying the quasistatic strain rate and length of recovery period may help elucidate the time scales involved in tissue biomechanics.

In vivo, arterial tissues experience continuous, cyclic forces on the order of 1 Hz due to pulsatile blood flow. In order to study the effects of this type of mechanical stimulation on the microtissues, a sinusoidal 1 Hz external force was applied. The microtissues' response fell on a range between that of a linear viscoelastic and non-linear, strain-stiffening viscoelastic material. Notably, strain-stiffening behavior diminished, and the stiffness of the microtissues increased as cyclic strains were maintained. This behavior suggests that microtissue remodeling by the cells may occur as a result of only a few minutes of applied cyclic strain, and these observations may be the early indications of dynamic tissue conditioning [96]. This effect can be studied by stimulating the microtissues over longer time periods (i.e. days rather than minutes).

In order to apply magnetic force to multiple microtissues simultaneously, a 'LID' device, which consisted of nickel bars built on a through-etched silicon substrate, was developed. This device allowed for the simultaneous stimulation of up to tens of microtissues. Biomechanical experiments conducted with these devices recapitulated the

results seen when microtissues were stimulated individually. The LID device can therefore be seen as a way to apply long-term cyclic forces to microtissues and may be able to serve as the basis for tissue conditioning experiments.

In addition to understanding the reciprocal mechanical relationship between cells and ECM from a scientific standpoint, the ultimate practical use of studying cell-populated collagen gels will be an engineering one. The critical goal of tissue engineering efforts is the implantation of *in vitro* developed tissues into a patient, and as scientists learn to better manipulate the fate of stem cells, many of these implantable tissues will have a stem-cell basis. As these cells will likely be difficult to create and require expensive reagents to maintain, the μTUG device may provide a logical choice for determining the tissue replacement viability of various stem cell lines.

To demonstrate this concept, I created microtissues using human embryonic stem cell (hESC) derived cardiomyocytes generously provided by Professor Ron Li at Hong Kong University. These model cardiac tissues notably were able to generate spontaneous beating forces at a frequency of 0.7 ± 0.2 Hz. The tissues were able to capture pacing up to a nominal 2.5 Hz, an order of magnitude higher than that reported previously [30].

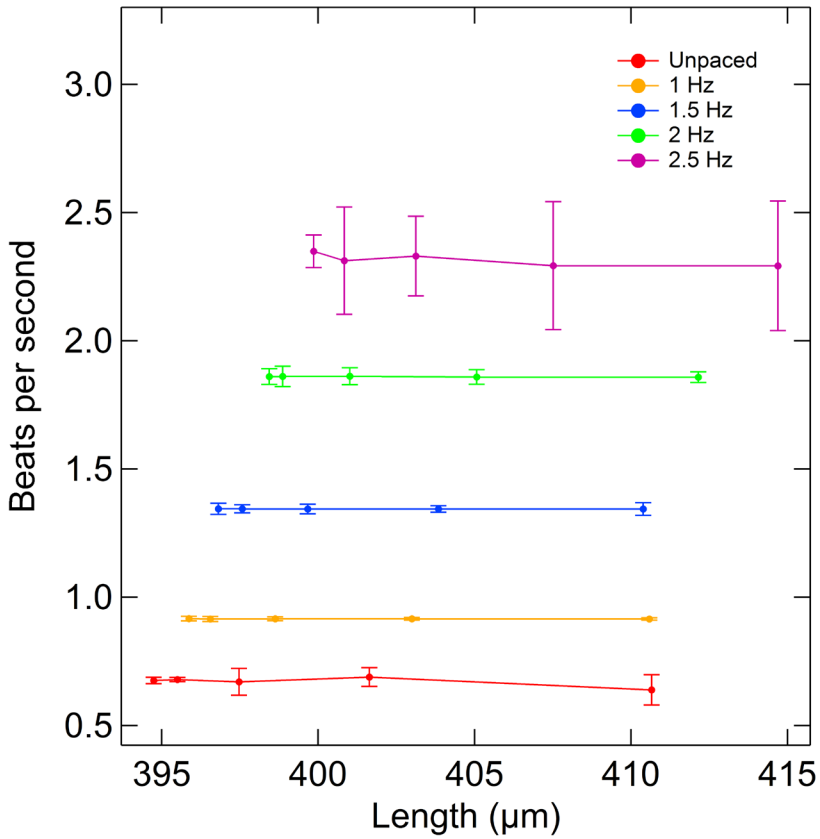

Figure 7.1 Beat frequency remains relatively constant as tissue length increases. Cardiomyocytes pacing at frequencies up to ~2.5 Hz as tissue is stretched via an applied magnetic field. Legend denotes frequency setting on the stimulator.

Microtissue length was also increased during pacing through the application of an external magnetic force (as described previously) to observe what effect length changes would have on force generation, and they were able to induce a Frank-Starling type behavior seen in *in vivo* cardiac tissue: as the microtissues' lengths increased, they were able to generate more force.

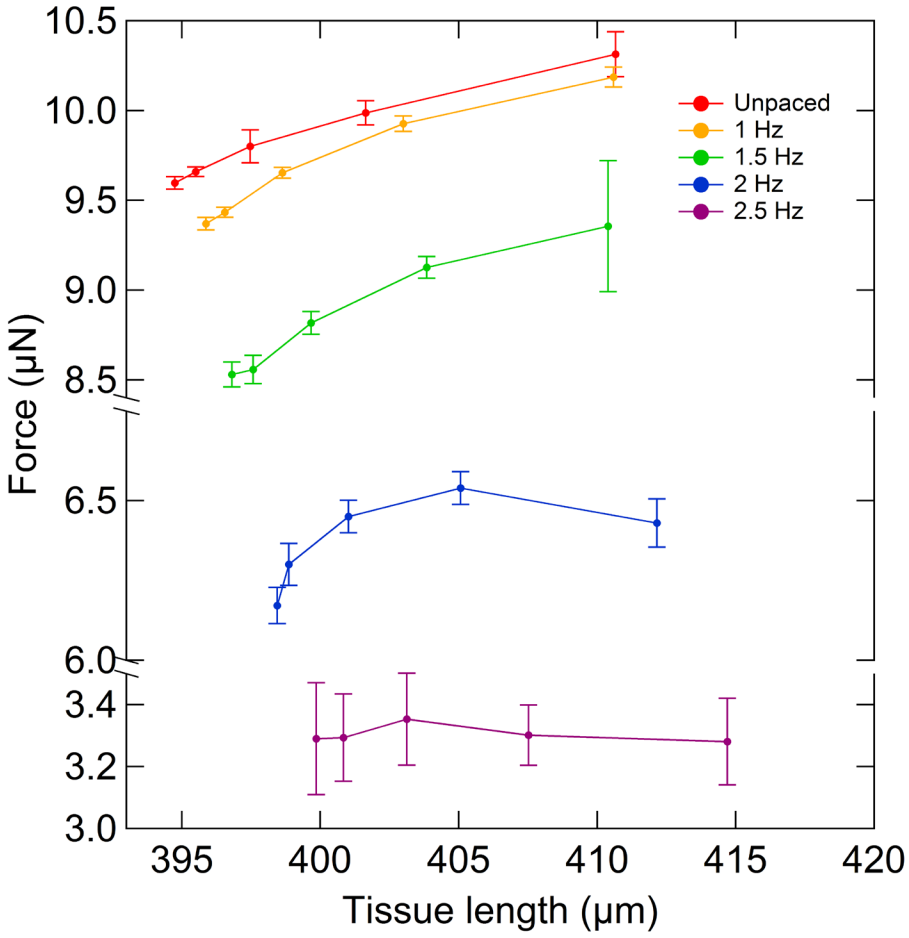

Figure 7.2 Microtissue force generation as function of length. Single microtissue was unpaced or paced at 4 different frequencies while undergoing stretch. As microtissues were stretched, they were able to generate more force, exhibiting a classic Frank-Starling type behavior seen in *in vivo* cardiac tissue. Note: dependent axis scaling modified in order to better display effect.

The microtissues presented in this thesis were used to study the biophysical properties of a combined cell-matrix construct. Encouragingly, they were able to recapitulate the important characteristics of relatively passive vascular smooth muscle and relatively active cardiac muscle, and hopefully, the experimental results derived from these microtissues will provide a portion of the foundation needed to support the creation of implantable tissue replacements in the future.

Chapter 8 Appendix

8.1 Microtissue engineering

The steps below occur immediately following the mixing of the ECM solution presented in § 2.3.2.

1. **Adding ECM solution to µTUG substrate:**
    a. Retrieve µTUG substrate from freezer.
    b. Add ~800 µL ECM solution to substrate.
    c. Degas (on ice) to pull solution into individual µTUG wells.

2. **Seeding cells:**
    a. Trypsinize cells, count, and spin down appropriate number (~280,000 per µTUG for BPA-SMCs)
    b. Aspirate media from pellet and re-suspend cells in remaining 1.2 mL of ECM solution.
    c. Add this solution to µTUG substrate, making sure to mix well.
    d. Spin cells down into individual µTUG wells: Centrifuge at 1200 RPM for 1.5 minutes. Rotate substrate 90 degrees and centrifuge again at 1200 RPM for 1.5 minutes.

3. **Removing excess collagen, polymerizing ECM solution, and final steps:**
    a. Tilt µTUG substrate at 30° angle and begin aspirating ECM solution starting at one of the upper corners of the substrate. Alternate corners as the solution 'dewets' from the surface of the substrate. Entire dewetting process should take at least 3 minutes, but not more than 5 minutes.
    b. Add 1 mL of sterile H20 to lid of 35 mm dish which house the µTUG substrate and invert µTUG onto the lid.
    c. Place dish into 37 °C incubator for 9:15 minutes.
    d. Aspirate H20 from lid.
    e. Add 1-2 mL growth media drop by drop (in order to minimize media flow and shear forces on underlying substrate) and replace µTUG in incubator.

8.2 Trypsin treatment

In order to remove cell-ECM interaction, microtissues were treated with 0.25% trypsin EDTA. The following procedure details this treatment.

1. Aspirate media.
2. Wash microtissue with PBS -/- and aspirate.
3. Incubate microtissue at room temperature with 0.25% Trypsin EDTA solution for 10 mins.
4. Aspirate Trypsin solution.
5. Add PBS -/- and conduct mechanical experiments immediately.

8.3 Fitting curves using a random search algorithm

Model parameters were obtained by fitting stress vs. time curves to actual experimental results using a random search algorithm, where the strain vs time curves are known. For each group of parameters, the simulation curves were generated and compared with the experimental data. The optimized parameters were obtained by minimizing the normalized sum of squared residuals χ until $\chi < 5\%$ or the search steps is larger than the maximum search step. The normalized sum of squared residuals can be defined as the difference between the simulation stress, $\sigma_s(t_i)$, and experimental stress, $\sigma_e(t_i)$,

$$\chi = \frac{1}{N\left(\sigma_e^{max}(t_i) - \sigma_e^{min}(t_i)\right)^2}\sum_{i=1}^{N}\left(\sigma_s(t_i) - \sigma_e(t_i)\right)^2,$$

where i denotes the *ith* data point, *N* is the data number. $\sigma_e^{max}(t_i)$ and $\sigma_e^{min}(t_i)$ is the maximum and minimum experimental stress, respectively [97]. [From Hailong Wang]

Bibliography

1. Chambliss, A.B., et al., *The LINC-anchored actin cap connects the extracellular milieu to the nucleus for ultrafast mechanotransduction.* Scientific reports, 2013. **3**.
2. McBeath, R., et al., *Cell shape, cytoskeletal tension, and RhoA regulate stem cell lineage commitment.* Developmental cell, 2004. **6**(4): p. 483-495.
3. Lee, J.-Y., et al., *Wnt/Frizzled signaling controls C. elegans gastrulation by activating actomyosin contractility.* Current biology, 2006. **16**(20): p. 1986-1997.
4. Chen, C.S., *Mechanotransduction - a field pulling together?* J Cell Sci, 2008. **121**(Pt 20): p. 3285-92.
5. Weiss, L., G. Elkin, and E. Barbera-Guillem, *The differential resistance of B16 wild-type and F10 cells to mechanical trauma in vitro.* Invasion & metastasis, 1992. **13**(2): p. 92-101.
6. Cunningham, K.S. and A.I. Gotlieb, *The role of shear stress in the pathogenesis of atherosclerosis.* Laboratory investigation, 2005. **85**(1): p. 9-23.
7. Jaalouk, D.E. and J. Lammerding, *Mechanotransduction gone awry.* Nature reviews Molecular cell biology, 2009. **10**(1): p. 63-73.
8. Sniadecki, N.J., et al., *Magnetic microposts as an approach to apply forces to living cells.* Proc Natl Acad Sci U S A, 2007. **104**(37): p. 14553-8.
9. Nagayama, K., A. Adachi, and T. Matsumoto, *Heterogeneous response of traction force at focal adhesions of vascular smooth muscle cells subjected to macroscopic stretch on a micropillar substrate.* J Biomech, 2011. **44**(15): p. 2699-705.
10. Krishnan, R., et al., *Reinforcement versus fluidization in cytoskeletal mechanoresponsiveness.* PLoS One, 2009. **4**(5): p. e5486.
11. Charras, G.T. and M.A. Horton, *Single cell mechanotransduction and its modulation analyzed by atomic force microscope indentation.* Biophysical Journal, 2002. **82**(6): p. 2970-2981.
12. Alberts, B., et al., *Essential cell biology*. 2013: Garland Science.

13. Adelstein, R., *Regulation of contractile proteins by phosphorylation.* Journal of Clinical Investigation, 1983. **72**(6): p. 1863.
14. Harris, A.K., P. Wild, and D. Stopak, *Silicone rubber substrata: a new wrinkle in the study of cell locomotion.* Science, 1980. **208**(4440): p. 177-179.
15. Koch, T.M., et al., *3D traction forces in cancer cell invasion.* PLoS One, 2012. **7**(3): p. e33476.
16. Trepat, X., et al., *Physical forces during collective cell migration.* Nature physics, 2009. **5**(6): p. 426-430.
17. Liu, Z., et al., *Mechanical tugging force regulates the size of cell–cell junctions.* Proceedings of the National Academy of Sciences, 2010. **107**(22): p. 9944-9949.
18. Kanchanawong, P., et al., *Nanoscale architecture of integrin-based cell adhesions.* Nature, 2010. **468**(7323): p. 580-584.
19. Dallon, J.C. and H.P. Ehrlich, *A review of fibroblast-populated collagen lattices.* Wound Repair Regen, 2008. **16**(4): p. 472-9.
20. Seliktar, D., et al., *Dynamic mechanical conditioning of collagen-gel blood vessel constructs induces remodeling in vitro.* Annals of biomedical engineering, 2000. **28**(4): p. 351-362.
21. Cummings, C.L., et al., *Properties of engineered vascular constructs made from collagen, fibrin, and collagen–fibrin mixtures.* Biomaterials, 2004. **25**(17): p. 3699-3706.
22. Kanda, K., T. Matsuda, and T. Oka, *Mechanical stress induced cellular orientation and phenotypic modulation of 3-D cultured smooth muscle cells.* ASAIO journal, 1993. **39**(3): p. M691.
23. Wakatsuki, T., et al., *Cell mechanics studied by a reconstituted model tissue.* Biophysical Journal, 2000. **79**(5): p. 2353-2368.
24. Wille, J.J., E.L. Elson, and R.J. Okamoto, *Cellular and matrix mechanics of bioartificial tissues during continuous cyclic stretch.* Annals of biomedical engineering, 2006. **34**(11): p. 1678-1690.
25. Billiar, K.L., *The mechanical environment of cells in collagen gel models*, in *Cellular and biomolecular mechanics and mechanobiology*. 2011, Springer. p. 201-245.
26. Legant, W.R., et al., *Microfabricated tissue gauges to measure and manipulate forces from 3D microtissues.* Proc Natl Acad Sci U S A, 2009. **106**(25): p. 10097-102.
27. Zhao, R., et al., *Decoupling cell and matrix mechanics in engineered microtissues using magnetically actuated microcantilevers.* Adv Mater, 2013. **25**(12): p. 1699-705.
28. Foulds, I. and M. Parameswaran, *A planar self-sacrificial multilayer SU-8-based MEMS process utilizing a UV-blocking layer for the creation of freely moving parts.* Journal of Micromechanics and Microengineering, 2006. **16**(10): p. 2109.
29. Bodas, D. and C. Khan-Malek, *Formation of more stable hydrophilic surfaces of PDMS by plasma and chemical treatments.* Microelectronic engineering, 2006. **83**(4): p. 1277-1279.
30. Boudou, T., et al., *A microfabricated platform to measure and manipulate the mechanics of engineered cardiac microtissues.* Tissue Engineering Part A, 2011. **18**(9-10): p. 910-919.

31. Johnston, I., et al., *Mechanical characterization of bulk Sylgard 184 for microfluidics and microengineering.* Journal of Micromechanics and Microengineering, 2014. **24**(3): p. 035017.
32. Feynman, R., *The Feynman Lectures on Physics.* 1964. **2**.
33. Zhao, R., et al., *Magnetic approaches to study collective three-dimensional cell mechanics in long-term cultures.* Journal of applied physics, 2014. **115**(17): p. 172616.
34. West, A.R., et al., *Development and characterization of a 3D multicell microtissue culture model of airway smooth muscle.* American Journal of Physiology-Lung Cellular and Molecular Physiology, 2013. **304**(1): p. L4-L16.
35. Ye, Q., et al., *Fibrin gel as a three dimensional matrix in cardiovascular tissue engineering.* European Journal of Cardio-Thoracic Surgery, 2000. **17**(5): p. 587-591.
36. Fukata, Y., K. Kaibuchi, and M. Amano, *Rho–Rho-kinase pathway in smooth muscle contraction and cytoskeletal reorganization of non-muscle cells.* Trends in pharmacological sciences, 2001. **22**(1): p. 32-39.
37. Wang, Y., et al., *ROCK isoform regulation of myosin phosphatase and contractility in vascular smooth muscle cells.* Circulation research, 2009. **104**(4): p. 531-540.
38. Maekawa, M., et al., *Signaling from Rho to the actin cytoskeleton through protein kinases ROCK and LIM-kinase.* Science, 1999. **285**(5429): p. 895-898.
39. *Rho associated protein kinase*. [Webpage] 6/1/2015]; Available from: http://en.wikipedia.org/wiki/Rho-associated_protein_kinase.
40. Copeland, C., *Cellular forces and mechanical coupling using microengineered devices.* Doctoral dissertation, Johns Hopkins University, 2014.
41. Ishizaki, T., et al., *Pharmacological properties of Y-27632, a specific inhibitor of rho-associated kinases.* Molecular pharmacology, 2000. **57**(5): p. 976-983.
42. Antman, E.M., et al., *Use of nonsteroidal antiinflammatory drugs an update for clinicians: a scientific statement from the American Heart Association.* Circulation, 2007. **115**(12): p. 1634-1642.
43. Famaey, J., *In vitro and in vivo pharmacological evidence of selective cyclooxygenase-2 inhibition by nimesulide: an overview.* Inflammation Research, 1997. **46**(11): p. 437-446.
44. Funk, C.D. and G.A. FitzGerald, *COX-2 inhibitors and cardiovascular risk.* Journal of cardiovascular pharmacology, 2007. **50**(5): p. 470-479.
45. Bhala, N., et al., *Vascular and upper gastrointestinal effects of non-steroidal anti-inflammatory drugs: meta-analyses of individual participant data from randomised trials.* Lancet, 2013. **382**(9894): p. 769-779.
46. Kearney, P.M., et al., *Do selective cyclo-oxygenase-2 inhibitors and traditional non-steroidal anti-inflammatory drugs increase the risk of atherothrombosis? Meta-analysis of randomised trials.* Bmj, 2006. **332**(7553): p. 1302-1308.
47. Aw, T.-J., et al., *Meta-analysis of cyclooxygenase-2 inhibitors and their effects on blood pressure.* Archives of Internal Medicine, 2005. **165**(5): p. 490-496.
48. Gilbert, T.W., T.L. Sellaro, and S.F. Badylak, *Decellularization of tissues and organs.* Biomaterials, 2006. **27**(19): p. 3675-3683.

49. DOYLE, J.T., et al., *Observations on the circulation of domestic cattle.* Circulation Research, 1960. **8**(1): p. 4-15.
50. Stiebellehner, L., et al., *Bovine distal pulmonary arterial media is composed of a uniform population of well-differentiated smooth muscle cells with low proliferative capabilities.* Am J Physiol Lung Cell Mol Physiol, 2003. **285**(4): p. L819-28.
51. Wagenseil, J.E. and R.P. Mecham, *Vascular extracellular matrix and arterial mechanics.* Physiological reviews, 2009. **89**(3): p. 957-989.
52. Roeder, B.A., et al., *Tensile Mechanical Properties of Three-Dimensional Type I Collagen Extracellular Matrices With Varied Microstructure.* Journal of Biomechanical Engineering, 2002. **124**(2): p. 214.
53. Narumiya, S., T. Ishizaki, and M. Ufhata, *Use and properties of ROCK-specific inhibitor Y-27632.* Methods in enzymology, 2000. **325**: p. 273-284.
54. Gan, C.T.-J., et al., *Noninvasively assessed pulmonary artery stiffness predicts mortality in pulmonary arterial hypertension.* CHEST Journal, 2007. **132**(6): p. 1906-1912.
55. O'Rourke, M.F. and M.E. Safar, *Relationship between aortic stiffening and microvascular disease in brain and kidney cause and logic of therapy.* Hypertension, 2005. **46**(1): p. 200-204.
56. Bianco, P. and P.G. Robey, *Stem cells in tissue engineering.* Nature, 2001. **414**(6859): p. 118-121.
57. Larsen, M., et al., *The matrix reorganized: extracellular matrix remodeling and integrin signaling.* Current opinion in cell biology, 2006. **18**(5): p. 463-471.
58. Sumpio, B.E., et al., *Mechanical stress stimulates aortic endothelial cells to proliferate.* Journal of vascular surgery, 1987. **6**(3): p. 252-256.
59. LIU, Y. and D.R. SENGER, *Matrix-specific activation of Src and Rho initiates capillary morphogenesis of endothelial cells.* The FASEB journal, 2004. **18**(3): p. 457-468.
60. Bell, E., B. Ivarsson, and C. Merrill, *Production of a tissue-like structure by contraction of collagen lattices by human fibroblasts of different proliferative potential in vitro.* Proceedings of the National Academy of Sciences, 1979. **76**(3): p. 1274-1278.
61. Marquez, J.P., et al., *Thin bio-artificial tissues in plane stress: the relationship between cell and tissue strain, and an improved constitutive model.* Biophysical journal, 2005. **88**(2): p. 765-777.
62. Stamenovic, D., et al., *Viscoplasticity of respiratory tissues.* Journal of Applied Physiology, 1990. **69**(3): p. 973-988.
63. Zahalak, G.I., et al., *A cell-based constitutive relation for bio-artificial tissues.* Biophysical journal, 2000. **79**(5): p. 2369-2381.
64. Tan, J.L., et al., *Cells lying on a bed of microneedles: an approach to isolate mechanical force.* Proc Natl Acad Sci U S A, 2003. **100**(4): p. 1484-9.
65. Zhao, R., C.S. Chen, and D.H. Reich, *Force-driven evolution of mesoscale structure in engineered 3D microtissues and the modulation of tissue stiffening.* Biomaterials, 2014. **35**(19): p. 5056-5064.

66. Wang, H., et al., *Necking and failure of constrained 3D microtissues induced by cellular tension.* Proceedings of the National Academy of Sciences, 2013. **110**(52): p. 20923-20928.
67. Fu, J., et al., *Mechanical regulation of cell function with geometrically modulated elastomeric substrates.* Nature methods, 2010. **7**(9): p. 733-736.
68. Lin, Y.-C., et al., *Probing cellular traction forces with magnetic nanowires and microfabricated force sensor arrays.* Nanotechnology, 2012. **23**(7): p. 075101.
69. Mann, J.M., et al., *A silicone-based stretchable micropost array membrane for monitoring live-cell subcellular cytoskeletal response.* Lab on a Chip, 2012. **12**(4): p. 731-740.
70. Sheu, M.-T., et al., *Characterization of collagen gel solutions and collagen matrices for cell culture.* Biomaterials, 2001. **22**(13): p. 1713-1719.
71. Institute, N.I.o.H.N.H.G.R., *"Fibroblast".* Talking Glossary of Genetic Terms.
72. Evans, M.C. and V.H. Barocas, *The modulus of fibroblast-populated collagen gels is not determined by final collagen and cell concentration: Experiments and an inclusion-based model.* J Biomech Eng, 2009. **131**(10): p. 101014.
73. Notbohm, J., et al., *Microbuckling of fibrin provides a mechanism for cell mechanosensing.* Journal of The Royal Society Interface, 2015. **12**(108): p. 20150320.
74. Meyrick, B. and L. Reid, *Hypoxia-induced structural changes in the media and adventitia of the rat hilar pulmonary artery and their regression.* The American journal of pathology, 1980. **100**(1): p. 151.
75. Motta, P., *Ultrastructure of smooth muscle*. Vol. 8. 2012: Springer Science & Business Media.
76. Marquez, J.P., et al., *The relationship between cell and tissue strain in three-dimensional bio-artificial tissues.* Biophysical journal, 2005. **88**(2): p. 778-789.
77. Isenberg, B.C., C. Williams, and R.T. Tranquillo, *Small-diameter artificial arteries engineered in vitro.* Circ Res, 2006. **98**(1): p. 25-35.
78. Xu, F., et al., *A microfabricated magnetic actuation device for mechanical conditioning of arrays of 3D microtissues.* Lab on a Chip, 2015. **15**(11): p. 2496-2503.
79. Brenner, S.L. and E. Korn, *The effects of cytochalasins on actin polymerization and actin ATPase provide insights into the mechanism of polymerization.* Journal of Biological Chemistry, 1980. **255**(3): p. 841-844.
80. Münster, S., et al., *Strain history dependence of the nonlinear stress response of fibrin and collagen networks.* Proceedings of the National Academy of Sciences, 2013. **110**(30): p. 12197-12202.
81. Xu, B., M.-J. Chow, and Y. Zhang, *Experimental and modeling study of collagen scaffolds with the effects of crosslinking and fiber alignment.* International journal of biomaterials, 2011. **2011**.
82. Pryse, K.M., et al., *Incremental mechanics of collagen gels: new experiments and a new viscoelastic model.* Annals of biomedical engineering, 2003. **31**(10): p. 1287-1296.
83. Cheng, C.-M. and Y.-T. Cheng, *On the initial unloading slope in indentation of elastic-plastic solids by an indenter with an axisymmetric smooth profile.* Applied physics letters, 1997. **71**(18): p. 2623-2625.

84. Bogren, H.G., et al., *Pulmonary artery distensibility and blood flow patterns: a magnetic resonance study of normal subjects and of patients with pulmonary arterial hypertension.* American heart journal, 1989. **118**(5): p. 990-999.
85. Jardim, C., et al., *Pulmonary artery distensibility in pulmonary arterial hypertension: an MRI pilot study.* European Respiratory Journal, 2007. **29**(3): p. 476-481.
86. Karau, K.L., et al., *Microfocal X-ray CT imaging and pulmonary arterial distensibility in excised rat lungs.* American Journal of Physiology-Heart and Circulatory Physiology, 2001. **281**(3): p. H1447-H1457.
87. Vader, D., et al., *Strain-induced alignment in collagen gels.* PloS one, 2009. **4**(6): p. e5902.
88. Xu, J., Y. Tseng, and D. Wirtz, *Strain Hardening of actin filament networks regulation by the dynamic cross-linking protein α-actinin.* Journal of Biological Chemistry, 2000. **275**(46): p. 35886-35892.
89. Holzapfel, G.A., et al., *Determination of layer-specific mechanical properties of human coronary arteries with nonatherosclerotic intimal thickening and related constitutive modeling.* American Journal of Physiology-Heart and Circulatory Physiology, 2005. **289**(5): p. H2048-H2058.
90. Crangle, J. and G. Goodman. *The magnetization of pure iron and nickel*. in *Proceedings of the Royal Society of London A: Mathematical, Physical and Engineering Sciences*. 1971. The Royal Society.
91. Barron, V., et al., *Bioreactors for cardiovascular cell and tissue growth: a review.* Annals of biomedical engineering, 2003. **31**(9): p. 1017-1030.
92. Apte, S.S., et al., *Current developments in the tissue engineering of autologous heart valves: moving towards clinical use.* Future cardiology, 2011. **7**(1): p. 77-97.
93. Hoerstrup, S.P., et al., *New pulsatile bioreactor for in vitro formation of tissue engineered heart valves.* Tissue engineering, 2000. **6**(1): p. 75-79.
94. Ho, C.-H., et al., *Ultrathick SU-8 mold formation and removal, and its application to the fabrication of LIGA-like micromotors with embedded roots.* Sensors and Actuators A: Physical, 2002. **102**(1): p. 130-138.
95. Lorenz, H., et al., *SU-8: a low-cost negative resist for MEMS.* Journal of Micromechanics and Microengineering, 1997. **7**(3): p. 121.
96. Kim, B.-S., et al., *Cyclic mechanical strain regulates the development of engineered smooth muscle tissue.* Nature biotechnology, 1999. **17**(10): p. 979-983.
97. Bergstra, J. and Y. Bengio, *Random search for hyper-parameter optimization.* The Journal of Machine Learning Research, 2012. **13**(1): p. 281-305.

Vita

Alan S. Liu was born on May 5, 1987 in Shijiazhuang, China to Zhi-Jun and Jian-Ying Liu. He attended the University of North Carolina at Chapel Hill, where he graduated with a B.S. in Physics in 2009. He received his Ph.D. in Physics from Johns Hopkins University in September, 2015.